

Washington University in St. Louis

## Washington University Open Scholarship

---

All Theses and Dissertations (ETDs)

---

January 2010

### Biologically Inspired Sensing and MIMO Radar Array Processing

Murat Akcakaya

*Washington University in St. Louis*

Follow this and additional works at: <https://openscholarship.wustl.edu/etd>

---

#### Recommended Citation

Akcakaya, Murat, "Biologically Inspired Sensing and MIMO Radar Array Processing" (2010). *All Theses and Dissertations (ETDs)*. 12.

<https://openscholarship.wustl.edu/etd/12>

This Dissertation is brought to you for free and open access by Washington University Open Scholarship. It has been accepted for inclusion in All Theses and Dissertations (ETDs) by an authorized administrator of Washington University Open Scholarship. For more information, please contact [digital@wumail.wustl.edu](mailto:digital@wumail.wustl.edu).

WASHINGTON UNIVERSITY IN ST. LOUIS  
School of Engineering and Applied Science  
Department of Electrical & Systems Engineering

Dissertation Examination Committee:

Dr. Arye Nehorai, Chair  
Dr. R. Martin Arthur  
Dr. Jr-Shin Li  
Dr. Nan Lin  
Dr. Hiro Mukai  
Dr. Carlos H. Muravchik  
Dr. Tzyh Jong Tarn

BIOLOGICALLY INSPIRED SENSING AND MIMO RADAR ARRAY  
PROCESSING

by

Murat Akçakaya

A dissertation presented to the Graduate School of Arts and Sciences  
of Washington University in partial fulfillment of the  
requirements for the degree of

DOCTOR OF PHILOSOPHY

December 2010  
Saint Louis, Missouri

copyright by  
Murat Akçakaya  
2010

## ABSTRACT OF THE DISSERTATION

Biologically Inspired Sensing and MIMO Radar Array Processing

by

Murat Akçakaya

Doctor of Philosophy in Electrical Engineering

Washington University in St. Louis, December 2010

Research Advisor: Dr. Arye Nehorai

The contributions of this dissertation are in the fields of biologically inspired sensing and multi-input multi-output (MIMO) radar array processing. In our research on biologically inspired sensing, we focus on the mechanically coupled ears of the female *Ormia ochracea*. Despite the small distance between its ears, the *Ormia* has a remarkable localization ability. We statistically analyze the localization accuracy of the *Ormia*'s coupled ears, and illustrate the improvement in the localization performance due to the mechanical coupling.

Inspired by the *Ormia*'s ears, we analytically design coupled small-sized antenna arrays with high localization accuracy and radiation performance. Such arrays are essential for sensing systems in military and civil applications, which are confined to small spaces. We quantitatively demonstrate the improvement in the antenna array's radiation and localization performance due to the biologically inspired coupling.

On MIMO radar, we first propose a statistical target detection method in the presence of realistic clutter. We use a compound-Gaussian distribution to model the heavy

tailed characteristics of sea and foliage clutter. We show that MIMO radars are useful to discriminate a target from clutter using the spatial diversity of the illuminated area, and hence MIMO radar outperforms conventional phased-array radar in terms of target-detection capability.

Next, we develop a robust target detector for MIMO radar in the presence of a phase synchronization mismatch between transmitter and receiver pairs. Such mismatch often occurs due to imperfect knowledge of the locations as well as local oscillator characteristics of the antennas, but this fact has been ignored by most researchers. Considering such errors, we demonstrate the degradation in detection performance.

Finally, we analyze the sensitivity of MIMO radar target detection to changes in the cross-correlation levels (CCLs) of the received signals. Prior research about MIMO radar assumes orthogonality among the received signals for all delay and Doppler pairs. However, due to the use of antennas which are widely separated in space, it is impossible to maintain this orthogonality in practice. We develop a target-detection method considering the non-orthogonality of the received data. In contrast to the common assumption, we observe that the effect of non-orthogonality is significant on detection performance.

# Acknowledgments

First of all, I would like to express my gratitude to my supervisor Dr. Arye Nehorai for his continued encouragement and support. Under his valuable guidance, I had the opportunity to be part of a productive research team and work on many exciting research topics. He introduced me to the subject of Ormia and to MIMO radar signal processing, which were critical to the success of my work.

I wish to thank the members of my dissertation committee, Dr. R. Martin Arthur, Dr. Jr-Shin Li, Dr. Nan Lin, Dr. Hiro Mukai, Dr. Carlos H. Muravchik, and Dr. Tzyh Jong Tarn for their time and constructive comments to improve the quality of this dissertation. I cannot forget to thank Mr. James C. Ballard, Dr. Lynnea Brumbaugh, and Ms. Sandra Matteucci for their editorial suggestions on this dissertation.

Dr. Dan Schonfeld, Dr. Daniela Tuninetti, and Dr. Dibyen Majumdar from University of Illinois at Chicago, and Dr. Barry Spielman, Dr. Daniel Fuhrman, and Dr. Joseph O'Sullivan from Washington University in Saint Louis provided me with the chance to learn from the best, I am grateful to them. I would also like to thank all the staff members of the Preston M. Green Electrical & Systems Engineering Department at Washington University for their time and help.

I would like to thank all my labmates for providing a friendly work environment. I would especially like to thank Dr. Satyabrata Sen for his friendship and support in my research over the last five years. I am also thankful to all my friends from Chicago and Saint Louis for making my time in United States memorable.

Last but not least, my sincere gratitude goes to my family, including my parents, my sister, and my wife Rebecca Reese Akçakaya for their endless love and emotional support. This dissertation is dedicated to them.

Murat Akçakaya

*Washington University in Saint Louis  
December 2010*

To my family.

# Contents

Abstract . . . . .	ii
Acknowledgments . . . . .	iv
List of Tables . . . . .	ix
List of Figures . . . . .	x
List of Abbreviations . . . . .	xiii
List of Notations . . . . .	xiv
<b>1 Introduction . . . . .</b>	<b>1</b>
1.1 Biologically Inspired Sensing . . . . .	1
1.1.1 Performance of the Ormia Ochracea’s Coupled Ears . . . . .	3
1.1.2 Biologically Inspired Antenna Array . . . . .	4
1.2 Multi-Input Multi-Output Radar . . . . .	5
1.2.1 Adaptive MIMO Radar Design and Detection in Compound-Gaussian Clutter . . . . .	7
1.2.2 MIMO Radar Detection and Adaptive Design Under a Phase Synchronization Mismatch . . . . .	8
1.2.3 MIMO Radar Sensitivity Analysis for Target Detection . . . . .	9
1.2.4 Outline of the Dissertation . . . . .	9
<b>2 Performance of the Ormia Ochracea’s Coupled Ears . . . . .</b>	<b>11</b>
2.1 Introduction . . . . .	12
2.2 Modeling . . . . .	13
2.3 Performance Analysis . . . . .	18
2.3.1 Statistical Model . . . . .	18
2.3.2 Cramér-Rao Bound . . . . .	20
2.4 Numerical Results . . . . .	21
2.5 Summary . . . . .	24
<b>3 Biologically Inspired Coupled Antenna System . . . . .</b>	<b>25</b>
3.1 Introduction . . . . .	26
3.2 Biologically Inspired Coupled Antenna Array for Direction of Arrival Estimation . . . . .	27



3.2.1	Antenna Array Model . . . . .	28
3.2.2	Maximum Likelihood Estimation and Performance Analysis . . . . .	39
3.2.3	Optimization of the Biologically Inspired Coupling . . . . .	43
3.2.4	Circular Antenna Array With Biologically Inspired Coupling . . . . .	45
3.2.5	Numerical Results . . . . .	47
3.3	Biologically Inspired Coupled Antenna Beampattern Design . . . . .	56
3.3.1	Array Factor . . . . .	57
3.3.2	Radiation Intensity, Directivity, Half-power Beamwidth and Side Lobe Level . . . . .	61
3.3.3	Optimization of the Biologically Inspired Coupling . . . . .	63
3.3.4	Numerical Examples for Beampattern Design . . . . .	64
3.4	Summary . . . . .	67
<b>4</b>	<b>Adaptive MIMO Radar Design and Detection in Compound-Gaussian Clutter . . . . .</b>	<b>68</b>
4.1	Introduction . . . . .	69
4.2	Radar Model . . . . .	70
4.2.1	Measurement Model . . . . .	70
4.2.2	Statistical Model . . . . .	73
4.3	Detection and Estimation Algorithms . . . . .	74
4.4	Adaptive Design . . . . .	79
4.5	Numerical Examples . . . . .	83
4.6	Summary . . . . .	86
<b>5</b>	<b>MIMO Radar Detection and Adaptive Design Under a Phase Synchronization Mismatch . . . . .</b>	<b>88</b>
5.1	Introduction . . . . .	89
5.2	Radar Model . . . . .	92
5.2.1	Measurement Model . . . . .	92
5.2.2	Statistical Model . . . . .	95
5.3	Detection and Estimation Algorithm . . . . .	97
5.4	Adaptive Design . . . . .	102
5.5	Numerical Examples . . . . .	105
5.6	Summary . . . . .	112
<b>6</b>	<b>MIMO Radar Sensitivity Analysis for Target Detection . . . . .</b>	<b>115</b>
6.1	Introduction . . . . .	116
6.2	Radar Model . . . . .	117
6.2.1	Measurement Model . . . . .	117
6.2.2	Statistical Model . . . . .	120
6.3	Statistical Decision Test for Target Detection . . . . .	122
6.3.1	Wald Test . . . . .	122
6.3.2	Estimation Algorithm . . . . .	124

6.3.3	Computation of the Cramér-Rao Bound . . . . .	127
6.3.4	Detection Performance . . . . .	129
6.4	Numerical Examples . . . . .	131
6.5	Summary . . . . .	134
<b>7</b>	<b>Conclusions and Future Work . . . . .</b>	<b>139</b>
7.1	Conclusions . . . . .	139
7.2	Future Work . . . . .	142
<b>Appendix A</b>	<b>Definitions of Block Matrix Operators . . . . .</b>	<b>145</b>
<b>Appendix B</b>	<b>Computation of Matrix <math>C</math> in (3.23) . . . . .</b>	<b>147</b>
<b>Appendix C</b>	<b>Computation of the matrix <math>P</math> in (4.18) . . . . .</b>	<b>149</b>
<b>Appendix D</b>	<b>Proof of the identity in (5.15) . . . . .</b>	<b>151</b>
<b>Appendix E</b>	<b>Proof of the identity in (5.18) . . . . .</b>	<b>154</b>
<b>Appendix F</b>	<b>Proof of Theorem 5.1 . . . . .</b>	<b>157</b>
<b>Appendix G</b>	<b>Solution to (5.25) for <math>M = 2</math> and <math>N = 2, 4</math> . . . . .</b>	<b>159</b>
<b>Appendix H</b>	<b>Computation of the Conditional Mean and Covariance in (6.12) . . . . .</b>	<b>161</b>
<b>Appendix I</b>	<b>Computation of the Elements of the Fisher Information Matrix in (6.14) . . . . .</b>	<b>163</b>
<b>References</b>	<b>. . . . .</b>	<b>167</b>
<b>Vita</b>	<b>. . . . .</b>	<b>178</b>

# List of Tables

3.1	Directivity gains of the antenna arrays in the desired direction $\theta = 0^\circ$ and $\phi = 90^\circ$ (dB) . . . . .	66
3.2	Half-power beamwidths of the antenna arrays (degrees) . . . . .	67

# List of Figures

1.1	MIMO radar with colocated antennas for 2 transmitters (Ts) and 3 receivers (Rs). . . . .	5
1.2	MIMO radar with widely separated antennas for 2 transmitters (Ts) and 3 receivers (Rs). . . . .	6
2.1	(a) Anatomy of the female <i>Ormia ochracea</i> 's ear. Top: side view of the fly. Bottom: front view of the ear after the head was removed. (b) Top: front view of the ear after the head was removed. Bottom: mechanical model [1]. . . . .	14
2.2	Effect of coupling on the impulse responses of the Ormia's two ears for 45° incident angle. . . . .	15
2.3	Effect of coupling on the amplitude responses of the Ormia's two ears for 45° incident angle. . . . .	17
2.4	Effect of coupling on the phase responses of the Ormia's two ears (blue, red) for 45° incident angle. . . . .	18
2.5	Measurement model. . . . .	19
2.6	Square-root of the Cramér-Rao bound on direction of arrival estimation vs. SNR. . . . .	22
3.1	Amplitude responses of the Ormia ochracea's two ears. (a) Coupled system. (b) Uncoupled system. . . . .	33
3.2	Phase responses of the Ormia ochracea's two ears. (a) Coupled system. (b) Uncoupled system. . . . .	33
3.3	(a) Amplitude and (b) phase responses of the converted system. . . . .	34
3.4	Two-input two-output filter representation of the Ormia's coupled ears' response. . . . .	38
3.5	(a) Circular array and a source . (b) Angular Error . . . . .	45
3.6	Square-root of the mean-square error in the direction estimation and corresponding Cramér-Rao bounds vs. number of time samples for the standard (blue) and BIC (red) uniform linear arrays with different inter-element spacings, $d$ , and SNR=-10 dB. (a) $d = 0.1\lambda$ . (b) $d = 0.2\lambda$ . . . . .	50
3.7	Square-root of the Cramér-Rao bound on direction of arrival estimation vs. SNR for standard and BIC uniform linear arrays with $d = 0.1\lambda$ and $d = 0.2\lambda$ inter-element spacings and $N=10$ time samples. . . . .	51

3.8	Square-root of the mean-square error in the direction estimation and corresponding Cramér-Rao bounds vs. number of time samples for the standard (blue) and BIC (red) uniform linear arrays with different inter-element spacings, $d$ , and SNR=-10 dB. (a) $d = 0.1\lambda$ . (b) $d = 0.2\lambda$ . . . . .	52
3.9	Square-root of the Cramér-Rao bound on direction of arrival estimation vs. SNR for standard (blue), and BIC (red) uniform linear arrays with different inter-element spacings, $d = 0.1\lambda$ and $d = 0.2\lambda$ , and $N=10$ time samples. . . . .	54
3.10	Square-root of the Cramér-Rao bound on direction of arrival estimation vs. direction of arrival (azimuth) for standard (blue), and BIC (red) uniform linear arrays with different inter-element spacings, $d = 0.1\lambda$ and $d = 0.2\lambda$ , $N=10$ time samples, and SNR= -10 dB. . . . .	54
3.11	Square-root of the Cramér-Rao bound on direction of arrival estimation vs. inter-element spacing ( $d$ ) for standard (blue), and BIC (red) uniform linear arrays, SNR= -10 dB and $N=10$ time samples. . . . .	55
3.12	Square-root of the Cramér-Rao bound on direction of arrival estimation vs. SNR for standard (blue), and BIC (red) uniform linear arrays with different number of sources, $M$ , $N=10$ time samples. (a) $M = 2, 3$ . (b) $M = 4$ . . . . .	56
3.13	Square-root of the Cramér-Rao bound on direction of arrival estimation vs. SNR for the standard (blue) and BIC (red) circular arrays of radius (a) $r = 0.1\lambda$ (b) $r = 0.2\lambda$ and $N=10$ time samples. . . . .	57
3.14	Square-root of the mean-square angular error vs. SNR for the standard (blue), and BIC (red) circular arrays with different radius values, $r = 0.1\lambda$ and $r = 0.2\lambda$ , $N=10$ time samples. . . . .	58
3.15	Square-root of the mean-square angular error vs. DOA angle (elevation) for the standard (blue), and BIC (red) circular arrays with different radius values, $r = 0.1\lambda$ and $r = 0.2\lambda$ , $N=10$ time samples, and SNR= -10 dB. . . . .	58
3.16	Square-root of the mean-square angular error vs. SNR for the standard (blue), and BIC (red) circular arrays with different number of sources, $M$ , $N=10$ time samples. (a) $M = 2, 3$ (b) $M = 4$ . . . . .	59
3.17	Far-field radiation geometry of $M$ -element antenna array. . . . .	60
3.18	Power patterns of the uniform ordinary end-fire antenna arrays using standard (blue), and BIC (green) for (a) $d = 0.25\lambda$ , (b) $d = 0.1\lambda$ inter-element spacings. The bottom halves of the figures present the half-power beamwidth. . . . .	65
3.19	Power patterns of the binomial end-fire antenna arrays using standard (blue), and BIC (green) for (a) $d = 0.25\lambda$ , (b) $d = 0.1\lambda$ inter-element spacings. The bottom halves of the figures present the half-power beamwidth. . . . .	66
4.1	MIMO antenna system with $M$ transmitters and $N$ receivers. . . . .	84
4.2	(a) Receiver operating characteristics of MIMO and conventional phased-array radar (Conv.). (b) Receiver operating characteristics of MIMO radar with and without adaptive energy allocation. . . . .	85

5.1	Probability density function of von-Mises distribution with shape parameter $\Delta$ . . . . .	91
5.2	MIMO antenna system with $M = 2$ transmitters and $N = 3$ receivers. . .	106
5.3	Receiver operating characteristics of MIMO radar for different number of receivers and shape parameter values, unknown shape parameter $\Delta$ . . . . .	107
5.4	Receiver operating characteristics of MIMO radar with and without adaptive energy allocation for (a) $\Delta = 5$ ; (b) $\Delta = 25$ ; (c) $\Delta = 100$ , unknown shape parameter $\Delta$ . . . . .	109
5.5	Receiver operating characteristics of MIMO radar for different number of receivers and shape parameter values, known shape parameter $\Delta$ . . . . .	110
5.6	Receiver operating characteristics of MIMO radar with and without adaptive energy allocation for (a) $\Delta = 5$ ; (b) $\Delta = 25$ ; (c) $\Delta = 100$ , and known shape parameter $\Delta$ . . . . .	111
5.7	Probability of detection vs. signal-to-noise ratio for a fixed PFA= $10^{-2}$ , and known shape parameter $\Delta$ . . . . .	112
5.8	Comparison of the receiver operating characteristics of the coherent MIMO radar and MIMO radar phase error (GLRT) detectors, for known shape parameter $\Delta$ . . . . .	113
5.9	Receiver operating characteristics of MIMO radar under model mismatch (a) MIMO $2 \times 2$ (b) MIMO $2 \times 4$ . . . . .	113
6.1	MIMO antenna system with $M$ transmitters and $N$ receivers. . . . .	131
6.2	Probability density function of the test statistics under $\mathcal{H}_1$ for different ACCL values and (a) MIMO $2 \times 3$ (b) MIMO $3 \times 3$ (c) MIMO $3 \times 5$ configurations. . . . .	136
6.3	Receiver operating characteristics of the target detector for different ACCL values and (a) MIMO $2 \times 3$ (b) MIMO $3 \times 3$ (c) MIMO $3 \times 5$ configurations. . . . .	137
6.4	Probability of detection vs. SNR for different ACCL values ( $P_{FA} = 0.01$ ). . . . .	138
B.1	Circuit model of the $i^{th}$ antenna element in the transmitting mode. . . . .	147

# List of Abbreviations

ACCL	Average cross-correlation level
AF	Array factor
BIC	Biologically inspired coupling
CCL	Cross-correlation level
CFAR	Constant false alarm rate
COI	Cell of interest
CPI	Coherent processing interval
CRB	Cramér-Rao Bound
DOA	Direction-of-arrival
EF	Element factor
EM	Expectation-maximization
FIM	Fisher information matrix
GMANOVA	Generalized multivariate analysis of variance
GLRT	Generalized likelihood ratio test
MI	Mutual information
MIMO	Multiple-input multiple-output
MLE	Maximum likelihood estimate
MMSE	Minimum mean-square error
MSAE	Mean-square angular error
PLL	Phase-locked loop
PRF	Pulse repetition frequency
PRI	Pulse repetition interval
PX-EM	Parameter-expanded expectation-maximization
RCS	Radar cross section
RMSE	Root mean squared error
ROC	Receiver operating characteristic
SCR	Signal-to-clutter ratio
SNR	Signal-to-noise ratio
UCA	Uniform circular array
ULA	Uniform linear array

# List of Notations

$a$	lowercase math italic denotes a scalar
$\mathbf{a}$	lowercase bold denotes a vector $\mathbf{a} \in \mathbb{C}^n$
$\mathbf{A}$	uppercase bold denotes a matrix $\mathbf{A} \in \mathbb{C}^{m \times n}$
$ \mathbf{A} $	determinant of $\mathbf{A}$
$[\mathbf{A}]_{(i,j)}$	$(i, j)$ -th element of $\mathbf{A}$
$\mathbf{A}^*$	conjugate of $\mathbf{A}$
$\mathbf{A}^T$	transpose of $\mathbf{A}$
$\mathbf{A}^H$	conjugate-transpose (Hermitian) of $\mathbf{A}$
$\mathbf{A}^-$	generalized inverse of $\mathbf{A}$ such that $\mathbf{A}\mathbf{A}^-\mathbf{A} = \mathbf{A}$
$\mathbf{A}^\dagger$	pseudo-inverse of $\mathbf{A}$ , defined as $\mathbf{A}^\dagger = (\mathbf{A}^H \mathbf{A})^{-1} \mathbf{A}^H$
$\text{vec}(\mathbf{A})$	forms a column vector of length $mn$ by stacking the columns of $\mathbf{A}$
$\text{tr}(\mathbf{A})$	trace of square matrix $\mathbf{A} \in \mathbb{C}^{n \times n}$
$\text{diag}(\dots)$	forms a square matrix with non-zero entries only on the main diagonal
$\text{blkdiag}(\dots)$	forms a square matrix with non-zero matrix entries only on the main diagonal
$\mathbf{I}_n$	identity matrix of dimension $n$
$\text{Re}\{\cdot\}$	real part of a complex quantity
$\text{Im}\{\cdot\}$	imaginary part of a complex quantity
$\otimes$	Kronecker product operator
$\odot$	element-wise Hadamard product operator
$\mathcal{N}$	Gaussian distribution
$\mathbb{C}\mathcal{N}_k$	complex Gaussian distribution of a vector of length $k$
$\mathbb{C}\chi_n^2$	complex chi-square distribution with $n$ degrees of freedom



# Chapter 1

## Introduction

In this dissertation we present our research on biologically inspired sensing, specifically inspired by the hearing system of the parasitoid fly *Ormia ochracea*, and then develop multi-input multi-output (MIMO) radar applications in array signal processing. In this chapter, we first discuss sound source localization for animals, with a focus on the mechanically coupled ears of a female *Ormia ochracea*. As a part of our research on biologically inspired sensing, we propose to design a coupled antenna system inspired by the unique structure of the female *Ormia*'s ears. In the rest of this chapter, we introduce the MIMO processing approach for radar signal processing. For MIMO radar, our research addresses target detection in non-homogeneous clutter, the effect of phase synchronization mismatch between transmitter and receiver pairs on the detection performance, and sensitivity analysis for target detection performance.

### 1.1 Biologically Inspired Sensing

For animals, source localization through directional hearing relies on the interaural acoustic cues: interaural time differences (ITD) and interaural intensity differences

(IID) of the incoming sound source [2]. The ears of large animals are acoustically isolated from each other, i.e., the organs are located on opposite sides of the head or body. For these animals the distance between the hearing organs provides relatively large ITDs between the ipsilateral and contralateral ears (the ears closest to and furthest from the sound source, respectively). Moreover, a large body or head, with a size comparable to the incoming signals wavelength (above one tenth of the wavelength [3]), diffracts the incoming sound and increases the IIDs between received signals. Therefore, these big interaural differences can be detected by the hearing systems of large animals such as monkeys [4], [5]; human beings [6],[7]; cats [8]; horses [9]; and pigs [10].

On the other hand, small animals may sense no diffractive effect in the incoming signal, and hence have almost no IID between their two ears. Moreover, due to the closely spaced ears, the ITD drops below the level where it can be processed by the nervous systems of the animals. Therefore many small animals develop a mechanism to improve these interaural differences [11]. A pressure difference receiver is the most common mechanism employed by many animals in this category. In animals with pressure difference receivers, the ears are acoustically coupled to each other through internal air passages. Thus, the resulting force stimulating the eardrum is the difference between the internal and external acoustic pressures, and hence the name pressure difference receiver [2]. This structure amplifies the ITDs and IIDs and improves the directional hearing performances of many small animals [12]-[17].

We focus on the hearing system of a parasitoid fly *Ormia ochracea*. For reproduction, a female *Ormia* acoustically locates a male field cricket and deposits her larvae on or near the cricket [18]. The localization occurs at night, relying on the cricket's mating call [19], [20]. The fly is very small and its ears are very closely separated, and

physically connected to each other, resulting in ITDs as small as 4 microseconds [21], [22]. Moreover, there is a big incompatibility between the wavelength of the mating call (a relatively pure frequency peak around 5KHz, with a resulting wavelength of 7 cm) and the size of the fly’s hearing organ (around 1.5 mm), resulting in negligible IIDs [3]. It is theorized that these extremely small interaural differences can not be processed by the nervous system of the Ormia. However, confounding theory, the fly still locates the cricket very accurately, with as low as  $2^\circ$  of error in direction estimation [23]. Female Ormias have a mechanical structure that connects their two ears, and it is this structure that amplifies the interaural differences to improve the localization accuracy [1], [24], [25]. This mechanical coupling is unique to the female Ormia [2, Chapter 2]; even the male Ormias do not have anything similar [22].

In our research, we first quantitatively demonstrate the localization performance of the female Ormia. Then, inspired by the Ormia’s mechanically coupled ears, we develop an antenna array with coupling.

### **1.1.1 Performance of the Ormia Ochracea’s Coupled Ears**

We quantitatively demonstrate the localization accuracy of a female Ormia ochracea [26]. To feed its larvae, the female Ormia is able to locate a cricket’s mating call despite the small distance between its ears compared with the incoming signal’s wavelength. This phenomenon has been explained by the mechanical coupling between the ears. In this research, we first show that the coupling enhances the differences in the frequency responses of the ears to the incoming source signals. Then, by computing the Cramèr-Rao bound (CRB) on the direction of arrival (DOA) estimation error, we analyze the source localization accuracy of the Ormia. We rewrite the differential

equations of the mechanical system in a state-space model, and calculate the ears' impulse and frequency responses. Using the spectral properties of the system, we asymptotically compute the CRB for multiple stochastic sources with unknown directions and spectra. With numerical examples, we compare the CRB for the coupled and the uncoupled cases, illustrating the effect of the coupling on reducing the errors in estimating the DOA.

### 1.1.2 Biologically Inspired Antenna Array

We propose to design a small-size antenna array having high localization performance, inspired by the female Ormia's coupled ears [27]-[30]. The mechanical coupling between the Ormia's ears has been modeled by a pair of differential equations. We first solve the differential equations governing the Ormia's ear response, and convert the response to the pre-specified radio frequencies. Using the converted response, we design passive and active transmitting antenna arrays. For the passive antenna array, we implement the biologically inspired coupling (BIC) as a multi-input multi-output filter on a uniform linear antenna array output. We derive the maximum likelihood estimates (MLEs) of source DOAs, and compute the corresponding CRBs on the DOA estimation error as a performance measure. We also consider a circular array configuration and compute the mean-square angular error bound on the three-dimensional localization accuracy. For the active antenna system with BIC, we obtain the array factor of the antenna array with BIC at the desired radio frequencies. We compute the radiation intensity of this system and analyze its half-power beamwidth, sidelobe levels, and directivity of the radiation pattern. Moreover, we propose an algorithm to optimally choose the BIC for maximum localization and radiation performance. We use numerical simulations to demonstrate the advantages of the coupling effect.

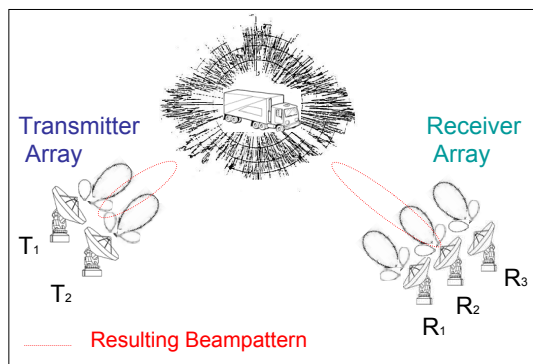


Figure 1.1: MIMO radar with collocated antennas for 2 transmitters (Ts) and 3 receivers (Rs).

## 1.2 Multi-Input Multi-Output Radar

Multi-input multi-output (MIMO) radar is a remote sensing system that uses multiple transmitters. It jointly processes the received signal from a moving or stationary target at multiple receivers for detection, and for identification of the target's range, direction or speed in the presence of possible reflections from the target environment, usually referred to as clutter [31], [32]. Over the last decade, the MIMO approach for radar processing has drawn a great deal of attention from researchers and has been applied to various radar scenarios and problems. MIMO radar has been studied using both collocated [33] and widely separated antennas [34].

With collocated antennas, a MIMO radar is capable of transmitting multiple signals, which can be uncorrelated or correlated with each other, providing transmitted waveform diversity. In this configuration every transmitter and receiver pair illuminates the target from the same direction, so that the target returns are fully correlated for all the pairs, as shown in Fig. 1.1. The advantages of such systems have been well studied. They include improved parameter identifiability [35], improved detection

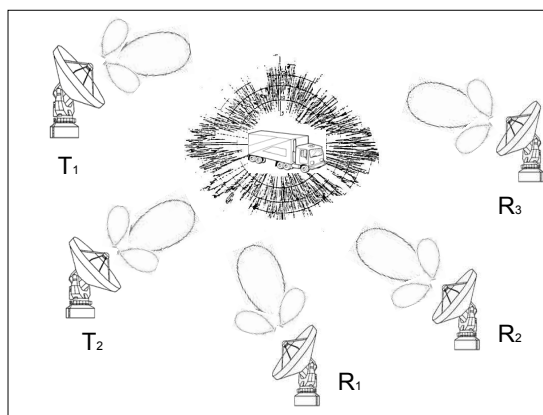


Figure 1.2: MIMO radar with widely separated antennas for 2 transmitters (Ts) and 3 receivers (Rs).

performance and higher resolution [36], higher sensitivity for detecting moving targets [37], a radiation pattern with lower side lobes and better suppression [38], and increased degrees of freedom for transmission beamforming [39]-[42].

MIMO radars with widely separated antennas exploit spatial diversity and hence the spatial properties of the target's radar cross section (RCS). The RCSs of complex radar targets are quickly changing functions of the angle aspect [43]. These target scintillations cause signal fading, which deteriorates the radar performance [32], [44]. When the transmitters are sufficiently separated, the multiple signals illuminate the target from de-correlated angles, and hence each signal carries independent information, as seen in Fig. 1.2 [45]. This spatial diversity allows the radar systems to localize the target with high resolution [46], to improve the target parameter estimation [47]-[50], and improve detection in homogeneous and inhomogeneous clutter [45]-[53]. It also enhances tracking performance [54], and the ability to handle slow moving targets by exploiting Doppler estimates from multiple directions [51], [55].

In this dissertation, we focus on MIMO radar with widely separated antennas. From here on, when we use the term MIMO radar, we refer to a MIMO radar with widely separated antennas. We first solve the target detection problem for a MIMO radar in the presence of sea or foliage clutter (compound-Gaussian clutter). We then continue with more practical issues related to MIMO radar. Under appropriate assumptions, everything seems to work very well for a theoretical MIMO radar system. However, in practice MIMO radar suffers from the lack of phase synchronization among the transmitter and receiver pairs [56], [57] and the non-orthogonality of the received signals [58]. We address these issues in this dissertation by developing more robust target detectors that consider the effect of phase synchronization mismatch between transmitter and receiver pairs, and by demonstrating the sensitivity of the target detection performance to changes in the cross-correlation levels among the received signals.

### **1.2.1 Adaptive MIMO Radar Design and Detection in Compound-Gaussian Clutter**

MIMO radars are useful to discriminate a target from clutter using the spatial diversity of the scatterers in the illuminated scene. We consider the detection of targets in compound-Gaussian clutter, to fit such scenarios as scatterers with heavy-tailed distributions for high-resolution and/or low-grazing-angle radars in the presence of sea or foliage clutter [59], [60], [61]. First, we introduce a data model using an inverse gamma distribution to represent the clutter texture [62]. Then, we apply the parameter-expanded expectation-maximization (PX-EM) algorithm to estimate the

clutter texture and speckle as well as the target parameters [63]. We develop a statistical decision test using these estimates and approximate its statistical characteristics. Based on this test, we propose an algorithm that adaptively distributes the total transmitted energy among the transmitters to improve the detection performance.

### **1.2.2 MIMO Radar Detection and Adaptive Design Under a Phase Synchronization Mismatch**

We consider the problem of target detection for MIMO radar in the presence of a phase synchronization mismatch between the transmitter and receiver pairs [64], [65]. Such mismatch often occurs due to imperfect knowledge of the locations and local oscillator characteristics of the antennas. First, we introduce a data model using a von-Mises distribution to represent the phase error terms [66]. Then, we propose a method based on the expectation-maximization algorithm to estimate the error distribution parameter, target returns, and noise variance [67]. We develop a generalized likelihood ratio test target detector using these estimates [68]. Based on the mutual information [69] between the radar measurements and received target returns (and hence the phase error), we propose an algorithm to adaptively distribute the total transmitted energy among the transmitters. Using numerical simulations, we demonstrate that the adaptive energy allocation, the increase in the phase information, and the realistic measurement modeling improve detection performance.



### 1.2.3 MIMO Radar Sensitivity Analysis for Target Detection

For MIMO radar, we consider the effect of the imperfect separability of the received signals on detection performance [70]. In practice, mutual orthogonality among the received signals cannot be achieved for all Doppler and delay pairs [58]. We introduce a data model considering the correlation among the data from different transmitter-receiver pairs as unknown parameters. We formulate a method to estimate the target, correlation, and noise parameters, and then use these estimates to develop a statistical decision test. Using the asymptotical statistical characteristics and the numerical performance of the test, we analyze the sensitivity of the MIMO radar with respect to changes in the cross-correlation levels of the measurements. Using numerical examples, we demonstrate the effect of the increase in the correlation among the received signals from different transmitters on the detection performance.

### 1.2.4 Outline of the Dissertation

The rest of the dissertation is organized as follows. In Chapter 2, we quantitatively analyze the localization accuracy of a female *Ormia ochracea*'s coupled ears, using a statistical approach. In Chapter 3, inspired by the coupled ears of *Ormia ochracea*, we propose to develop an antenna array for improved localization accuracy and radiation performance. Then, we continue with our results on target detection using MIMO radar with widely separated antennas. First, in Chapter 4, we address the target detection problem in the presence of sea or foliage clutter. Then, we consider the practical limitations of MIMO radar processing. In this context, in Chapter 5, we develop a more robust target detector, including the possible phase synchronization errors between the transmitter and receiver antenna pairs. Then, in Chapter 6, we

analyze the sensitivity of the target detection performance of a MIMO radar system to changes in the cross-correlation levels of the received signals from different transmitters. Finally, we summarize our contributions and talk about possible future work in Chapter 7.

## Chapter 2

# Performance Analysis of the Ormia Ochracea's Coupled Ears<sup>1</sup>

The female Ormia ochracea, a parasitoid fly, locates male crickets very accurately as part of its reproduction strategy. This is unexpected, as the distance between its ears is much smaller than the wavelength of the cricket's mating call. This phenomenon has been explained by a mechanical coupling between the ears, which is represented by a pair of differential equations. We analytically show the significance of the mechanical coupling between the O. ochracea's ears for localization accuracy. We first represent the differential equations in state space, then solve the model and illustrate its time and spectral properties. We find the impulse and frequency responses of the fly's ears, and compare these responses for coupled and uncoupled versions of the system to demonstrate the effect of coupling on the intensity and time differences between the two ears. We then develop a statistical model with multiple stochastic sources and measurement noise to analyze the effect of the coupling on localization performance. We compute the asymptotic Cramér-Rao bound (CRB) on estimating the direction

---

<sup>1</sup>Based on M. Akcakaya and A. Nehorai, "Performance Analysis of the Ormia Ochracea's Coupled Ears" *The Journal of the Acoustical Society of America*, vol. 124, pp. 2100–2105, Oct. 2008. ©[2008] Acoustical Society of America.

of arrival (DOA) of a source in two-dimensional (2D) space. Finally, we present numerical examples which compare the CRB's of the coupled and the uncoupled systems, showing the improvement in the localization accuracy due to coupling.

## 2.1 Introduction

Most available array processing methods employ the time differences of arrival between the elements of a sensor array to estimate the directions of arrival (DOA) of the incoming waves. Since the performance of such arrays is directly proportional to the size of the array's aperture, large aperture arrays are often required. However, this is costly and may be impractical in many tactical and mobile applications. This chapter demonstrates a high-performance array with very small aperture, namely of the parasitoid fly called *Ormia Ochracea*.

A female *O. ochracea* is known to have a mechanical coupling between its ears to enhance its hearing. There are also other small animals having interactions between their ears for the same purpose [11], but the mechanical coupling is unique for the *O. ochracea*. This coupling is necessary for the *O. ochracea*'s perpetuation. The female *O. ochracea* must locate and deposit her parasitic maggots on or near a male field cricket, relying on the cricket's mating call which is relatively pure in frequency (peak frequency 4.8 kHz). However, there is a tremendous incompatibility between the distance between the two ears ( $\approx 1.2$  mm) and the wavelength ( $\approx 7$  cm) of the cricket's mating call. This disaccord leads to extremely small interaural intensity and time of arrival differences between the ipsilateral and contralateral ears. It is believed that the coupling mechanism magnifies these binaural differences and subsequently improves the sound source localization accuracy [1], [21]-[25].

A system which models the mechanical coupling between the ears of the *O. ochracea* is introduced in [1]. The authors of [1] show experimentally that this model is well-matched to the fly's ear in terms of frequency and transient responses. In the following, using this mechanical model, we quantitatively analyze the effect of the coupling on the localization accuracy of the *O. ochracea*.

## 2.2 Modeling

In this section, we briefly review the anatomy of the ear of the female *O. ochracea* and describe the mechanical model, associating its parameters with the parts of the ear following [1]. Then, to demonstrate the effect of the coupling, we compute and compare the impulse and frequency responses of the coupled and the uncoupled systems for a far-field source.

Fig. 2.1(a) shows the female *O. ochracea* and its ear structure. Observe that:

- The ear is located on the front face of the thorax, behind the head.
- Prosternal tympanal membranes serve for hearing.
- Bulbae acustica (sensory organs) are connected to the tympanal pit.
- The tympanal pits and the pivot point are connected to each other by a cuticular structure referred as intertympanal bridge. This improves the usage of interaural differences.

A simple mechanical model, composed of springs and dash-pots, is proposed in [1] to explain the mechanical coupling between the ears (Fig. 2.1(b)) with  $k_i$ 's and  $c_i$ 's

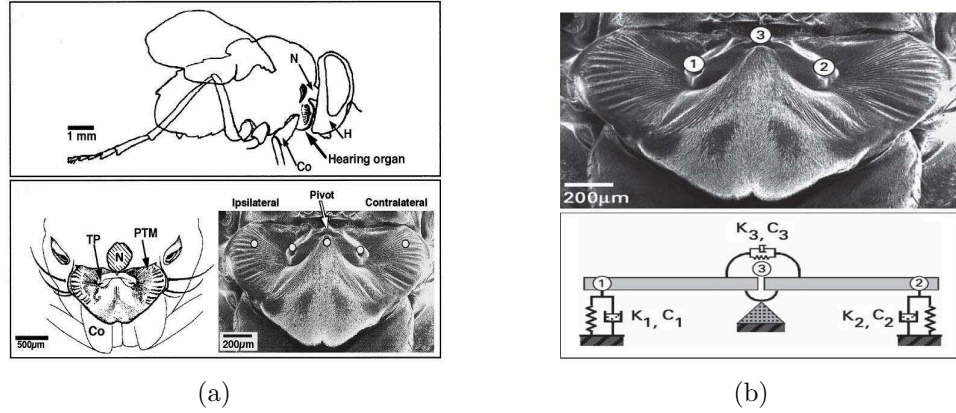


Figure 2.1: (a) Anatomy of the female *Ormia ochracea*'s ear. Top: side view of the fly. Bottom: front view of the ear after the head was removed. (b) Top: front view of the ear after the head was removed. Bottom: mechanical model [1].

( $i = 1, 2, 3$ ) as the spring and dash-pot constants, respectively. In this model, the intertympanal bridge is assumed to consist of two rigid bars connected at the pivot point through a coupling spring  $k_3$  and dash-pot  $c_3$ . The springs and dash-pots at the extreme ends of the bridge approximately represent the dynamic properties of the tympanal membranes, bulbae acustica and surrounding structures. The numerical values of the above model were empirically found for  $45^\circ$  incident angle, but they were shown to hold also for a wide range of angles [1].

We can write the differential equations for the mechanical model in Fig. 2.1(b) in matrix form following [1]:

$$\begin{bmatrix} k_1 + k_3 & k_3 \\ k_3 & k_2 + k_3 \end{bmatrix} \begin{bmatrix} z_1(t) \\ z_2(t) \end{bmatrix} + \begin{bmatrix} c_1 + c_3 & c_3 \\ c_3 & c_2 + c_3 \end{bmatrix} \begin{bmatrix} \dot{z}_1(t) \\ \dot{z}_2(t) \end{bmatrix} + \quad (2.1)$$

$$\begin{bmatrix} m & 0 \\ 0 & m \end{bmatrix} \begin{bmatrix} \ddot{z}_1(t) \\ \ddot{z}_2(t) \end{bmatrix} = \begin{bmatrix} f_1(t, \Delta) \\ f_2(t, \Delta) \end{bmatrix} = \mathbf{f}(t, \Delta) \quad , \quad (2.2)$$

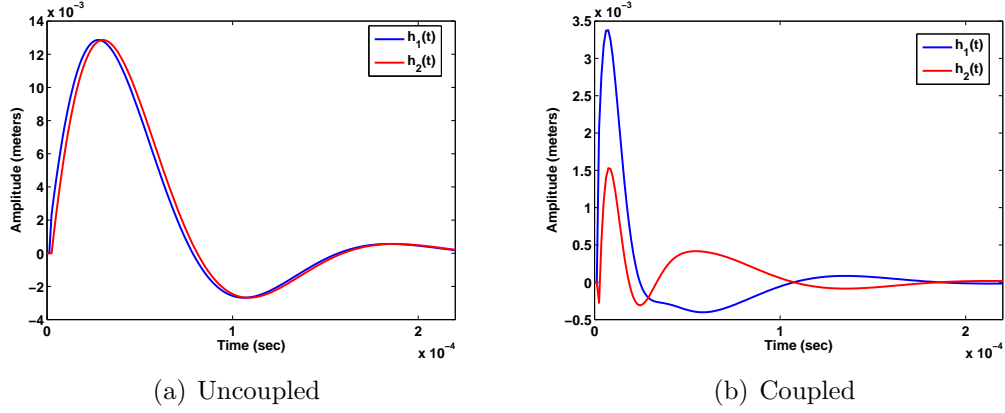


Figure 2.2: Effect of coupling on the impulse responses of the Ormia's two ears for  $45^\circ$  incident angle.

where

- $f_i(t, \Delta) = p_i(t, \Delta) * s$ ,  $i = 1, 2$ , where  $p_1(t, \Delta)$  and  $p_2(t, \Delta)$  both correspond to the same input sound source and are the pressure waves at the ipsilateral and the contralateral ears, respectively, and  $s$  is the surface area of each tympanal membrane (see Fig. 2.1)
- $z_1(t)$  and  $z_2(t)$  are displacements at the first and the second ends of the intertympanal bridge, respectively (see Fig.2.1(b))
- $m$  is the effective mass of all moving elements and it is assumed to be concentrated at each end of the intertympanal bridge, and
- $\Delta$  corresponds to the time difference of arrival between the two ears:  $\Delta = d \cos \phi / v$ , where  $\phi \in [-90^\circ, 90^\circ]$  is the direction of arrival,  $d$  is the distance between force locations, and  $v$  is the speed of sound, roughly 344m/s.

In order to find the solutions for  $z_1(t)$  and  $z_2(t)$ , we write (2.2) as a state space model:

$$\begin{aligned}\dot{\mathbf{x}}(t) &= \mathbf{A}\mathbf{x}(t) + \mathbf{B}\mathbf{f}(t, \Delta), \\ \mathbf{y}(t) &= \mathbf{C}\mathbf{x}(t),\end{aligned}\tag{2.3}$$

where  $\mathbf{x}(t) = [x_1(t), x_2(t), x_3(t), x_4(t)]^T = [z_1(t), z_2(t), \dot{z}_1(t), \dot{z}_2(t)]^T$  is the state variable vector,  $\mathbf{A}$  and  $\mathbf{B}$  are constant matrices which are functions of the model parameters in (2.2),  $\mathbf{C}$  is a constant matrix depending on the observations; see, for example [71].  $\mathbf{C}$  is chosen such that  $\mathbf{y}(t) = [y_1(t), y_2(t)]^T = [z_1(t), z_2(t)]^T$ . Using the variation of constants formula [72], the solution for the state space model can be computed by

$$\begin{aligned}\mathbf{x}(t) &= \Phi(t, t_0)\mathbf{x}(t_0) + \int_{t_0}^t \Phi(t, \tau)\mathbf{B}\mathbf{f}(\tau, \Delta)d\tau, \\ \mathbf{y}(t) &= \mathbf{C}\mathbf{x}(t).\end{aligned}\tag{2.4}$$

Here,  $t_0$  is the initial time referencing the instant when the input signal first arrives at the ipsilateral ear, and  $\Phi(t, t_0)$  is the transition matrix depending on the matrix  $\mathbf{A}$ .

Figs. 2.2, 2.3, and 2.4 show the impulse, amplitude and phase responses, respectively for both the coupled and uncoupled systems. We obtain the uncoupled system by setting the coupling parameters  $k_3$  and  $c_3$  to zero. Fig. 2.2 illustrates the impulse responses,  $\mathbf{h}(t, \Delta) = [h_1(t, \Delta), h_2(t, \Delta)]^T$ , calculated for  $\phi = 45^\circ$  using Dirac delta function in (2.4) as an input. The responses  $h_1(t, \Delta)$  and  $h_2(t, \Delta)$  correspond to the ipsilateral and contralateral ears, respectively. It is apparent that the interaural differences between the two ear outputs are enhanced for the coupled system (Figs. 2.2(a)



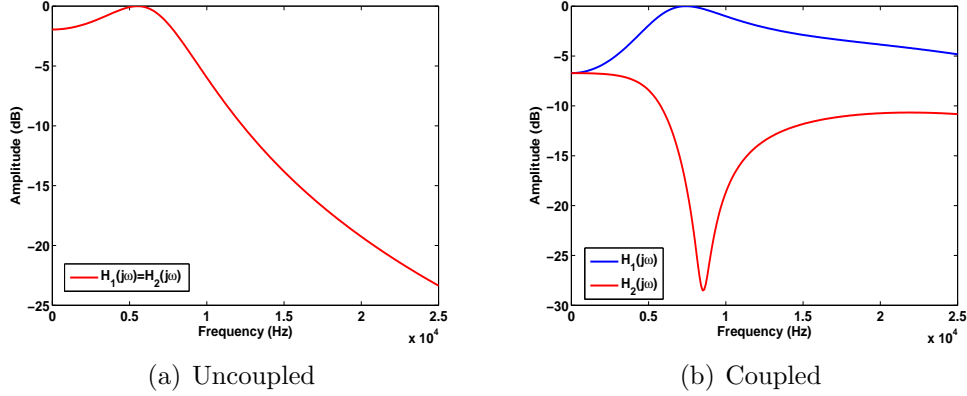


Figure 2.3: Effect of coupling on the amplitude responses of the Ormia’s two ears for  $45^\circ$  incident angle.

and 2.2(b)). These differences can be explained more clearly in the frequency domain. Therefore, the amplitude and phase responses are calculated by taking the discrete time fourier transform (DTFT) [73] of the sampled impulse responses. Fig. 2.3 shows that the gap between ipsilateral ( $H_1(e^{j\omega}, \Delta)$ ) and the contralateral ( $H_2(e^{j\omega}, \Delta)$ ) amplitude responses is bigger for the coupled system (Figs. 2.3(a) and 2.3(b)). This confirms the improvement of the intensity differences between the ear outputs. Similarly, Fig. 2.4 demonstrates how the phase difference between the responses of the two ears are amplified, so is the difference in arrival time of the sound source to the two ears, for coupled system (Figs. 2.4(a) and 2.4(b)). This analysis may explain how the extremely small interaural differences in intensity and arrival time are increased by the coupling to a level that the *O. ochracea* could use the improved binaural cues to process the information more effectively.

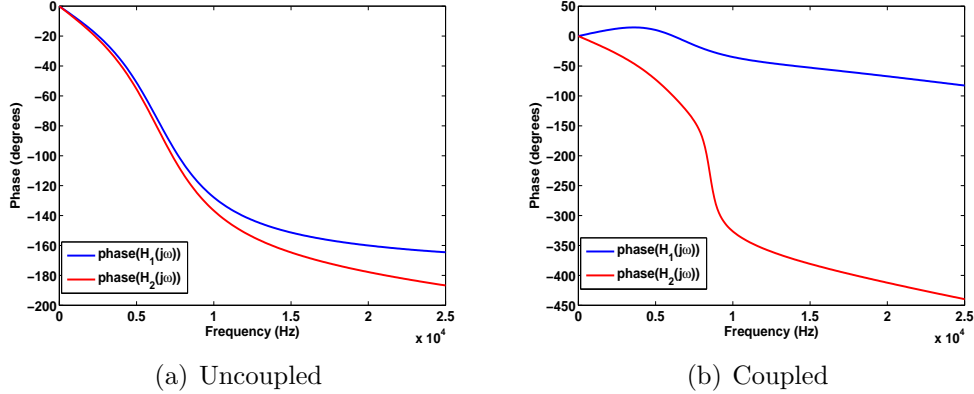


Figure 2.4: Effect of coupling on the phase responses of the Ormia's two ears (blue, red) for  $45^\circ$  incident angle.

## 2.3 Performance Analysis

In this section, we present a statistical model for measurements and compute the Cramèr-Rao bound (CRB) on DOA estimation using the model in (2.4).

### 2.3.1 Statistical Model

The model consists of  $M$  multiple stochastic inputs  $p_m(t)$  ( $m = 1, 2, \dots, M$ ) and additive measurement noise  $\mathbf{e}(t) = [e_1(t), e_2(t)]^T$  with  $e_1(t)$  and  $e_2(t)$  corresponding to the measurement noise at the ipsilateral and contralateral ears, respectively (Fig. 2.5). That is,  $M$  different angles for  $M$  different input signals are chosen to model the environment. This model gives rise to:

$$\mathbf{y}(t, \Delta) = \sum_{m=1}^M p_m(t) * h(t, \Delta_m) + \mathbf{e}(t), \quad t = 1, 2, \dots, N, \quad (2.5)$$

where  $\Delta = [\Delta_1, \Delta_2, \dots, \Delta_M]^T$ , and  $\Delta_m$  is the time difference between two ears corresponding to the incidence angle  $\phi_m$  of the input signal  $p_m(t)$ . The impulse response

$h(t, \Delta_m)$  depends on the angle  $\phi_m$ , due to the fact that for any signal  $p_m(t)$  the equality  $p_m(t - \Delta_m) * h(t) = p_m(t) * h(t - \Delta_m)$  always holds. Thus, it can be concluded that the system has different impulse responses and respective frequency responses for different incidence angles.

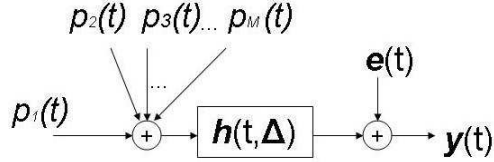


Figure 2.5: Measurement model.

We assume that  $p_m(t)$  and  $\mathbf{e}(t) = [e_1(t), e_2(t)]^T$  are zero-mean wide-sense stationary (WSS) Gaussian random processes, thus,  $\mathbf{y}(t)$  is also WSS and Gaussian process since the system in (2.4) is linear and time invariant for zero initial state. These assumptions are used to asymptotically compute the CRB on the variance of the error of estimating the input signal incidence angle  $\phi_m$  when there is an unbiased estimator  $\hat{\phi}_m$  available [74], [75]. However, for simplicity, we make the following further assumptions:  $e_1(t)$  and  $e_2(t)$  are white, have the same variance  $\sigma_e^2$ , and are uncorrelated with each other as well as with  $p_m(t)$  ( $m = 1, 2, \dots, M$ ). These assumptions result in:

$$\mathbf{S}_y(\omega, \boldsymbol{\theta}) = \sum_{m=1}^M \mathbf{H}(e^{j\omega}, \Delta_m) S_{p_m}(\omega) \mathbf{H}^H(e^{j\omega}, \Delta_m) + \sigma_e^2 \mathbf{I}, \quad (2.6)$$

where

- (i)  $S_{p_m}(\omega)$ ,  $\sigma_e^2 \mathbf{I}$  and  $\mathbf{S}_y(\omega, \boldsymbol{\theta})$  are the power spectral densities of  $p_m(t)$ ,  $\mathbf{e}(t)$  and  $\mathbf{y}(t, \boldsymbol{\Delta})$ , respectively
- (ii)  $\boldsymbol{\theta} = [\Delta_1, \Delta_2, \dots, \Delta_M, S_{p_1}, \dots, S_{p_M}, \sigma_e^2]^T = [\theta_1, \dots, \theta_{2M+1}]$ , and

(iii)  $\mathbf{H}(e^{j\omega}, \Delta_m) = [H_1(e^{j\omega}, \Delta_m), H_2(e^{j\omega}, \Delta_m)]^T$  ( $m = 1, 2, \dots, M$ ) is the frequency response vector of the system related to the input signal  $p_m(t)$  with incidence angle  $\phi_m$ .

### 2.3.2 Cramér-Rao Bound

Let  $\mathbf{y}(t, \Delta)$  be defined as in (2.5) and satisfy the assumptions defined in Section 2.3.1. Then, the elements of the Fisher information matrix corresponding to unknown parameter vector  $\boldsymbol{\theta} = [\Delta_1, \Delta_2, \dots, \Delta_M, S_{p_1}, \dots, S_{p_M}, \sigma_e^2]^T$  can be found (for large  $N$ ) as follows [74], [75]:

$$\begin{aligned} [\mathbf{J}(\boldsymbol{\theta})]_{kl} &= \frac{N}{4\pi} \int_{-\pi}^{+\pi} \text{tr} \left\{ \frac{\partial \mathbf{S}_y(\omega, \boldsymbol{\theta})}{\partial \theta_k} \mathbf{S}_y^{-1}(\omega, \boldsymbol{\theta}) \frac{\partial \mathbf{S}_y(\omega, \boldsymbol{\theta})}{\partial \theta_l} \mathbf{S}_y^{-1}(\omega, \boldsymbol{\theta}) \right\} d\omega, \\ [\mathbf{J}(\boldsymbol{\theta})]_{kl} &\approx \frac{1}{2} \sum_{n=1}^N \text{tr} \left\{ \frac{\partial \mathbf{S}_y(n, \boldsymbol{\theta})}{\partial \theta_k} \mathbf{S}_y^{-1}(n, \boldsymbol{\theta}) \frac{\partial \mathbf{S}_y(n, \boldsymbol{\theta})}{\partial \theta_l} \mathbf{S}_y^{-1}(n, \boldsymbol{\theta}) \right\}, \end{aligned} \quad (2.7)$$

where  $\mathbf{S}_y(n, \boldsymbol{\theta})$  is the discrete fourier transform (DFT) of the system output with frequency index  $n$ , which is obtained by sampling  $\mathbf{S}_y(\omega, \boldsymbol{\theta})$  in the frequency domain [73].

Recall that  $\Delta_m = d \cos(\phi_m)/v$ . Hence, to find the CRB of estimating the direction of arrival,  $\phi_m$ , the transformation formula [75] is utilized:

$$\text{Var}(\hat{\phi}_m) \geq \left[ \left( \frac{\partial g(\boldsymbol{\theta})}{\partial \theta} \right) \mathbf{J}^{-1}(\boldsymbol{\theta}) \left( \frac{\partial g(\boldsymbol{\theta})}{\partial \theta} \right)^T \right]_{mm}, \quad (2.8)$$

where

- (i)  $\mathbf{g}(\boldsymbol{\theta}) = [g_1(\boldsymbol{\theta}), \dots, g_M(\boldsymbol{\theta})]$ , with  $m^{\text{th}}$  element defined as  $g_m(\boldsymbol{\theta}) = \arccos\left(\frac{v\Delta_m}{d}\right)$ ,  
and
- (ii)  $\mathbf{J}(\boldsymbol{\theta})$  is the Fisher information matrix with  $[\mathbf{J}(\boldsymbol{\theta})]_{kl}$  as defined in (2.7) ( $1 \leq k, l \leq 2M + 1$ ).

## 2.4 Numerical Results

We compare the CRBs of estimating the DOAs for the coupled and uncoupled systems to show the effect of the coupling. We use the following scenario for different signal-to-noise ratio (SNR) values.

We assume that in (2.5),  $p_1(t)$  with incidence angle  $\phi_1$  is the incoming signal that is to be localized, and similarly  $p_m(t)$  and  $\phi_m(t)$  ( $m = 2, 3, \dots, M$ ) are the signal from the environment and corresponding incidence angle, respectively. For simulation purposes only,  $\phi_m$  is randomly chosen ( $\phi_m$  is uniform in  $[-90^\circ, 90^\circ]$ ). Accordingly, SNR is defined as:

$$\text{SNR} = \frac{\text{Tr} \left\{ \sum_{n=1}^N \mathbf{H}(n, \Delta_1) S_{p_1}(n) \mathbf{H}^H(n, \Delta_1) \right\}}{\text{Tr} \left\{ \sum_{n=1}^N \left( \sum_{m=2}^M \mathbf{H}(n, \Delta_m) S_{p_m}(n) \mathbf{H}^H(n, \Delta_m) \right) + \sigma_e^2 \mathbf{I} \right\}}, \quad (2.9)$$

that is,  $p_m(t)$  for  $m = 2, 3, \dots, M$  contribute to the noise power. Note also that similar to (2.7),  $\mathbf{H}(n, \Delta_m) = [H_1(n, \Delta_m), H_2(n, \Delta_m)]$  and  $S_{p_m}(n)$  are the DFT of  $\mathbf{H}(e^{j\omega}, \Delta_m)$  and  $S_{p_m}(\omega)$  and  $n$  denotes the frequency index.

In addition to the assumptions in Section 2.3.1, for further simplification, we assume that the spectrum corresponding to  $p_m(t)$  is constant over the entire frequency range,

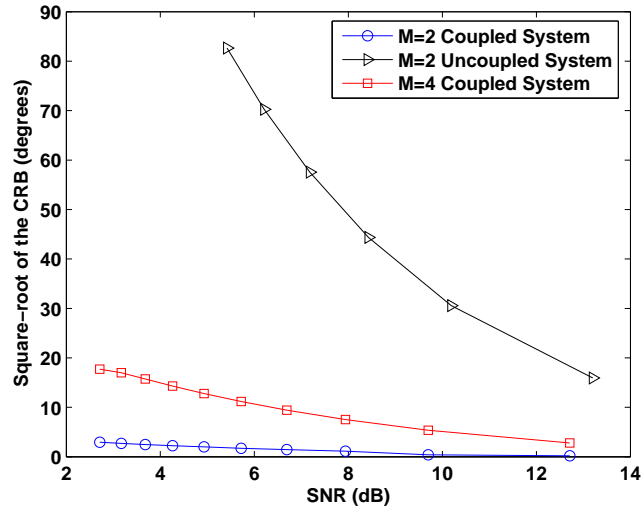


Figure 2.6: Square-root of the Cramér-Rao bound on direction of arrival estimation vs. SNR.

i.e.,  $S_{p_m}(w) = \sigma_{p_m}$  ( $\omega \in [-\pi, \pi]$ ). This simplification is reasonable in this problem, since the amplitude response of the mechanical model is already selective (see Fig. 2.3.)

- Model parameters [1] are chosen as below:

- $c_1 = c_2 = 1.15 * 10^{-5}$  Ns/m and  $k_1 = k_2 = 0.576$  N/m

- $c_3 = 3.88 * 10^{-5}$  Ns/m and  $k_3 = 5.18$  N/m, and

- $m = 2.88 * 10^{-10}$ kg.

- Note also that in these examples:

- $\phi_0 = 45^\circ$

- $t_0 = 0$  (see eqn.(2.4)), and

- $T_s = 0.02$  ms is the sampling period.

In Fig. 2.6, the improvement on the lower bound of the error in estimating DOA when there is coupling in the system is shown by plotting the square-root of the CRB with respect to SNR. This figure first illustrates the case where the number of the time samples is 2000 ( $N = 2000$ ), which correspond to a time range of 40ms, and the number of input signals is two ( $M = 2$ ), i.e., there is only one interference signal other than the input itself. Note that the number of the time samples are chosen to obtain CRB values of roughly one to two degrees for the coupled system to match the experimental results in [23]. When the CRBs of the coupled and the uncoupled system, for  $M = 2$ , are compared, a big difference is observed for the same SNR. This clear difference shows how the mechanical coupling improves the localization ability of the *O. ochracea*. For the coupled system, the error in azimuth angle drops down to 1-2 degrees, which is also in agreement with the experimental results demonstrated in [23]. Note that for the uncoupled system when  $M = 2$ , the variance of the error is markedly above the experimental results for SNR less than 12-14 dB.

Fig. 2.6 also demonstrates the performance of only the coupled system with  $N = 5000$  and  $M = 4$ . For the chosen values of  $M$  and  $N$ , the CRB values for the uncoupled system are too high, so the approximation (2.7) does not hold anymore.  $N = 5000$  for  $M = 4$  are chosen in the same way described for  $M = 2$  to reach the desired CRB values. It is observed that as the number of interference signals increases, so does the number of time samples for the same CRB values, when the plots of coupled system for  $M = 2$  and  $M = 4$  are compared. For the fly, this may correspond to requiring more time to locate the source when background noise increases. It can also be seen from the same figure that to achieve the same CRB values for  $M = 2$ , higher SNR values are needed for  $M = 4$ .

## 2.5 Summary

We analyzed the effect of coupling on the hearing system of the *O. ochracea*. By examining the impulse and frequency responses of the model, we showed that the coupling increases the time and amplitude differences between the two ears. Using our statistical model, we asymptotically computed the CRB of the DOA estimation error for unknown input signal and noise spectra. Comparing the CRB of the coupled with the uncoupled system, we illustrated the enhancement provided by the mechanical coupling. We have proven the experimental results regarding the azimuthal localization capacity of the *O. ochracea*.



# Chapter 3

## Biologically Inspired Coupled Antenna System<sup>2 3</sup>

We propose to design a small-size antenna array having high direction of arrival (DOA) estimation accuracy and radiation performance, inspired by a female *Ormia ochracea*'s coupled ears. The female *Ormia* is able to locate male crickets' call accurately, for reproduction purposes, despite the small distance between its ears compared with the incoming wavelength. This phenomenon has been explained by the mechanical coupling between the *Ormia*'s ears, modeled by a pair of differential equations. In this chapter, we first solve the differential equations governing the *Ormia ochracea*'s ear response, and convert the response to the pre-specified radio frequencies. We consider passive and active transmitting antenna arrays. First, to obtain a passive antenna array with biologically inspired coupling (BIC), using the converted response, we implement the BIC as a multi-input multi-output filter on a uniform linear antenna array output. We derive the maximum likelihood estimates (MLEs) of

---

<sup>2</sup>Based on M. Akcakaya C.H Muravchik and A. Nehorai, "Biologically Inspired Coupled Antenna Array for Direction of Arrival Estimation" in *Proc. 44th Asilomar Conf. Signals, Syst. Compt.*, Pacific Grove, CA, USA, Nov. 7-10 2010. ©[2010] IEEE

<sup>3</sup>Based on M. Akcakaya and A. Nehorai, "Biologically Inspired Coupled Antenna Beam pattern Design" *Bioinspiration and Biomimetics*, vol.5, no.4, p.046003, 2010. ©[2010] IOP.

source DOAs, and compute the corresponding Cramér-Rao bound (CRB) on the DOA estimation error as a performance measure. We also consider circular array configuration and compute the mean-square angular error bound on the three-dimensional localization accuracy. Then, to obtain an active antenna array with BIC, together with the undesired electromagnetic coupling among the array elements (due to their proximity), we apply the BIC in the antenna array factor. We assume finite-length dipoles as the antenna elements and compute the radiation intensity, and accordingly the directivity gain, half-power beamwidth (HPBW) and side lobe level (SLL) as radiation performance measures for this antenna system with BIC. For both the passive and active antenna arrays, we propose an algorithm to optimally choose the BIC for maximum localization and radiation performance. With numerical examples, we demonstrate the improvement due to the BIC.

### 3.1 Introduction

Accurate source localization has attracted significant attention in many civil and military applications over the past few decades [76]-[81]. These applications require array of sensors (antennas) with high resolution and direction of arrival (DOA) estimation accuracy, and radiation performance. Most existing array design methods rely on the inter-element time delay of the antenna array for DOA estimation [82], [83], and radiation pattern design [84]. The performance of the array is directly proportional to the size of the array's electrical aperture, such that large-aperture arrays are required to achieve better DOA estimation and radiation performance. However, using a large aperture array to improve performance can be costly and also may not be feasible,

since in many tactical and mobile applications the sensing systems are confined to small spaces, requiring small-sized arrays.

In this chapter, we propose biologically inspired antenna array to have high DOA estimation accuracy and radiation performance with small-sized compact arrays. The approach is inspired by a parasitoid fly called *Ormia ochracea*, which has a remarkable localization ability despite its small size (see Chapters 1 and 2 for further discussions). To perpetuate its species, a female *Ormia ochracea* must find a male field cricket using the cricket's mating call.

Next we demonstrate our results on the statistical analysis of DOA estimation and beam pattern design for biologically inspired coupled antenna array.

## **3.2 Biologically Inspired Coupled Antenna Array for Direction of Arrival Estimation**

In this section, we develop a biologically inspired small-sized coupled antenna array, having high DOA estimation performance, inspired by the *Ormia*. First, we solve the second order differential equations governing the *Ormia*'s coupled ear response, and then convert this response to fit the desired radio frequencies. Using the converted response, we implement the biologically inspired coupling (BIC) as a multi-input multi-output filter and obtain the desired array response. By standard antenna array we shall refer to a system without the BIC. Note here that to simplify the analysis, we assume that we know the carrier frequency and the bandwidth of the incoming signal.

For two antennas, our approach of pre-filtering the measurements is similar to the generalized cross-correlation (GCC) method proposed in [85]. The GCC method generalizes the widely used time delay estimation pre-filtering methods (and hence DOA estimation) such as the Roth processor [86], smoothed coherence transform (SCOT) [87], phase transform (PHAT) [88], Eckart processor [89], and Hannah Thomson (HT) processor [90]. In Section 3.2.5 we compare our approach with the GCC method, specifically with the HT processor. We choose the HT processor because it is identical to the maximum likelihood (ML) estimator of DOA's using a standard array [90]. Moreover it was shown in [85] that under low signal-to-noise ratio (SNR) conditions other pre-filtering methods are equivalent to the HT processor. The HT processor achieves the CRB, and performance of a GCC processor can be analyzed using the CRB [85] (see also [91], [92]). We demonstrate that, compared with a standard antenna array, an antenna array with BIC has higher localization accuracy.

Similarly for multiple antennas, to demonstrate the improvement in the localization performance due to the BIC, we compare our method with the multi-channel cross-correlation technique [93]. Under our assumptions, the multi-channel cross-correlation technique asymptotically reduces to ML estimator of the DOA's using a standard array. Therefore, for comparison purposes, we demonstrate the performances of the ML estimators of the standard antenna array (standard array) and the antenna array which uses the BIC (BIC array).

### 3.2.1 Antenna Array Model

In this section, we introduce the measurement and statistical models for the biologically inspired antenna array.

## Measurement Model

We develop a coupled multiple-antenna array at radio frequencies inspired by the Ormia's ears. We start with the measurement model of a standard antenna array [82]. We assume narrow-band incoming signal and write the complex envelope of the measurements as

$$\mathbf{x}(t) = \mathbf{A}(\boldsymbol{\phi})\mathbf{s}(t) + \mathbf{e}_e(t), \quad t = 1, \dots, N \quad (3.1)$$

where

- $\mathbf{x}(t)$  is  $M \times 1$  output vector of the array, with  $M$  antennas
- $\mathbf{s}(t) = [s_1(t), \dots, s_Q(t)]^T$  is the  $Q \times 1$  input signal vector with  $Q$  as the number of the sources
- $\mathbf{A}(\boldsymbol{\phi}) = [\mathbf{a}(\phi_1) \cdots \mathbf{a}(\phi_Q)]$  is the array response, with  $\phi_q$  as the DOA of the  $q^{th}$  source
- $\mathbf{a}(\phi_q) = [1, \exp(-j\omega\Delta_q), \dots, \exp(-j\omega(M-1)\Delta_q)]$  for a uniform linear array (later in Section 3.2.4, we extend our analysis also to a uniform circular array)
- $\Delta_q = \frac{d \cos \phi_q}{v}$  with  $d$  as the distance between each antenna (we focus on 2-D direction finding)
- $v$  is the speed of signal propagation in the medium, and
- $\mathbf{e}_e(t)$  is the additive environment noise.

Next, we implement the BIC as a filtering procedure and obtain the biologically inspired array response. We first obtain the frequency response of the Ormia's ears,

and modify it to fit the desired radio frequencies. We then employ the converted response as a two-input two-output filter and obtain a two-antenna array with the BIC. We also generalize the BIC concept to multiple-antenna arrays.

Note that in practice, systems with closely spaced antennas typically undergo undesired electromagnetic coupling among the antennas. In our work, to simplify the analysis we assume that the calibration is achieved beforehand and hence we ignore the effect of the undesired coupling. Assuming known calibration, the performance of the system should not be affected, therefore we do not include it in our analysis. We will consider the effect of the combined coupling (BIC and unknown undesired) in our future work.

### Response of the Ormia's Coupled Ears

To obtain the response of the Ormia's coupled ears, we solve the second-order differential equations governing the mechanical model proposed in [1] for the Ormia's ears (Fig. 2.1), and find the corresponding transfer function. Note that these equations represent a two-input two-output filter system. We rewrite the governing differential equations:

$$\begin{bmatrix} k_1 + k_3 & k_3 \\ k_3 & k_2 + k_3 \end{bmatrix} \begin{bmatrix} y_1 \\ y_2 \end{bmatrix} + \begin{bmatrix} c_1 + c_3 & c_3 \\ c_3 & c_2 + c_3 \end{bmatrix} \begin{bmatrix} \dot{y}_1 \\ \dot{y}_2 \end{bmatrix} + \begin{bmatrix} m_0 \\ m_0 \end{bmatrix} \begin{bmatrix} \ddot{y}_1 \\ \ddot{y}_2 \end{bmatrix} = \begin{bmatrix} x_1(t, \Delta) \\ x_2(t, \Delta) \end{bmatrix} = F(t, \Delta), \quad (3.2)$$

where

- $x_i(t, \Delta)$ ,  $i = 1, 2$ , are the input signals
- $y_i(t)$ ,  $i = 1, 2$ , are the displacements of each ear, and
- $m_0$ ,  $k$ 's, and  $c$ 's are the effective mass, spring and dash-pot constants, respectively.

To solve the differential equations and obtain the transfer function (and hence the frequency response) of the system, we apply the Laplace transform to (3.2) assuming zero initial values (See our approach in Chapter 2 for the state-space solution of the Ormia's ear responses. Here, we focus on the Laplace transform solution which simplifies the solution.)

$$\begin{bmatrix} Y_1(s) \\ Y_2(s) \end{bmatrix} = 1/P(s) \begin{bmatrix} D_2(s) & -N(s) \\ -N(s) & D_1(s) \end{bmatrix} \begin{bmatrix} X_1(s) \\ X_2(s) \end{bmatrix}, \quad (3.3)$$

where

- $Y_1(s)$  and  $Y_2(s)$  are the Laplace transforms of  $y_1(t)$  and  $y_2(t)$
- $X_1(s)$  and  $X_2(s)$  are the Laplace transforms of  $x_1(t)$  and  $x_2(t)$
- $D_1(s) = m_0s^2 + (c_1 + c_3)s + k_1 + k_3$  and  $D_2(s) = m_0s^2 + (c_2 + c_3)s + k_2 + k_3$
- $N(s) = c_3s + k_3$  (coupling effect), and
- $P(s) = D_1(s)D_2(s) - N^2(s)$  is the characteristic function.

We obtain the Laplace transform of the impulse responses associated with (3.2) by substituting

$$x_1(t) = \delta(t) \rightarrow X_1(s) = 1,$$

$$x_2(t) = x_1(t - \Delta) \rightarrow X_2(s) = e^{-s\Delta}.$$

Then the responses of the two ears are

$$\begin{aligned} H_1(s, \Delta) &= [D_2(s) - N(s)e^{-s\Delta}]/P(s), \\ H_2(s, \Delta) &= [D_1(s)e^{-s\Delta} - N(s)]/P(s). \end{aligned} \quad (3.4)$$

For  $s = j\omega$ , we obtain the frequency responses of the Ormia's coupled ears. See Figs. 3.1 and 3.2 for the amplitude and phase responses of the Ormia's ears. These figures have already been shown in Chapter 2. The approach we use here is different (time -vs- frequency domain), but the results coincide with Figs. 2.3 and 2.4 as it should be. To demonstrate the effect of the mechanical coupling, we compare the coupled response of the Ormia's ear with a response assuming zero coupling,  $N(s) = 0$ , i.e.,  $c_3 = 0 = k_3$ . We observe that the coupling amplifies the amplitude and phase differences between the responses of the Ormia's two ears. The figures are presented for  $45^\circ$  DOA using the effective mass, spring and dash-pot constants experimentally obtained in [1]. Moreover in [1], it was shown analytically and experimentally that similar responses hold for a wide range of DOAs.

### **Converting to Desired Radio Frequencies for Array Response Design**

We now modify the frequency response of the Ormia's ears to fit the desired radio frequencies. We achieve this conversion by re-computing the poles of the transfer function in (3.3), the roots of  $P(s) = D_1(s)D_2(s) - N^2(s) = 0$ , for frequencies of interest. We shift the resonance frequencies of the system,  $f_1$  and  $f_2$ , by changing the



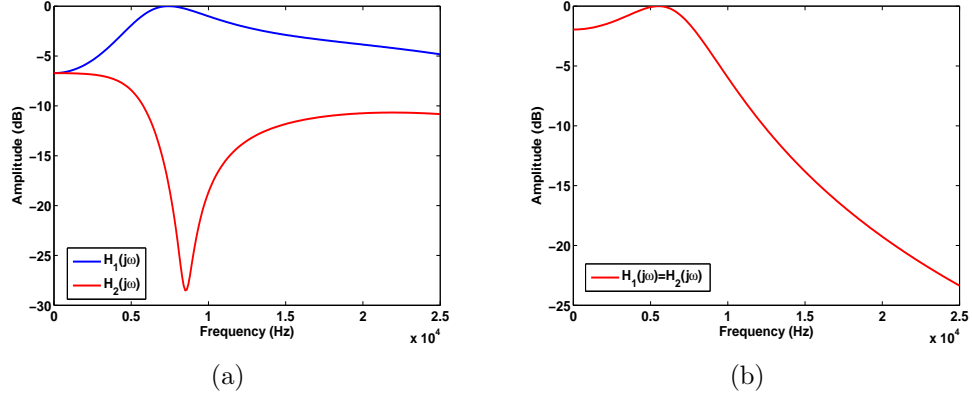


Figure 3.1: Amplitude responses of the *Ormia ochracea*'s two ears. (a) Coupled system. (b) Uncoupled system.

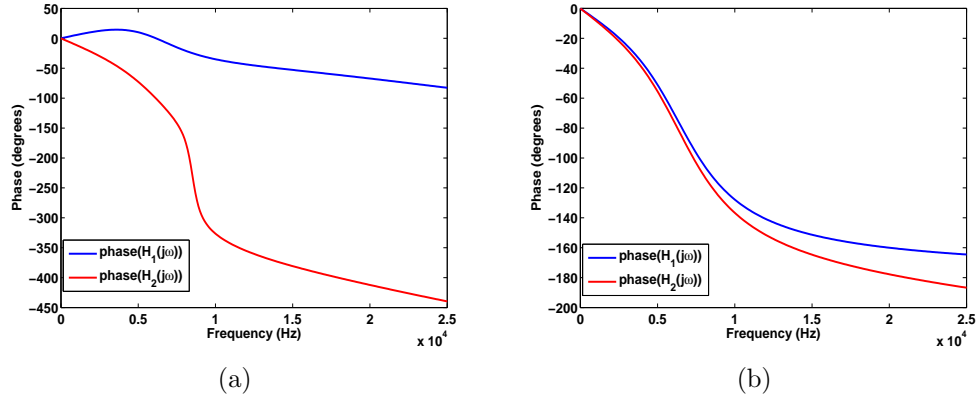


Figure 3.2: Phase responses of the *Ormia ochracea*'s two ears. (a) Coupled system. (b) Uncoupled system.

imaginary parts of the poles. This corresponds to changing the system parameters, namely mass, spring and dash-pot constants defined in the analogous mechanical model [see (2)]. We will keep the real parts,  $r_1$  and  $r_2$ , as free variables which will enable us to optimize the coupling without modifying the resonant frequencies, see Section 3.2.3 for the details of the optimization procedure and computation of the real and imaginary parts of the poles. Our purpose is to preserve a coupling structure similar to Figs. 3.1 and 3.2 which amplifies the differences between the amplitude and

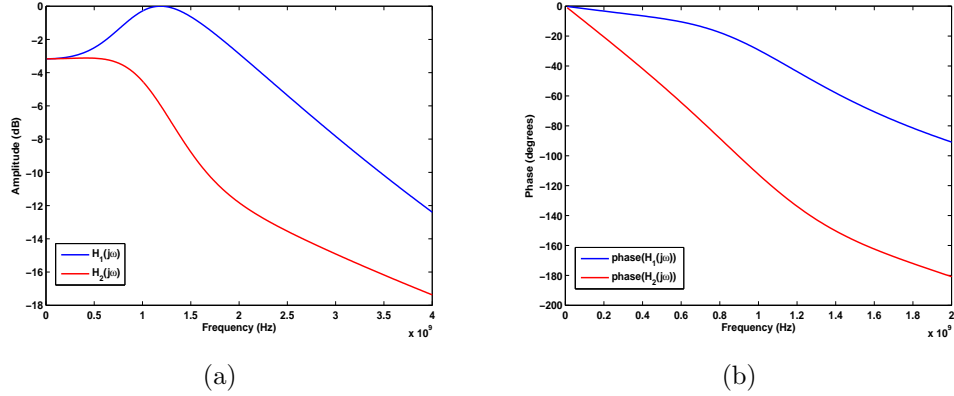


Figure 3.3: (a) Amplitude and (b) phase responses of the converted system.

phase responses of the system outputs. For a narrowband signal with bandwidth  $B$  and carrier frequency  $f_c$ , we choose  $f_1 = f_c - B/2$  and  $f_2 = f_c + B/2$ . See for example Fig. 3.3 for the amplitude and phase responses of the converted system with  $f_1 = 0.99$  GHz and  $f_2 = 1.01$  GHz as the desired resonant frequencies considering a bandlimited signal  $B = 20$  MHz and  $f_c = 1$  GHz. Note that for this signal, we can easily show that the propagation time of the signal across the array (for instance, consider as in the section of Numerical Results an array with 5 elements and  $d = 0.1\lambda$  inter-element spacing) is much smaller than the reciprocal of the signal bandwidth. The latter is a standard narrowband criterion assumed in array signal processing (narrowband array assumption)[94]. This figure is obtained for  $45^\circ$  DOA. Similar structure holds for different DOAs. In Section 3.2.5, we demonstrate the performance of the converted system for different DOAs.

### Biologically Inspired Array Processing

We first consider two-antenna array for BIC implementation. For an antenna array with two identical antennas,  $D_1(j\omega) = D_2(j\omega) = D(j\omega)$ , we apply the BIC filter to

the measurements in (3.1) and obtain in the frequency domain

$$\begin{bmatrix} Y_1(j\omega) \\ Y_2(j\omega) \end{bmatrix} = \mathbf{H}_I(j\omega) \begin{bmatrix} X_1(j\omega) \\ X_2(j\omega) \end{bmatrix}, \quad (3.5)$$

$$\text{where } \mathbf{H}_I(j\omega) = \begin{bmatrix} D(j\omega) & N(j\omega) \\ N(j\omega) & D(j\omega) \end{bmatrix}^{-1}.$$

We assume that an incoming bandlimited signal, fitting the standard narrowband assumption as mentioned in Section 3.2.1, with the carrier frequency  $\omega = \omega_c = 2\pi f_c$ , can be approximated as a summation of components which are almost pure in frequency such that  $\mathbf{s}(t) = \sum_{f=1}^F \mathbf{s}^f(t)$ , where  $F$  is the number of such components. Then we obtain the measurement model in the time domain for biologically inspired antenna array using the fact that for each component multiplication in the frequency domain results in convolution in the time domain. Moreover, convolution of the BIC filter with each component results in multiplication of the time domain incoming signal with the BIC filter computed at the corresponding frequencies of the components [73]-[96]. Then under the above mentioned assumption, we approximate the output of the BIC filter (3.5) to the  $f^{\text{th}}$  component as

$$\mathbf{y}^f(t) = \begin{bmatrix} y_1(t) \\ y_2(t) \end{bmatrix}^f = \mathbf{H}_I(j\omega_f) \mathbf{A}^f(\phi) \mathbf{s}^f(t) + \tilde{\mathbf{e}}^f(t) \quad t = 1, \dots, N, \quad (3.6)$$

where  $\tilde{\mathbf{e}}^f(t) = \mathbf{e}_a^f(t) + \mathbf{H}_I(j\omega_f) \mathbf{e}_e^f(t)$ , such that only the environment noise is affected by the BIC. Here  $\mathbf{e}_a^f$  and  $\mathbf{e}_e^f$  are the amplifier and environment noise components corresponding to  $\mathbf{s}^f(t)$ , respectively. The implicit assumption here is that the array will be designed with coupling between the antennas and/or by filtering to achieve

a response matrix,  $\mathbf{H}_I(j\omega_f)\mathbf{A}^f(\phi)$ . Recall that in computing  $\mathbf{H}_I(j\omega)$ , we use the method explained in Section 3.2.1 for the selection of the resonant frequencies (assuming the starting and ending frequencies of the bandlimited signal are equal to the first,  $f_1$ , and second,  $f_2$ , resonant frequencies, respectively). See also Section 3.2.3 for the selection of the real parts of the roots of the characteristic function defined after (3.3). We then collect the measurements corresponding to different components in a vector as

$$\mathbf{y}(t) = \begin{bmatrix} \mathbf{y}^1(t) \\ \dots \\ \mathbf{y}^F(t) \end{bmatrix} = \mathbf{H}_I\mathbf{A}(\phi)\bar{\mathbf{s}}(t) + \tilde{\mathbf{e}}(t), \quad (3.7)$$

where

- $\mathbf{H}_I = \text{blkdiag}(\mathbf{H}_I(j\omega_1), \dots, \mathbf{H}_I(j\omega_F))$  is  $2F \times 2F$  block diagonal matrix with  $\mathbf{H}_I(j\omega_f)$  as the  $f^{\text{th}}$  block diagonal entry
- $\mathbf{A}(\phi) = \text{blkdiag}(\mathbf{A}^1(\phi), \dots, \mathbf{A}^F(\phi))$
- $\bar{\mathbf{s}}(t) = [(\mathbf{s}^1(t))^T, \dots, (\mathbf{s}^F(t))^T]^T$ , and
- $\tilde{\mathbf{e}}(t) = [(\tilde{\mathbf{e}}^1(t))^T, \dots, (\tilde{\mathbf{e}}^F(t))^T]^T$ .

Under this approximation of the filter output, the measurements depend on the values of the filter at  $F$  different frequencies (not just at the carrier frequency), and hence the proposed procedure employs the dynamic properties of the filter.

We next extend the model in (3.6) to  $M$  identical antennas. We assume each antenna is coupled to its immediate neighboring antennas in the array, i.e., each antenna (except for the first and the last antennas) is coupled to two antennas. We will consider in our future work other possible coupling configurations, more than coupling only

the adjacent antennas. Note that other antenna array structures may also be possible, however we focus on the linear and circular arrays which are the most commonly used structures in antenna array processing, see also Section 3.2.4. Different array structures will also be investigated in our future work. Therefore we generalize the two-input two-output filter by using it in a tridiagonal  $M \times M$  matrix form:

$$\mathbf{y}^f(t) = \begin{bmatrix} y_1(t) \\ \dots \\ y_M(t) \end{bmatrix}^f = \mathbf{H}_I(j\omega_f) \begin{bmatrix} x_1(t) \\ \dots \\ x_M(t) \end{bmatrix} = \mathbf{H}_I(j\omega_f) \mathbf{A}^f(\boldsymbol{\phi}) \mathbf{s}^f(t) + \tilde{\mathbf{e}}^f(t) \quad (3.8)$$

$$\text{where } \mathbf{H}_I(j\omega_f)^{-1} = \begin{bmatrix} D(j\omega_f) & N(j\omega_f) & 0 & \dots & & & 0 \\ N(j\omega_f) & D(j\omega_f) & N(j\omega_f) & 0 & \dots & & 0 \\ 0 & N(j\omega_f) & D(j\omega_f) & N(j\omega_f) & 0 & \dots & 0 \\ & & & \dots & & & \\ 0 & \dots & & & & N(j\omega_f) & D(j\omega_f) \end{bmatrix}.$$

Then we stack the measurements obtained from different components as in (3.7) and obtain a measurement model for  $M$ -antenna system.

### Filter Interpretation

In this section, we explain the physical effects of the biologically inspired coupling on the linear antenna array.

- The mechanical coupling is represented as a two-input two-output filter (Fig. 3.4), amplifying the differences between the outputs of the system, see Figures 3.1 and 3.2.

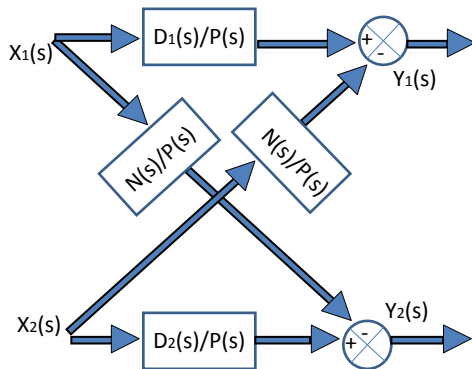


Figure 3.4: Two-input two-output filter representation of the Ormia's coupled ears' response.

- Since the mechanical coupling amplifies the amplitude and phase differences between the frequency responses of the Ormia's ears [26], it effectively creates larger distance between successive antennas, a virtual array with a larger aperture.
- Applying the BIC to the antenna array, we generate a virtual array with a larger aperture. Larger aperture improves the DOA estimation performance (providing higher estimation accuracy).

### Statistical Assumptions

We introduce our statistical assumptions on the measurement model. We assume, in (3.1),

- $\phi = [\phi_1, \dots, \phi_Q]^T$  is the  $Q \times 1$  vector of deterministic unknown DOA parameters;

- $\bar{\mathbf{s}}(t)$  is a Gaussian input signal vector,  $E[\bar{\mathbf{s}}(t)] = \mathbf{0}$ ,  $E[\bar{\mathbf{s}}(t)\bar{\mathbf{s}}(t')^H] = \mathbf{P}\delta_{tt'}$  and  $E[\bar{\mathbf{s}}(t)\bar{\mathbf{s}}(t')^T] = \mathbf{0}$ , with  $\mathbf{P}$  as the  $QF \times QF$  unknown source covariance matrix, and for  $t, t' = 1, \dots, N$   $\delta_{tt'} = 1$  when  $t = t'$  and zero otherwise
- $\tilde{\mathbf{e}}(t)$  is Gaussian distributed and  $E[\tilde{\mathbf{e}}(t)] = \mathbf{0}$ ,  $E[\tilde{\mathbf{e}}(t)\tilde{\mathbf{e}}(t')^H] = (\sigma_a^2\mathbf{I} + \sigma_e^2\mathbf{H}_I\mathbf{H}_I^H)\delta_{tt'}$  and  $E[\tilde{\mathbf{e}}(t)\tilde{\mathbf{e}}(t')^T] = \mathbf{0}$ , such that  $\sigma_a^2$  and  $\sigma_e^2$  are the unknown variances of amplifier and environment noise, respectively, and
- $\bar{\mathbf{s}}(t)$  and  $\tilde{\mathbf{e}}(t')$  are uncorrelated for all  $t$  and  $t'$ .

### 3.2.2 Maximum Likelihood Estimation and Performance Analysis

In this section, we demonstrate the derivation of the DOA estimation, and the Cramér-Rao bound computation for statistical performance analysis of the array's localization accuracy.

#### Maximum Likelihood Estimation

The maximum likelihood estimate of the DOA is defined as the value that maximizes the likelihood function (see (3.11)). It is asymptotically optimal, namely it is unbiased and it attains the CRB of minimum variance [75]. Following the statistical assumptions in Section 3.2.1, we write the probability density function of the measurements as

$$\prod_{t=1}^N p[\mathbf{y}(t); \phi, \mathbf{P}, \sigma_a^2, \sigma_e^2] = \prod_{t=1}^N \frac{1}{|\pi\mathbf{R}|} \exp[\mathbf{y}(t)\mathbf{R}^{-1}\mathbf{y}(t)], \quad (3.9)$$

where

- $\mathbf{R} = \text{E}[\mathbf{y}(t)\mathbf{y}(t)^H] = \tilde{\mathbf{A}}(\boldsymbol{\phi})\mathbf{P}\tilde{\mathbf{A}}(\boldsymbol{\phi})^H + \sigma_e^2\boldsymbol{\Sigma}(\rho)$ , with  $\boldsymbol{\Sigma}(\rho) = \rho\mathbf{I} + \mathbf{H}_I\mathbf{H}_I^H$ , and  $\rho = \sigma_a^2/\sigma_e^2$
- $\tilde{\mathbf{A}}(\boldsymbol{\phi}) = \mathbf{H}_I\mathbf{A}(\boldsymbol{\phi})$ .

We obtain  $\boldsymbol{\Sigma}(\rho)^{-1/2}$ , then we define  $\bar{\mathbf{y}} = \boldsymbol{\Sigma}(\rho)^{-1/2}\mathbf{y}$ , and  $\bar{\mathbf{A}}(\boldsymbol{\theta}) = \boldsymbol{\Sigma}(\rho)^{-1/2}\tilde{\mathbf{A}}(\boldsymbol{\phi})$ , where  $\boldsymbol{\theta} = [\rho, \boldsymbol{\phi}]^T$  is  $(Q + 1) \times 1$  vector of unknown parameters. Next, we rewrite (3.9)

$$\prod_{t=1}^N p[\bar{\mathbf{y}}(t); \boldsymbol{\phi}, \rho, \mathbf{P}, \sigma_e^2] = \prod_{t=1}^N \frac{1}{|\pi\tilde{\mathbf{R}}|} \exp\left[-\bar{\mathbf{y}}(t)\tilde{\mathbf{R}}^{-1}\bar{\mathbf{y}}(t)\right], \quad (3.10)$$

where  $\tilde{\mathbf{R}} = \text{E}[\bar{\mathbf{y}}(t)\bar{\mathbf{y}}(t)^H] = \bar{\mathbf{A}}(\boldsymbol{\theta})\mathbf{P}\bar{\mathbf{A}}(\boldsymbol{\theta})^H + \sigma_e^2\mathbf{I}$ .

Then taking the logarithm of (3.10) and considering it as a function of the unknown parameters, we obtain the log-likelihood function as

$$\text{LF}(\boldsymbol{\theta}, \mathbf{P}, \sigma_e^2) = -N \left[ M\ln(\pi) + \ln|\tilde{\mathbf{R}}| + \text{tr}(\tilde{\mathbf{R}}^{-1}\hat{\mathbf{R}}) \right], \quad (3.11)$$

where  $\hat{\mathbf{R}} = \frac{1}{N} \sum_{t=1}^N \bar{\mathbf{y}}(t)\bar{\mathbf{y}}(t)^H$ , is the sample covariance.

We follow the procedure explained in [97], such that we derive the MLEs of  $\mathbf{P}$  and  $\sigma_e^2$  as a function of  $\boldsymbol{\theta}$ :

- $\hat{\mathbf{P}}(\boldsymbol{\theta}) = \bar{\mathbf{A}}(\boldsymbol{\theta})^\dagger \hat{\mathbf{R}} (\bar{\mathbf{A}}(\boldsymbol{\theta})^\dagger)^H - \hat{\sigma}_e^2(\boldsymbol{\theta})(\bar{\mathbf{A}}(\boldsymbol{\theta})^H \bar{\mathbf{A}}(\boldsymbol{\theta}))^{-1}$
- $\hat{\sigma}_e^2(\boldsymbol{\theta}) = \text{tr}(\Pi^\perp \hat{\mathbf{R}})/(M - Q)$



- $\bar{\mathbf{A}}(\boldsymbol{\theta})^\dagger = [\bar{\mathbf{A}}(\boldsymbol{\theta})^H \bar{\mathbf{A}}(\boldsymbol{\theta})]^{-1} \bar{\mathbf{A}}(\boldsymbol{\theta})^H$
- $\boldsymbol{\Pi} = \bar{\mathbf{A}}(\boldsymbol{\theta}) \bar{\mathbf{A}}(\boldsymbol{\theta})^\dagger$ , and
- $\boldsymbol{\Pi}^\perp = \mathbf{I} - \boldsymbol{\Pi}$ .

Concentrating the likelihood function using these estimates,  $F(\boldsymbol{\theta}) = L[\boldsymbol{\theta}, \hat{\mathbf{P}}(\boldsymbol{\theta}), \hat{\sigma}_e^2(\boldsymbol{\theta})]$ , we obtain the MLE of  $\boldsymbol{\theta}$  through

$$\hat{\boldsymbol{\theta}} = \operatorname{argmin}_{\boldsymbol{\theta}} F(\boldsymbol{\theta}) = \operatorname{argmin}_{\boldsymbol{\theta}} \ln \left| \bar{\mathbf{A}}(\boldsymbol{\theta}) \hat{\mathbf{P}}(\boldsymbol{\theta}) \bar{\mathbf{A}}(\boldsymbol{\theta})^H + \hat{\sigma}_e^2(\boldsymbol{\theta}) \mathbf{I} \right|. \quad (3.12)$$

### Cramér-Rao Bound

We analyze the array's statistical performance, i.e., accuracy in estimating the source direction, by computing the Cramér-Rao bound. The CRB is the lower bound on estimation error for any unbiased estimator. We concentrate the likelihood function in (3.11) with respect to  $\mathbf{P}$  and  $\sigma_e^2$  and compute the CRB on the covariance matrix of any unbiased estimator of  $\boldsymbol{\theta}$ . Using the results in [98] and [99], we define

$$\mathbf{CRB}^{-1}(\boldsymbol{\theta}) = N \cdot \mathbf{F}_0''(\boldsymbol{\theta}), \quad (3.13)$$

where

$$\mathbf{F}_0''(\boldsymbol{\theta}) = \lim_{N \rightarrow \infty} \frac{\partial^2}{\partial \boldsymbol{\theta} \partial \boldsymbol{\theta}^T} F(\boldsymbol{\theta}), \quad (3.14)$$

with  $F(\boldsymbol{\theta})$  as defined in (3.12).

Then we apply the Lemma C.1 and C.2 of [99], and obtain

$$[\mathbf{CRB}^{-1}(\boldsymbol{\theta})]_{ij} = \frac{2N}{\sigma_e^2} \operatorname{Re} \left\{ \operatorname{tr} [\mathbf{U} \mathbf{D}_j^H \boldsymbol{\Pi}^\perp \mathbf{D}_i] \right\}, \quad (3.15)$$

where

- $i, j = 1, \dots, Q + 1$ , and
- $\mathbf{U} = \mathbf{P} \left[ \bar{\mathbf{A}}^H(\boldsymbol{\theta}) \bar{\mathbf{A}}(\boldsymbol{\theta}) \mathbf{P} + \sigma^2 \mathbf{I} \right]^{-1} \bar{\mathbf{A}}^H(\boldsymbol{\theta}) \bar{\mathbf{A}}(\boldsymbol{\theta}) \mathbf{P}$ ,
- $\mathbf{D}_i = \frac{\partial \bar{\mathbf{A}}(\boldsymbol{\theta})}{\partial \theta_i}$ .

Then collecting the terms we have

$$\text{CRB}(\boldsymbol{\theta}) = \frac{\sigma_e^2}{2N} \left\{ \text{Re} \left( \text{btr} \left[ (\mathbf{1} \otimes \mathbf{U}) \boxtimes (\mathbf{D}^H \boldsymbol{\Pi}^\perp \mathbf{D})^{bT} \right] \right) \right\}^{-1}, \quad (3.16)$$

where,

- $\mathbf{1}$  is a  $Q + 1 \times Q + 1$  matrix of ones
- $\mathbf{D} = [\mathbf{D}_1 \ \cdots \ \mathbf{D}_{Q+1}]$
- btr is block trace operator
- $\otimes$  Kronecker product
- $\boxtimes$  is block Schur-Hadamard product, and
- $bT$  is block transpose operator.

See Appendix A for the definition of the block matrix operators. Note that we modified the results in [99] to account for our assumptions and filtering effect.

### 3.2.3 Optimization of the Biologically Inspired Coupling

In this section, we develop a method to maximize the localization performance of the antenna array by optimizing the BIC. We first introduce the optimization parameters, and then formulate a cost function employing the CRB on DOA estimation for optimum performance. Note here that we optimize the value of the BIC for the antenna array structures (linear and circular) and coupling configurations (coupling with adjacent antennas) as discussed in Section 3.2.1. Other array structures and different coupling configurations are left as a future work.

Recall from Section 3.2.1 that we change the imaginary parts of the poles of the characteristic function to shift the resonance frequencies of the system response while we keep the real parts as free variables. Therefore, under the constraints that we explain below, we have the freedom of choosing the real parts for optimum coupling design. We compute the poles of the system as a function of system parameters (‘ $k$ ’, ‘ $c$ ’ and ‘ $m_0$ ’). Recalling the discussions after (3.3), we assume identical antennas ( $D_1 = D_2 = D$ , and hence  $k_1 = k_2 = k$ ,  $c_1 = c_2 = c$ ), and write the characteristic function as

$$\begin{aligned} P(s) &= D(s)^2 - N(s)^2 \\ &= m_0^2[(s^2 + b_1s + a_1)^2 - (b_2s + a_2)^2], \end{aligned} \quad (3.17)$$

where  $a_1 = (k + k_3)/m_0$ ,  $a_2 = k_3/m_0$ ,  $b_1 = (c + c_3)/m_0$ , and  $b_2 = c_3/m_0$ . We assume that the parameters  $a_1$ ,  $a_2$ ,  $b_1$ , and  $b_2$  are positive. Then we obtain the roots (the

poles of the system) as

$$p_{1,2} = -r_1 \pm \sqrt{i_1} \quad (3.18)$$

$$p_{3,4} = -r_2 \pm \sqrt{i_2}, \quad (3.19)$$

where  $r_1 = \frac{1}{2}(b_1 + b_2)$ ,  $r_2 = \frac{1}{2}(b_1 - b_2)$ ,  $i_1 = \frac{1}{4}[(b_1 + b_2)^2 - 4(a_1 + a_2)]$ , and  $i_2 = \frac{1}{4}[(b_1 - b_2)^2 - 4(a_1 - a_2)]$ . In order to change the resonance frequencies, we change the values of the imaginary parts such that  $i_1 = -(2\pi f_1)^2$  and  $i_2 = -(2\pi f_2)^2$ , where  $f_1$  and  $f_2$  are the new resonant frequencies. We set  $r_1$  and  $r_2$  as the free parameters. We have the freedom to control the real parts as long as  $r_1 > r_2$  due to the positivity assumption on the parameters  $a_1$ ,  $a_2$ ,  $b_1$ , and  $b_2$ . Define  $\mathbf{r} = [r_1, r_2]^T$ , then  $\text{CRB}(\boldsymbol{\theta}, \mathbf{r})$ , i.e., the CRB is also a function of the real parts of the characteristic function. Minimizing the CRB w.r.t. the real parts also preserves the dynamic properties of the filter.

Next we formulate the optimization problem to improve the localization performance. We choose the CRB on DOA estimation as the utility function to be minimized. This is a reasonable choice since minimizing the CRB minimizes the lower bound on the error of the MLE of DOA. Therefore we formulate the problem as

$$\underset{\mathbf{r}}{\text{argmin}} \text{tr} [\text{CRB}(\boldsymbol{\theta}, \mathbf{r})] \quad \text{s.t.} \quad r_1 - r_2 > 0, \quad (3.20)$$

where by taking the trace of the  $\text{CRB}(\boldsymbol{\theta}, \mathbf{r})$ , we minimize the sum of the variance of the errors on the DOA,  $\boldsymbol{\phi}$ , and noise-to-interference ratio (NIR) estimation. We define the numerical value of NIR as  $\rho = \sigma_a^2 / \sigma_e^2$ . Different weights on the  $\text{tr}[\text{CRB}(\boldsymbol{\theta}, \mathbf{r})]$  summation can be introduced; for example assigning larger weights on the components of CRB related to DOA estimation means considering the localization accuracy with

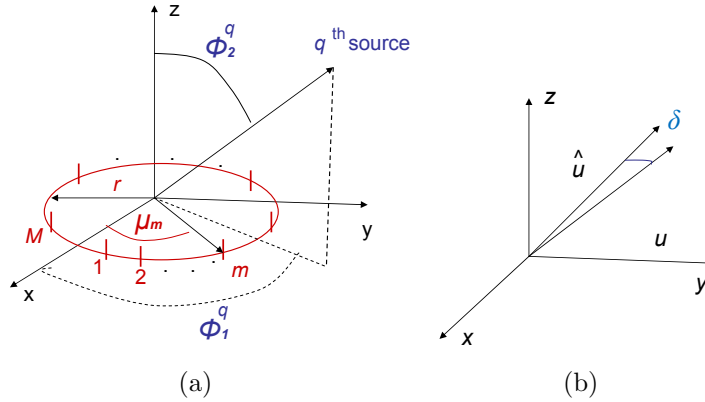


Figure 3.5: (a) Circular array and a source . (b) Angular Error

a higher importance than NIR estimation. Different choice of weights can further improve the CRB on DOA estimation.

Note that other optimization approaches are possible, for instance using pole placement procedure with feedback on  $\mathbf{H}_I$ .

### 3.2.4 Circular Antenna Array With Biologically Inspired Coupling

In this section, we extend our analysis to design biologically inspired coupled circular antenna array, and compute CRB on three dimensional (3D) localization error.

To obtain the measurement model, we generalize the steering matrix  $\mathbf{A}(\boldsymbol{\phi})$  in (3.1). Assuming  $M$ -antenna circular array, and  $Q$  sources impinging on the array:

- $\mathbf{A}(\boldsymbol{\phi}) = [\mathbf{a}(\phi_1^1, \phi_2^1) \cdots \mathbf{a}(\phi_1^Q, \phi_2^Q)]$  is the array response, with  $\phi_1^q$  and  $\phi_2^q$  as the azimuth and and the elevation of the  $q^{th}$  source respectively, see Fig.3.5(a);
- $\mathbf{a}(\phi_1^q, \phi_2^q) = [\exp(-j\omega\Delta_1^q), \dots, \exp(-j\omega\Delta_M^q)]$  for a circular array;

- $\Delta_m^q = \frac{r \sin(\phi_2^q) \cos(\phi_1^q - \mu_m)}{v}$  (see Fig. 3.5(a), and [84]) where
  - $r$  is the radius of the circular array,
  - $\mu_m$  is the azimuth angle of the location of the  $m^{\text{th}}$  antenna,
  - $v$  is the speed of the signal propagation.

The statistical assumptions on the input signal and noise are the same as we defined in Section 3.2.1, but for the circular antenna array we have:

- $\phi = [\phi_1^1, \phi_2^1, \dots, \phi_1^Q, \phi_2^Q]^T$  is the  $2Q \times 1$  vector of deterministic unknown DOA parameters (azimuth and elevation for each source).

We apply the same procedure that we explained in Section 3.2.1 to obtain the BIC among the circular array elements.

To compute the CRB on azimuth and elevation estimation, we modify (3.16) such that

- $\theta = [\rho, \phi_1^1, \phi_2^1, \dots, \phi_1^Q, \phi_2^Q]^T$  is the  $2Q + 1 \times 1$  vector of deterministic unknown parameters
- $\mathbf{1}$  is a  $2Q + 1 \times 2Q + 1$  matrix of ones, and
- $\mathbf{D} = [\mathbf{D}_1 \ \cdots \ \mathbf{D}_{2Q+1}]$ .

For each source, we define  $\text{MSAE}_{\text{CR}}^{s_q}$  as the lower bound on the mean-square angular error (MSAE), 3D direction of arrival (azimuth and elevation) estimation error ( $\delta$  in Fig. 3.5(b)), which is a function of the CRBs of the azimuth and elevation [99].

$$\text{MSAE}_{\text{CR}}^q(\phi_1^q, \phi_2^q, \mathbf{r}) = N [\sin^2(\phi_2^q) \cdot \text{CRB}(\phi_1^q, \mathbf{r}) + \text{CRB}(\phi_2^q, \mathbf{r})], \quad (3.21)$$

where  $\text{CRB}(\phi_1^q, \mathbf{r})$  and  $\text{CRB}(\phi_2^q, \mathbf{r})$  are the CRB on the azimuth and elevation estimation errors corresponding to the  $q^{\text{th}}$  source, respectively. Recall from Section 3.2.3 that the CRBs on DOA estimation depend on the real parts of the characteristic function,  $\mathbf{r}$ .

For the circular array with BIC, we change the utility function for the optimum BIC selection algorithm that we propose in Section 3.2.3 to include the  $\text{MSAE}_{\text{CR}}^q(\phi_1^q, \phi_2^q, \mathbf{r})$  of all the incoming signals:

$$\underset{\mathbf{r}}{\text{argmin}} \quad \text{tr} \left[ \sum_{q=1}^Q \text{MSAE}_{\text{CR}}^q(\phi_1^q, \phi_2^q, \mathbf{r}) + \text{CRB}(\rho, \mathbf{r}) \right] \quad \text{s.t. } r_1 - r_2 > 0, \quad (3.22)$$

where  $\text{CRB}(\rho, \mathbf{r})$  is the CRB on the noise-to-interference ratio ( $\rho$ ) estimation error, which also depends on the real parts of the characteristic function roots,  $\mathbf{r}$ . The cost function in (3.22) is similar to (3.20) such that both are the summations of the estimation error variances.

### 3.2.5 Numerical Results

We compare the localization performances of the biologically inspired coupled and standard multiple-antenna arrays using Monte Carlo simulations. By BIC and standard arrays we refer to the systems with and without the BIC. In these examples, we focus on the optimally designed BIC as described in Section 3.2.3. We follow

the statistical assumptions mentioned in Section 3.2.1. We first compare the performances of the BIC array and HT processor for two antenna systems, then for multiple antenna systems we compare the BIC array with the multi-channel cross-correlation method. Under our statistical assumptions both HT processor and multi-channel cross-correlation methods asymptotically reduce to the ML estimation of DOA using standard antenna array. Therefore for comparison, we demonstrate the results of the ML estimation of the DOA and compute the corresponding CRB using the standard antenna array and the antenna array with BIC (BIC array). We use the following scenario for the multiple-antenna array.

**For Uniform Linear Array (ULA):**

- 5 identical dipole antennas.
- $d = 0.1\lambda$  and  $d = 0.2\lambda$  inter-element distances.

**For Uniform Circular Array (UCA):**

- 6 identical dipole antennas.
- $r = 0.1\lambda$  and  $r = 0.2\lambda$  as different radius values for the circular array.

**For Both ULA and UCA:**  $f_c = 1$  GHz is the carrier and  $f_1 = 0.99$  GHz and  $f_2 = 1.01$  GHz are the resonant frequencies (as also explained in Section 3.2.1), and  $\rho = \sigma_a^2/\sigma_c^2 = 0.5$  is the NIR.

We focus on the small-sized arrays and demonstrate the effect of the BIC on DOA estimation accuracy. Such compact arrays are very important for civil and military



purposes to be used in tactical and mobile applications which are confined in small spaces.

We define the signal-to-noise ratio,  $\text{SNR} = \frac{\text{tr}[\tilde{\mathbf{A}}\mathbf{P}\tilde{\mathbf{A}}]}{\sigma_n^2 \text{tr}[\boldsymbol{\Sigma}(\rho)]}$  and root mean-square error,  $\text{RMSE} = \sqrt{\frac{1}{\text{MC}} \sum_{i=1}^{\text{MC}} (\hat{\phi}_i - \phi_0)^2}$ , where MC is the number of the Monte Carlo simulations,  $\phi_0$  is the true value of DOA and  $\hat{\phi}_i$  is the estimate of the true DOA at the  $i^{\text{th}}$  simulation. In our examples, we obtain the results after 1000 Monte Carlo runs, MC= 1000.

Using two-antenna arrays, we compare our approach with the HT processor and demonstrate our results in Figs. 3.6 and 3.7. In these figures the true value of the azimuth of the DOA,  $\phi_0 = 55^\circ$ . As we explain in Section 3.1, the HT processor is identical to the ML estimator using standard array and hence it achieves the CRB. Moreover it was shown that other GCC methods are equivalent to the HT processor under low SNR conditions [85], and the performance of a GCC method can be measured using the CRB on DOA estimation [91] and [92]. Therefore, under low SNR conditions, which is reasonable for antenna array systems operating as passive radar systems etc., we focus on the HT processor (ML estimation using standard array) to compare our approach.

In Figs. 3.6(a) and 3.6(b), for a fixed SNR=-10 dB, we plot the RMSE on the maximum likelihood estimation of direction of arrival, and CRB of DOA estimation for the standard and BIC two-antenna arrays with  $d = 0.1\lambda$  and  $d = 0.2\lambda$  inter-element spacings, respectively. We observe that the CRB on DOA estimation error and RMSE of MLE are smaller for the BIC array, meaning a decrease in estimation error and an improvement in the localization performance. The MLE algorithm attains the bound asymptotically.

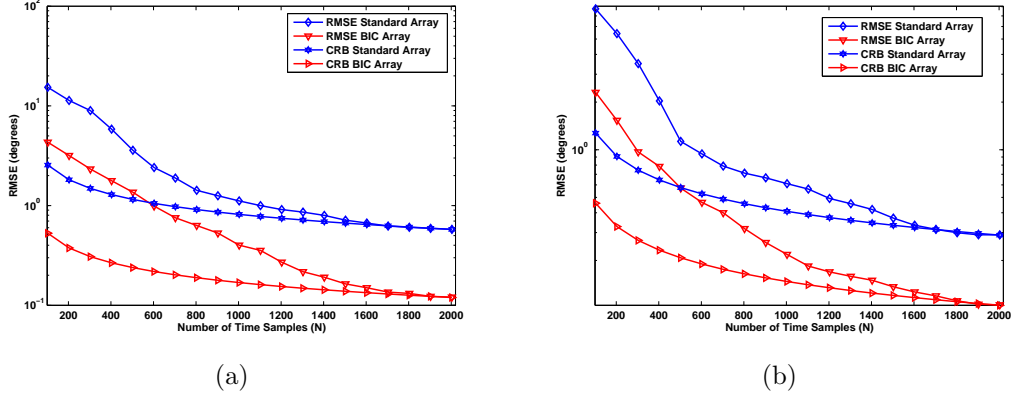


Figure 3.6: Square-root of the mean-square error in the direction estimation and corresponding Cramér-Rao bounds vs. number of time samples for the standard (blue) and BIC (red) uniform linear arrays with different inter-element spacings,  $d$ , and SNR=-10 dB. (a)  $d = 0.1\lambda$ . (b)  $d = 0.2\lambda$

In Fig. 3.7, for  $N = 10$  time samples, we plot the CRB on DOA estimation for the standard and BIC two-antenna arrays for different SNR values and demonstrate the decrease in the minimum bound on the estimation error due to the BIC. Figs. 3.6 and 3.7 confirm that the BIC decreases the minimum bound on estimation error and improves the performance of DOA estimation compared to the HT processor. The physical reason of the improvement in the localization performance is that the BIC works as a two-input two-output filter as shown in Fig. 3.4, magnifying the phase differences (time differences) between the signals received at successive antennas and creating a virtual array with a larger aperture. The HT processor is also a pre-filtering procedure, however it is different than the BIC filter such that the cross-filtering in Fig. 3.4 is not present for the HT processor, see also [85]. Note that in these examples the improvement effect of the BIC increases as the inter-element spacing of the array,  $d$ , decreases.

We extend our results to the BIC uniform linear array with multiple antennas, we demonstrate our results on estimation of direction of arrival in Figs. 3.8, 3.9, 3.10

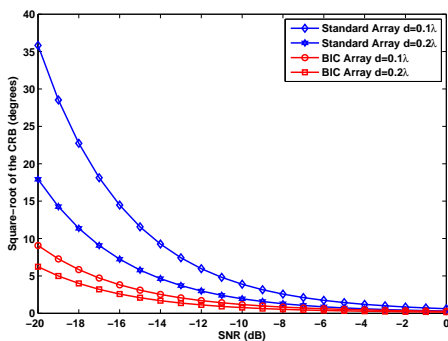


Figure 3.7: Square-root of the Cramér-Rao bound on direction of arrival estimation vs. SNR for standard and BIC uniform linear arrays with  $d = 0.1\lambda$  and  $d = 0.2\lambda$  inter-element spacings and  $N=10$  time samples.

and 3.12. In Figs. 3.8(a) and 3.8(b) for a fixed SNR=-10 dB and the true value of the azimuth of DOA,  $\phi_0 = 55^\circ$ , we plot the RMSE for the maximum likelihood estimation of DOA, and CRB of DOA estimation for the standard and BIC arrays with  $d = 0.1\lambda$  and  $d = 0.2\lambda$  inter-element spacings, respectively. We observe that the CRB on DOA estimation error and RMSE of MLE are smaller for the BIC array, meaning a decrease in estimation error and an improvement in the localization performance. Moreover the MLE algorithm attains the bound asymptotically. BIC array outperforms the standard array in ML estimation of DOA accuracy. Therefore asymptotically BIC array is better than the multi-channel cross-correlation method, which is asymptotically the ML estimation of DOA using standard array.

In Fig. 3.9, for  $N = 10$  time samples and  $\phi_0 = 55^\circ$ , we plot the CRB on DOA estimation for the standard and BIC uniform linear arrays for different SNR values and demonstrate the decrease in the minimum bound on the estimation error due to the BIC. Figs. 3.8 and 3.9 confirm that the BIC decreases the minimum bound on estimation error and improves the performance of DOA estimation. Comparisons of Figs. 3.6 and 3.8, and Figs. 3.7 and 3.9 demonstrate that there is performance

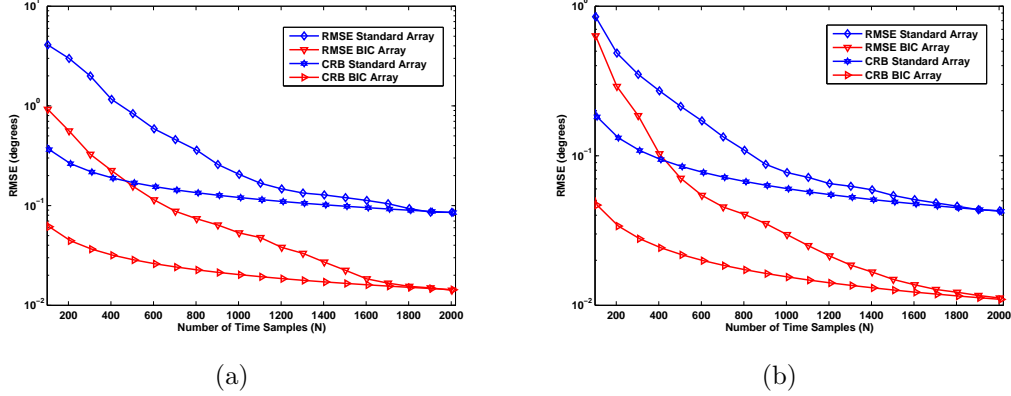


Figure 3.8: Square-root of the mean-square error in the direction estimation and corresponding Cramér-Rao bounds vs. number of time samples for the standard (blue) and BIC (red) uniform linear arrays with different inter-element spacings,  $d$ , and SNR=-10 dB. (a)  $d = 0.1\lambda$ . (b)  $d = 0.2\lambda$

improvement in extending the two-antenna array to multiple-antenna linear array. In the multiple-antenna case, the BIC works as a multi-input multi-output filter creating a virtual array with a larger aperture.

In Fig. 3.10, we illustrate the CRB on the error of the DOA estimation as a function of the azimuth values of the DOA for fixed  $N = 10$  time samples and SNR= -10 dB. We observe that the BIC array always outperforms the standard array, and as the azimuth increases the estimation accuracy increases.

In Fig. 3.11, for fixed  $N = 10$  time samples and SNR= -10 dB, we demonstrate the CRB on the error of DOA estimation as a function of the inter-element spacing of the antennas ( $d$ ). We observe that the improvement due to the BIC decreases as  $d$  increases. For  $d = 0.5\lambda$ , the performances of the standard and the BIC array are the same. We conclude that for the antenna systems that have inter-element spacings lower than  $0.5\lambda$ , the BIC provides an improvement in the localization performance. From a practical standpoint this comparison favors even more BIC over standard

arrays. Indeed, it is very hard to implement a standard array with small  $d$  due to the unwanted coupling among close elements. However, a BIC array may be designed to absorb, to a certain extent, the unwanted coupling. This will be the subject of further work.

In Fig. 3.12, we show the performances of the BIC and standard linear arrays for multiple incoming sources. In this example the inter-element distance is  $d = 0.2\lambda$ . For the linear array with, since we use  $M = 5$  antennas for our examples, we assume the maximum number of the incoming sources is  $Q = 4$  (in order to have a well-posed problem.) Well-posedness is a necessary condition for the Fisher information matrix to be nonsingular (see [100] for details). For this figure  $55^\circ$ ,  $10^\circ$ ,  $45^\circ$ , and  $85^\circ$  are the azimuths of the true DOA of the incoming sources 1, 2, 3 and 4, respectively. In this figure, we plot the CRB on DOA estimation as a function of the SNR for the first source in the presence of multiple sources. Other sources have similar results, but due to the space limitation, we do not show those results here. For  $Q = 2$ , we use the sources 1 and 2, for  $Q = 3$  we use sources 1,2 and 3 etc. We observe that the BIC array has better localization performance than the standard array in the presence of multiple sources.

In Figs 3.13, 3.14, 3.15 and 3.16, we demonstrate the CRB results on the errors of 3D DOA estimations for the BIC circular array. In Figs 3.13 and 3.14, the true value of the elevation,  $\phi_{01}$  and azimuth,  $\phi_{02}$  of the DOA are  $(\phi_{01}, \phi_{02}) = (45^\circ, 55^\circ)$ . In Fig. 3.13, for circular arrays of radius  $r = 0.1\lambda$  and  $r = 0.2\lambda$ , we plot the CRB on the azimuth and elevation estimations as a function of SNR. Similar to the uniform linear array case, we observe that the BIC improves both the elevation and azimuth estimation; the improvement in the elevation estimation is higher than the azimuth estimation; as the size of the array gets smaller the effect of the BIC increases. To gain

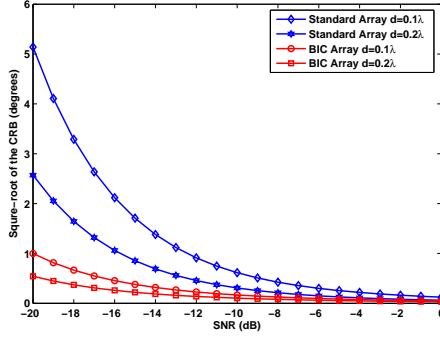


Figure 3.9: Square-root of the Cramér-Rao bound on direction of arrival estimation vs. SNR for standard (blue), and BIC (red) uniform linear arrays with different inter-element spacings,  $d = 0.1\lambda$  and  $d = 0.2\lambda$ , and  $N=10$  time samples.

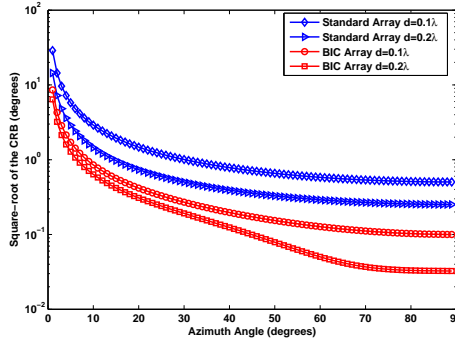


Figure 3.10: Square-root of the Cramér-Rao bound on direction of arrival estimation vs. direction of arrival (azimuth) for standard (blue), and BIC (red) uniform linear arrays with different inter-element spacings,  $d = 0.1\lambda$  and  $d = 0.2\lambda$ ,  $N=10$  time samples, and  $\text{SNR} = -10$  dB.

more physical insight into the 3D localization error, we also illustrate the  $\text{MSAE}_{\text{CR}}$ , a quality that measures 3D angular error, see Fig. 3.5(b), as a function of the SNR in Fig. 3.14, which confirms the improvement provided by the BIC.

In Fig. 3.15, we plot the  $\text{MSAE}_{\text{CR}}$  as a function of the elevation of the DOA for fixed azimuth,  $\phi_{02} = 55^\circ$ . Note that for UCA,  $\text{MSAE}_{\text{CR}}$  is constant w.r.t. the azimuth of the DOA. We demonstrate that for different elevation angles, the BIC array has

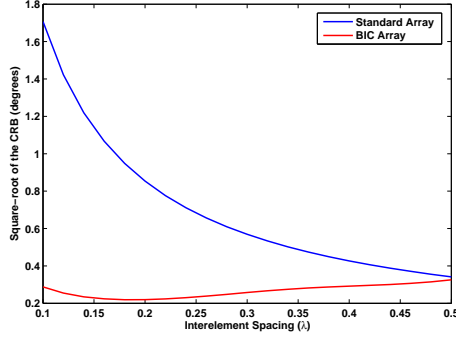


Figure 3.11: Square-root of the Cramér-Rao bound on direction of arrival estimation vs. inter-element spacing ( $d$ ) for standard (blue), and BIC (red) uniform linear arrays, SNR=  $-10$  dB and  $N=10$  time samples.

always better localization performance than the standard array, and as the elevation angle increases the localization performance also increases.

For multiple incoming sources, we plot the  $\text{MSAE}_{\text{CR}}$  as a function of the SNR in Fig. 3.16. We illustrate the results for a circular array of radius,  $r = 0.2\lambda$ . To have a well-posed problem, we assume the maximum number of the incoming signals,  $Q = 4$ . For this figure,  $(45, 55)$ ,  $(10, 80)$ ,  $(30, 70)$  and  $(20, 65)$  are the true DOA of the incoming sources 1, 2, 3 and 4, respectively. Similar to Fig. 3.12, for  $Q = 2$ , we use the sources 1 and 2, for  $Q = 3$  we use sources 1,2 and 3 etc; and demonstrate the  $\text{MSAE}_{\text{CR}}$  value for the first source in the presence of multiple sources. We observe that for multiple incoming signals the BIC array outperforms the standard array.

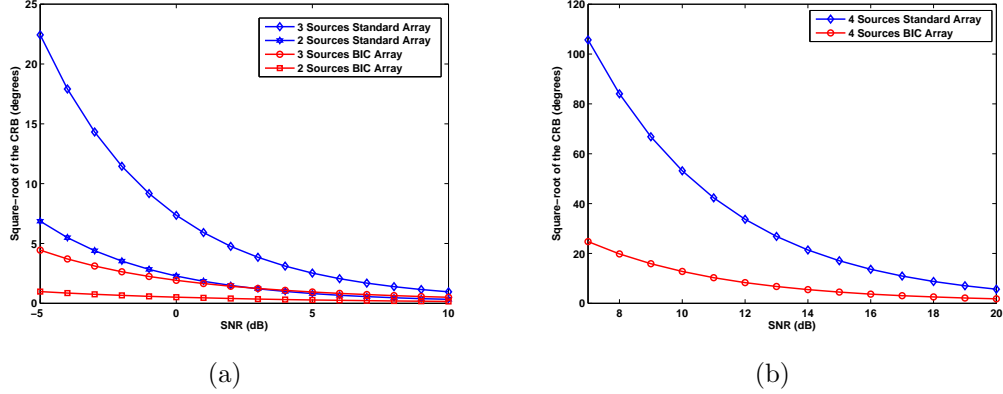


Figure 3.12: Square-root of the Cramér-Rao bound on direction of arrival estimation vs. SNR for standard (blue), and BIC (red) uniform linear arrays with different number of sources,  $M$ ,  $N=10$  time samples. (a)  $M = 2, 3$ . (b)  $M = 4$ .

### 3.3 Biologically Inspired Coupled Antenna Beam-pattern Design

The concept of electrically small antenna arrays with high radiation performance, superdirective (supergain) arrays, is quite old [84], and has attracted antenna researchers for the last few decades. Different methods have been proposed to achieve the superdirectivity namely by decoupling the antennas (reducing the effects of the undesired electromagnetic coupling among the antennas) and changing the current distributions applied to the array elements [101], [102], [103], [104]. In this section, inspired by the female *Ormia*'s coupled ears, we show that applying biologically inspired coupling amongst antennas is beneficial to achieve high radiation performance. Our goal is to demonstrate the effect of the BIC on the radiation performance. The implementation of the BIC system and the investigation of the relationship between the superdirective arrays and the BIC system remain as a future work. We would like to note that our approach, namely employing BIC, might be also used to complement



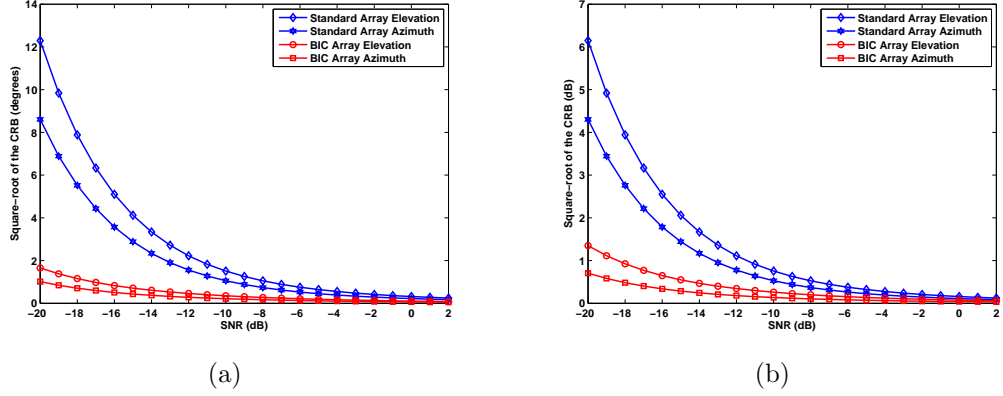


Figure 3.13: Square-root of the Cramér-Rao bound on direction of arrival estimation vs. SNR for the standard (blue) and BIC (red) circular arrays of radius (a)  $r = 0.1\lambda$  (b)  $r = 0.2\lambda$  and  $N=10$  time samples.

the existing superdirective array design methods that overcome issues; for example, the effect of the undesired coupling on individual antenna impedance.

### 3.3.1 Array Factor

In this section, we compute the array factor of the proposed biologically inspired uniform linear array (ULA). We start with the array factor of a standard ULA, positioned without loss of generality along the z-axis (see Fig. 3.17). Since we focus on systems confined in small spaces, we also consider the undesired electromagnetic coupling between the array elements.

Under the far-field radiation and narrow-band signal assumption, we modify the uniform linear array factor to include the undesired coupling between the elements (see also [105]):

$$\text{AF}(\theta) = \sum_{m=1}^M p_m \exp(-j(m-1)(\omega\Delta + \beta)), \quad (3.23)$$

where,

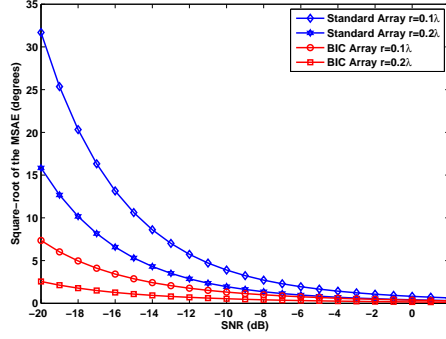


Figure 3.14: Square-root of the mean-square angular error vs. SNR for the standard (blue), and BIC (red) circular arrays with different radius values,  $r = 0.1\lambda$  and  $r = 0.2\lambda$ ,  $N=10$  time samples.

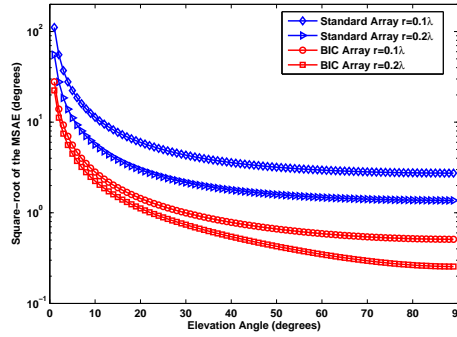
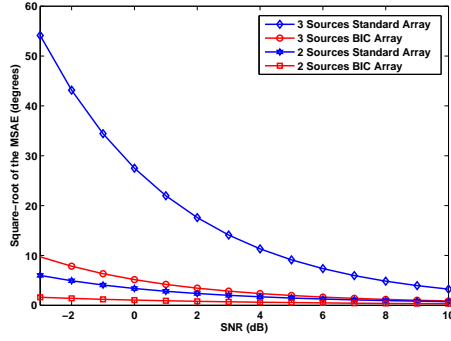
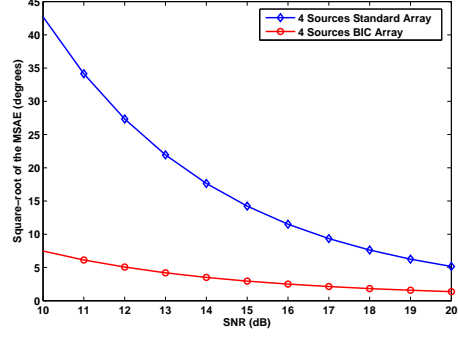


Figure 3.15: Square-root of the mean-square angular error vs. DOA angle (elevation) for the standard (blue), and BIC (red) circular arrays with different radius values,  $r = 0.1\lambda$  and  $r = 0.2\lambda$ ,  $N=10$  time samples, and SNR=  $-10$  dB.

- $\text{AF}(\theta)$  is the radiation pattern (desired amplitude and phase in each direction) of  $M$ -element array assuming isotropic antennas, which depends on the positions and excitations of the sensing elements in the system
- $\mathbf{p} = [p_1, \dots, p_M]^T = \mathbf{C}\mathbf{v}_g$  is the vector of the currents on the antennas
- $\mathbf{v}_g = [v_1, \dots, v_M]^T$  is the vector of generator (excitation) voltages at the input of the antennas



(a)



(b)

Figure 3.16: Square-root of the mean-square angular error vs. SNR for the standard (blue), and BIC (red) circular arrays with different number of sources,  $M$ ,  $N=10$  time samples. (a)  $M = 2, 3$  (b)  $M = 4$ .

- $\mathbf{C}$  is the undesired electromagnetic coupling between the array elements, (a transformation matrix, transforming generator voltages to the induced currents on each antenna)
- $\omega = 2\pi f$  with  $f$  as the frequency of the radiated signal
- $\Delta = \frac{d \cos \theta}{v}$  is the inter-element time difference
- $d$  is the inter-element distance
- $v$  is the speed of signal propagation in the medium
- $\theta$  is the elevation angle (see Fig. 3.17), and
- $\beta$  is the excitation phase.

We compute  $\mathbf{C}$  similar to [105] as a function of self and mutual impedances between the antennas (see also discussions in [106] and [107]). We summarize the computation of  $\mathbf{C}$  in Appendix B. When the mutual impedances are zero, when there is no electromagnetic coupling,  $\mathbf{C}$  reduces to a diagonal matrix. We compute the self and

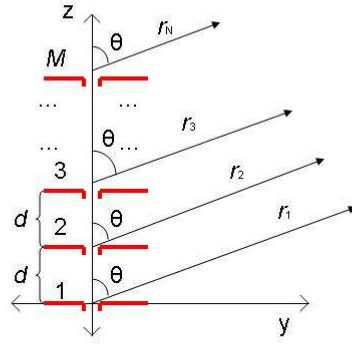


Figure 3.17: Far-field radiation geometry of  $M$ -element antenna array.

mutual impedances, assuming finite-length dipole antennas as the elements of the array, as explained in [84, Chapter 8], see also section 3.3.4. Note that the standard literature often ignores  $\mathbf{C}$ , which is reasonable for sufficiently large inter-elemental distances.

The usual goal of the array-factor design is to select the excitation voltages,  $\mathbf{v}_g$ , and phase,  $\beta$ , to obtain a desired radiation pattern. Our goal is to include the BIC in the array factor for fixed  $\mathbf{v}_g$  and  $\beta$  values and demonstrate the improvement in the directivity gain, half-power beamwidth (HPBW) and side lobe level (SLL) of the radiation pattern.

### Biologically Inspired Coupled Array Factor

We generalize (3.23) to include also the coupling biologically inspired by the Ormia's coupled ears. First, we obtain the response of the Ormia's coupled ears. We convert this response to fit the desired radio frequencies and obtain the BIC. Then we modify the array factor to also include BIC. We follow the discussions in Section 3.2.1 to

obtain the frequency responses of the converted system and compute the ratio

$$\frac{H_2(\omega, \Delta)}{H_1(\omega, \Delta)} = \frac{D_1(j\omega)e^{-j\omega\Delta} - N(j\omega)}{D_2(j\omega) - N(j\omega)e^{-j\omega\Delta}} \quad (3.24)$$

choosing the frequency  $\omega$  depending on the application (see also section 3.3.4).

To apply the BIC concept to the array factor in (3.23), we replace the exponential terms in (3.23) with the ratio in (3.24)

$$\text{AF}_I(\theta) = \sum_{m=1}^M p_m \left( \frac{H_2(\omega, \Delta, \beta)}{H_1(\omega, \Delta, \beta)} \right)^{(m-1)}, \quad (3.25)$$

where

$$\frac{H_2(\omega, \Delta, \beta)}{H_1(\omega, \Delta, \beta)} = \frac{D(j\omega) \exp(-j(\omega\Delta + \beta)) - N(j\omega)}{D(j\omega) - N(j\omega) \exp(-j(\omega\Delta + \beta))},$$

with  $D(j\omega)$  and  $N(j\omega)$  as defined after (3.3), substituting  $s = j\omega$ . We assume identical antennas  $D_1(j\omega) = D_2(j\omega) = D(j\omega)$ . The ratio in (3.24) generalizes the exponential terms in (3.23) to include the BIC.

Note that  $N(j\omega)$  represents the BIC and when there is no coupling ( $N(j\omega) = 0$ ),  $\text{AF}_I(\theta)$  in (3.25) reduces to  $\text{AF}(\theta)$  in (3.23). In this paper, we analytically demonstrate the biologically inspired beam pattern design. The actual implementation is left for future work.

### 3.3.2 Radiation Intensity, Directivity, Half-power Beamwidth and Side Lobe Level

In this section, we describe our measures to analyze the radiation performance. First, taking into account the antenna factor (element factor) and the BIC, we compute the

radiation intensity of the antenna array in a given direction [84]

$$U_I(\theta, \phi) = [\text{EF}(\theta, \phi)]_n^2 [\text{AF}_I(\theta)]_n^2, \quad (3.26)$$

where

- $[\text{EF}(\theta, \phi)]_n$  is the normalized element factor, far-zone electric field of a single element (in our work we assume that the array is formed with finite-length dipoles, see also section 3.3.4)
- $[\text{AF}_I(\theta)]_n$  is the normalized array factor, and
- $U_I(\theta, \phi)$ , the radiation intensity in a given direction, is the power radiated from an antenna array per unit solid angle.
- Hence the radiated power  $P_{\text{rad}}$  is

$$P_{\text{rad}} = \int_0^{2\pi} \int_0^\pi U_I(\theta, \phi) \sin \theta \, d\theta \, d\phi,$$

where  $\theta$  and  $\phi$  are the elevation and azimuth angles, respectively,  $\sin \theta \, d\theta \, d\phi$  is the unit solid angle.

Using the radiation intensity, we consider the following measures to analyze the performance of the beampattern design:

- The directivity,  $D_I(\theta, \phi)$ , is the ratio of the radiation intensity in a given direction to the average radiation intensity.

$$D_I(\theta, \phi) = \frac{4\pi U_I(\theta, \phi)}{P_{\text{rad}}}, \quad (3.27)$$

where  $\frac{1}{4\pi}P_{\text{rad}}$  is the average radiation intensity over all angles. In our work, for comparison purposes, we consider the directivity gain in a desired direction (at elevation  $\theta = 0^\circ$  and azimuth  $\phi = 90^\circ$ , see also section 3.3.4).

- Half-power beamwidth, HPBW, in terms of the elevation angle,  $\theta$ , for a fixed azimuth angle,  $\phi$ . HPBW is defined as the angle between two half-power directions [84].
- Sidelobe level (SLL) defined as the maximum value of the radiation pattern in any direction other than the desired one (direction other than  $\theta = 0^\circ$  on  $\phi = 90^\circ$  plane for our case).

The directivity gain, HPBW and SLL measure how effectively the power is directed (steered) in a given direction. For a good performance, it is desirable to have large  $D_1(\theta, \phi)$ , small SLL and narrow HPBW in a desired direction.

### 3.3.3 Optimization of the Biologically Inspired Coupling

In this section, we develop a method to maximize the radiation performance by optimizing the BIC. We formulate the optimization problem to improve the radiation performance. For an antenna array, we choose the directivity gain in a desired direction as the utility function to be maximized. This is a reasonable choice since the directivity gain is also related to the SLL and the HPBW of the radiation pattern. Generally it is true that the patterns with smaller SLL and HPBW values have larger directivity gain. Therefore, we formulate the problem as

$$\begin{aligned} &\text{maximize} && D_1(\theta, \phi) \\ &\text{subject to} && r_1 - r_2 > 0, \end{aligned} \tag{3.28}$$

where  $\theta$  and  $\phi$  are the elevation and the azimuth of the desired direction of transmission. Recall the discussions in section 3.2.3 for the condition on  $r_1$  and  $r_2$ , which are the free parameters in  $\frac{H_2(\omega, \Delta, \beta)}{H_1(\omega, \Delta, \beta)}$  of (3.25), not the distances to antennas 1 and 2 in Fig. 3.17.

### 3.3.4 Numerical Examples for Beampattern Design

In this section, we compare the radiation performances of the BIC and standard antenna arrays. For comparison, we plot the radiation pattern and compare the directivity gain, half-power beamwidths and sidelobe attenuation of these systems. Similar to Section 3.2.5, by BIC and standard arrays we refer to the systems with and without the BIC. BIC parameters are optimally designed using the algorithm described in section 3.3.3. We use the following scenario:

- We consider uniform (uniform excitation voltages) ordinary and binomial (binomial expansion coefficients as the excitation voltage values) end-fire arrays [84, Chapter 8], maximum at  $\theta = 0^\circ$ , then  $\beta = -w\Delta$
- Frequency of interest,  $f = 1$  GHz
- Uniform linear array composed of 20 identical dipole antennas
- The undesired coupling matrices,  $\mathbf{C}$  for  $0.5\lambda$ -wavelength antenna system with different inter-element distances ( $d = 0.25\lambda$  and  $d = 0.1\lambda$ ) are calculated according to [84, Chapter8] for finite-length thin-dipole antennas, and
- The antennas are located on the z-axis parallel to y-axis, then assuming azimuth  $\phi = 90$  (on the y-z plane, see Fig. 3.17), the element factor for a finite-length



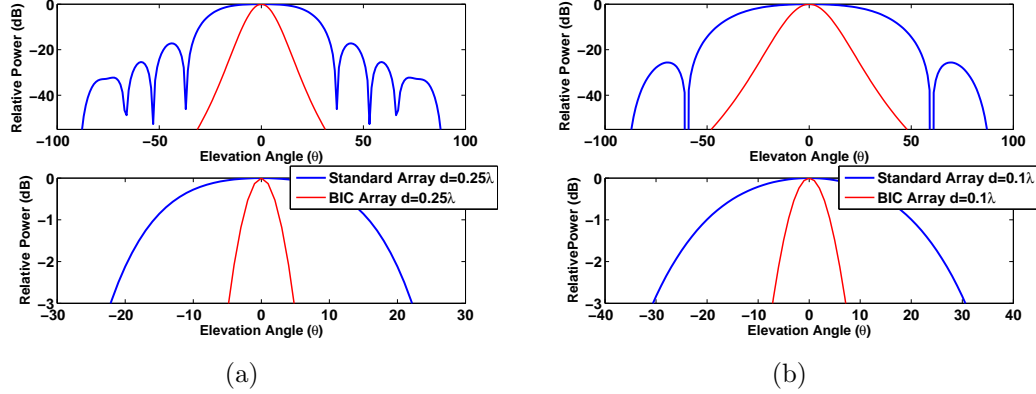


Figure 3.18: Power patterns of the uniform ordinary end-fire antenna arrays using standard (blue), and BIC (green) for (a)  $d = 0.25\lambda$ , (b)  $d = 0.1\lambda$  inter-element spacings. The bottom halves of the figures present the half-power beamwidth.

dipole antenna is computed as

$$EF(\theta, 90^\circ) = \left[ \frac{\cos(\frac{kl}{2} \sin \theta) - \cos(\frac{kl}{2})}{\cos \theta} \right].$$

where  $k = \frac{2\pi}{\lambda}$ ,  $\lambda$  is the wavelength of the radiated signal and  $l$  is the length of each antenna.

Recall that we focus on 2-D beampattern design in terms of elevation angle,  $\theta$ .

We demonstrate our results for standard, and BIC arrays in Figures 3.18 and 3.19, and summarize the calculated directivity gains, and HPBW values in Tables 3.1 and 3.2, respectively. We observe that the BIC array with uniform excitation voltages outperforms the uniform standard array in terms of sidelobe suppression, directivity, and HPBW (see Fig. 3.18, and Tables 3.1 and 3.2). For binomial array, in Fig. 3.19, we observe that neither the standard nor the BIC array have sidelobes, but the BIC array has much narrower HPBW and hence better directivity gain (see also Tables 3.1 and 3.2). The physical reason of the improvement in the radiation performance is that the

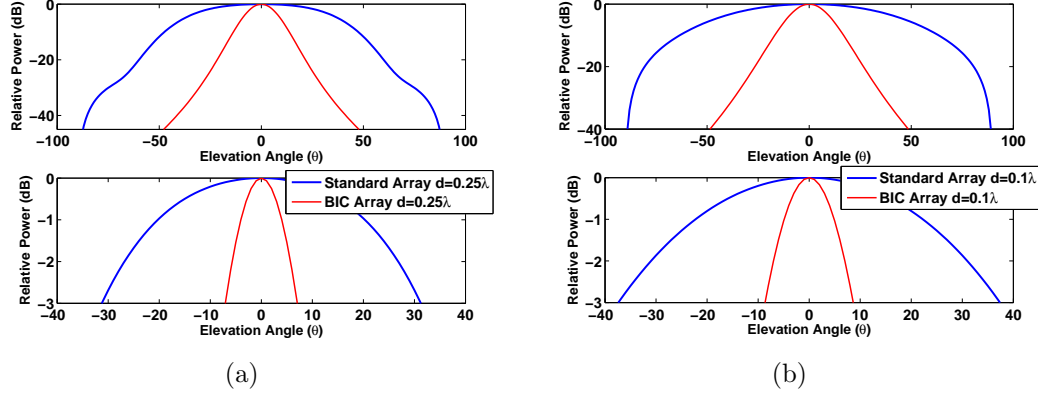


Figure 3.19: Power patterns of the binomial end-fire antenna arrays using standard (blue), and BIC (green) for (a)  $d = 0.25\lambda$ , (b)  $d = 0.1\lambda$  inter-element spacings. The bottom halves of the figures present the half-power beamwidth.

	Uniform		Binomial	
	$d = 0.25\lambda$	$d = 0.1\lambda$	$d = 0.25\lambda$	$d = 0.1\lambda$
Standard Array	13.96	10.77	10.81	8.08
BIC Array	25.62	22.16	22.75	20.35

Table 3.1: Directivity gains of the antenna arrays in the desired direction  $\theta = 0^\circ$  and  $\phi = 90^\circ$  (dB)

BIC works as a multi-input multi-output filter, magnifying the amplitude and phase differences (time differences) between the outputs of the successive antennas and creating a virtual array with a larger aperture. In the beam pattern design, the virtual array with larger aperture creates a radiation pattern with higher directivity and sidelobe suppression, and lower half-power beamwidth. Note that in these examples the effect of the BIC increases as the distance between the antennas,  $d$ , decreases.

	Uniform		Binomial	
	$d = 0.25\lambda$	$d = 0.1\lambda$	$d = 0.25\lambda$	$d = 0.1\lambda$
Standard Array	45°	62°	63°	76°
BIC Array	9.8°	14.6°	14.2°	17.4°

Table 3.2: Half-power beamwidths of the antenna arrays (degrees)

### 3.4 Summary

We designed a small-sized multiple-antenna array with couplings biologically inspired by the mechanically coupled ears of *Ormia ochracea*. First, we obtained the response of the mechanical model representing the coupling between the *Ormia*'s ears. We then converted this response to the desired radio frequencies. Assuming uniform linear antenna array, we implemented the biologically inspired coupling using the converted system as a multi-input multi-output filter, and obtained a passive antenna system with BIC. For the resulting system, we derived the maximum likelihood estimates of the direction of arrival and computed the Cramér-Rao lower bound on estimation error as a performance measure. We extended our analysis to consider circular arrays and computed the mean-square angular error bound on the 3D localization error. We later developed an active transmitting antenna array with BIC. For the resulting system we computed the directivity gain, half-power beamwidth, and side lobe level as radiation performance measures. For both the passive and active antenna arrays, we proposed an algorithm to optimally choose the BIC for maximum localization and radiation performance. With numerical examples we demonstrated the improvement in localization and radiation performance due to the BIC.

# Chapter 4

## Adaptive MIMO Radar Design and Detection in Compound-Gaussian Clutter<sup>4</sup>

We consider target detection with multiple-input multiple-output (MIMO) radars under high-resolution and/or low-grazing-angle transmission scenarios in the presence of sea or foliage clutter. We model the clutter using a compound-Gaussian distribution. This distribution fits well with the heavy-tailed statistics of the clutter in such scenarios. We first choose an inverse gamma distribution as the clutter texture, and accordingly introduce a measurement model. We present a parameter-expanded expectation-maximization (PX-EM) algorithm to estimate the target and clutter parameters. Using these estimates, we then formulate a statistical decision test based on the generalized likelihood ratio test (GLRT). Moreover, we develop an adaptive power distribution algorithm, based on the asymptotical characteristics of the GLRT,

---

<sup>4</sup>Based on M. Akcakaya and A. Nehorai, “Adaptive MIMO Radar Design and Detection in Compound-Gaussian Clutter” *IEEE Trans. Aerospace and Electronic Systems*, accepted for publication ©[2010] IEEE.

to improve the detection performance of the radar system. With Monte Carlo simulations, we demonstrate the advantages of MIMO radar and the proposed adaptive algorithm.

## 4.1 Introduction

Target detection for MIMO systems has been addressed with white and colored Gaussian noise in [45] and [52], respectively. However, real clutter often deviates from the complex Gaussian model. We model the clutter reflections at the receiver with a compound-Gaussian model. This model represents the heavy-tailed clutter statistics that are distinctive of several scenarios, e.g., high-resolution and/or low-grazing-angle radars in the presence of sea or foliage clutter [108], [109]. The compound-Gaussian clutter  $\mathbf{e} = \sqrt{u}\mathcal{X}$ , where  $u$  and  $\mathcal{X}$  are the texture and speckle components of the compound model, respectively. The fast-changing  $\mathcal{X}$  is a realization of a stationary zero mean complex Gaussian process, and the slow-changing  $u$  is modeled as a nonnegative real random process [110]. Gamma distribution for the texture is investigated in [53] for MIMO radar systems, leading to the well-known K-clutter model. In this work, we specifically consider the inverse gamma distribution for texture component  $u$ , since similar to its gamma distributed counterpart inverse gamma fits well with real clutter data [62]. Moreover this choice of distribution simplifies in a closed-form maximum likelihood solution for the joint target and clutter estimation as it follows a complex multivariate-t distribution [111].

The applications investigated for MIMO radar assume that the total energy is divided equally among the transmitters (see [31, Chapters 8 and 9]). We believe that this assumption may not be optimal, since MIMO radar systems are sensitive to RCS

variations of the target w.r.t. angle and since transmitting signals with different energies from different transmitters may change the total received power under the same environmental conditions.

In the following, we demonstrate our analytical and numerical results on target detection MIMO radar under compound-Gaussian clutter assumption using generalized likelihood ratio test (GLRT) [68], [112].

## 4.2 Radar Model

In this section, we develop measurement and statistical models for a MIMO radar system to detect a target in the range cell of interest (COI). Our goal is to present an algorithm, within a generalized multivariate analysis of variance (GMANOVA) framework [113] when the signal and noise parameters are unknown.

### 4.2.1 Measurement Model

We consider a two dimensional (2D) system with  $M$  transmitters and  $N$  receivers. Define  $(x_{\text{T}x_m}, y_{\text{T}x_m})$ ,  $m = 1, \dots, M$ , and  $(x_{\text{R}x_n}, y_{\text{R}x_n})$ ,  $n = 1, \dots, N$ , as the locations of the transmitters and receivers, respectively. We also assume a stationary point like target located at  $(x_0, y_0)$  and having reflection coefficient values changing w.r.t. the angle aspect (e.g., multiple scatterers, which cannot be resolved by the transmitted signals, with  $(x_0, y_0)$  as the center of gravity) [31]. Define the complex envelope of the signal from the  $m^{\text{th}}$  transmitter as  $\beta_m s_m(t)$ ,  $m = 1, \dots, M$ , such that  $|\beta_m|^2$  is the transmitted energy with  $\sum_{m=1}^M |\beta_m|^2 = E$  ( $E$  is constant for any  $M$ ) and

$\int_{T_s} |s_m(t)|^2 dt = 1$ ,  $m = 1, \dots, M$ , with  $T_s$  as the signal duration. We write the lowpass equivalent of the received signal at the  $n^{\text{th}}$  receiver following [31]:

$$r_n(t) = \sum_{m=1}^M \alpha_{nm} x_{nm} \beta_m s_m(t - \tau_{nm}) e^{-j\psi_{nm}} + e_n(t), \quad (4.1)$$

where

- $x_{nm}$  is the complex target reflection coefficient seen by the  $m^{\text{th}}$  transmitter and  $n^{\text{th}}$  receiver pair, such that the amplitude of  $x_{nm}$  corresponds to the radar cross section (RCS)
- $\alpha_{nm} = \sqrt{\frac{G_{tx} G_{rx} \lambda^2}{(4\pi)^3 R_m^2 R_n^2}}$  is the channel parameter from the  $m^{\text{th}}$  transmitter to the  $n^{\text{th}}$  receiver, with  $G_{tx}$  and  $G_{rx}$  as the gains of the transmitting and receiving antennas, respectively;  $\lambda$  as the wavelength of the incoming signal;  $R_m = \sqrt{(x_{\text{Tx}_m} - x_0)^2 + (y_{\text{Tx}_m} - y_0)^2}$  and  $R_n = \sqrt{(x_{\text{Rx}_n} - x_0)^2 + (y_{\text{Rx}_n} - y_0)^2}$  as the distances from transmitter and receiver to target, respectively
- $\tau_{nm} = (R_m + R_n)/c$ , and  $c$  is the speed of the signal propagation in the medium
- $\psi_{nm} = 2\pi f_c \tau_{nm}$ , with  $f_c$  as the carrier frequency, and
- $e(t)$  is additive clutter noise.

To enable the data separation at the receiver side due to the reflection of the multiple transmitted signals from the target, we assume low-cross-correlation transmitted signals. The design of signals with these properties is a challenging research subject [58], but to simplify the problem and demonstrate our methods and analysis, we assume that the assumed signal characteristics are met (this assumption is commonly made in MIMO radar, see [31, Chapters 8 and 9] and references therein.) Hence, we

apply matched-filtering and range gating, then obtain the output of the  $n^{\text{th}}$  receiver corresponding to the  $i^{\text{th}}$  transmitter:

$$r_{ni} = \beta_i \alpha_{ni} x_{ni} e^{-j\psi_{ni}} + e_{ni}, \quad (4.2)$$

where  $r_{ni} = \int_{\tau_{ni}}^{\tau_{ni}+T_s} r_n(t) s_i^*(t - \tau_{ni}) dt$ , and  $e_{ni} = \int_{\tau_{ni}}^{\tau_{ni}+T_s} e_n(t) s_i^*(t - \tau_{ni}) dt$ . Since we apply range gating, we represent the range cell of interest using the delay  $\tau_{ni}$  observed by the  $n^{\text{th}}$  receiver and  $i^{\text{th}}$  transmitter. Note that different transmitter receiver pairs have different delays corresponding to the same range cell of interest. However since we know the array configuration and the range cell of interest, we assume we have the knowledge of these delays. Moreover  $\tau_{ni}$  might be interpreted as the sampling time after the match filtering for the signal transmitted by the  $i^{\text{th}}$  transmitter and received by the  $n^{\text{th}}$  receiver representing the range cell of interest, see for example [114].

Then, combining the received data corresponding to the transmitted signal  $s_i(t)$  for one pulse, we obtain

$$\mathbf{r}_i = \mathbf{A}_i \mathbf{x}_i + \mathbf{e}_i, \quad (4.3)$$

where

- $\mathbf{r}_i = [r_{1i}, \dots, r_{N_i}]^T$
- $\mathbf{A}_i = \beta_i \text{diag}(\alpha_{1i} e^{-j\psi_{1i}}, \dots, \alpha_{N_i} e^{-j\psi_{N_i}})$
- $\mathbf{x}_i = [x_{1i}, \dots, x_{N_i}]^T$ , and
- $\mathbf{e}_i = [e_{1i}, \dots, e_{N_i}]^T$ .



We stack the receiver outputs corresponding to all the signals into an  $NM \times 1$  vector

$$\mathbf{y} = \mathbf{A}\mathbf{x} + \mathbf{e}, \quad (4.4)$$

where

- $\mathbf{y} = [\mathbf{r}_1^T, \dots, \mathbf{r}_M^T]^T$
- $\mathbf{A} = \text{blkdiag}(\mathbf{A}_1, \dots, \mathbf{A}_M)$
- $\mathbf{x} = [\mathbf{x}_1^T, \dots, \mathbf{x}_M^T]^T$ , and
- $\mathbf{e} = [\mathbf{e}_1^T, \dots, \mathbf{e}_M^T]^T$ .

We transmit  $K$  pulses and assume that the target is stationary during this observation time; then

$$\mathbf{Y} = [\mathbf{y}(1) \ \mathbf{y}(2) \ \cdots \ \mathbf{y}(K)]_{NM \times K} = \mathbf{A}\mathbf{x}\boldsymbol{\phi} + \mathbf{E}, \quad (4.5)$$

where  $\boldsymbol{\phi} = [1, \dots, 1]_{1 \times K}$ , and  $\mathbf{E} = [\mathbf{e}(1) \ \mathbf{e}(2) \ \cdots \ \mathbf{e}(K)]_{NM \times K}$  is the additive noise.

## 4.2.2 Statistical Model

In (4.5), we assume that  $\mathbf{x}$  (target reflection coefficients) is an unknown deterministic. We consider the compound-Gaussian distribution  $\mathbf{e}(k) = \sqrt{u}\mathcal{X}(k)$ ,  $k = 1, \dots, K$ , to model the clutter with  $u$  and  $\mathcal{X}(k)$  as the texture and speckle components, respectively; see [111] and references therein. The realizations of the fast-changing component,  $\mathcal{X}(k)$ ,  $k = 1, \dots, K$ , are independent and identically distributed (i.i.d.) and follow a complex Gaussian distribution with zero mean and covariance  $\boldsymbol{\Sigma}$ . The texture is the slow-changing component; thus, we consider it to be constant during

the coherent processing interval (CPI), but changing from CPI to CPI according to a probability density function of a non-negative random variable [110], [115]. Therefore,  $\mathbf{e}(k)|u$   $k = 1, \dots, K$ , are i.i.d., and we can write the conditional distribution for the observation  $\mathbf{Y}$  in (4.5) as

$$\prod_{k=1}^K p_{\mathbf{y}|u}(\mathbf{y}(k)|u) = \prod_{k=1}^K \frac{1}{|\pi u \boldsymbol{\Sigma}|} \exp \left\{ -[\mathbf{y}(k) - \mathbf{A}\mathbf{x}\phi(k)]^H \cdot [u\boldsymbol{\Sigma}]^{-1} [\mathbf{y}(k) - \mathbf{A}\mathbf{x}\phi(k)] \right\}. \quad (4.6)$$

Observe that conditioned on  $u$ , with known  $\mathbf{A}$  and  $\boldsymbol{\phi}$  and unknown  $\mathbf{x}$  and  $\boldsymbol{\Sigma}$ , (4.5) is a GMANOVA model. We assume that  $w = 1/u$  follows the gamma distribution (consequently  $u$  follows the inverse gamma distribution) with unit mean and unknown shape parameter  $v > 0$  as in [111]; *i.e.*,

$$p_w(w; v) = \frac{1}{\Gamma(v)} v^v w^{v-1} \exp[-vw], \quad (4.7)$$

where  $\Gamma(\cdot)$  is the gamma function. Therefore, we consider  $\mathbf{x}$ ,  $\boldsymbol{\Sigma}$ , and  $v$  as the unknown parameters.

### 4.3 Detection and Estimation Algorithms

We compute in this section the maximum likelihood estimates (MLE) of the unknown parameters, and the target detection test. There is no closed form solution for the MLEs of the unknown parameters, and hence we apply a parameter-expanded expectation-maximization (PX-EM) algorithm to estimate the clutter texture and

speckle as well as the target parameters [63]. Note that we define  $\mathbf{y}$ ,  $u$ , and  $(\mathbf{y}, u)$  as the observed, unobserved, and complete data, respectively.

Using the MLEs of the unknown parameters in the observed-data likelihood function, we derive a statistical decision test based on the GLRT to determine the presence of a target in the COI. We choose between two hypotheses  $\mathcal{H}_0$  (the target-free case) and  $\mathcal{H}_1$  (the target-present case) with the speckle covariance  $\Sigma$  and the inverse texture shape parameter  $v$  as the nuisance parameters. We compute the GLRT by replacing the unknown parameters with their MLEs in the likelihood ratio test. Then, we reject  $\mathcal{H}_0$  in favor of  $\mathcal{H}_1$  when

$$\text{GLRT} = \frac{p_1(\mathbf{Y}; \hat{\mathbf{x}}_1, \hat{\Sigma}_1, \hat{v}_1)}{p_0(\mathbf{Y}; \hat{\Sigma}_0, \hat{v}_0)} > \eta, \quad (4.8)$$

where

- $p_0(\cdot)$  and  $p_1(\cdot)$  are the observed-data likelihood functions under  $\mathcal{H}_0$  and  $\mathcal{H}_1$
- $\hat{\Sigma}_0$  and  $\hat{\Sigma}_1$  are the MLEs of  $\Sigma$ , and  $\hat{v}_0$  and  $\hat{v}_1$  are the MLEs of the shape parameter  $v$  under  $\mathcal{H}_0$  and  $\mathcal{H}_1$ , respectively
- $\hat{\mathbf{x}}_1$  is the MLE of  $\mathbf{x}$  under  $\mathcal{H}_1$ , and
- $\eta$  is the detection threshold.

We compute the observed-data likelihood function

$$p_1(\mathbf{Y}; \mathbf{x}, \Sigma, v) = \frac{\Gamma(v + KNM)}{|\pi\Sigma|^K \Gamma(v) v^{KNM}} \left( 1 + \sum_{k=1}^K [\mathbf{y}(k) - A\mathbf{x}\phi(k)]^H [\Sigma]^{-1} [\mathbf{y}(k) - A\mathbf{x}\phi(k)] / v \right)^{-v-KNM} \quad (4.9)$$

and under  $\mathcal{H}_0$ ,  $p_0(\mathbf{Y}; \Sigma, v)$  is the same as (4.9) with  $\mathbf{x} = \mathbf{0}$ .

We compute the MLEs of the vector  $\mathbf{x}$ , speckle covariance matrix  $\Sigma$ , and texture distribution shape parameter  $v$  using the hierarchical data model presented in (4.6) and (4.7). Similar to the work presented in [111], we apply two iterative loops for the MLE computations: (i) inner loop and (ii) outer loop. In the inner loop, first we introduce the PX-EM algorithm to obtain the MLEs of  $\hat{\mathbf{x}}$ , and  $\hat{\Sigma}$  for a fixed  $v$ . The PX-EM algorithm has the same convergence properties as the classical EM algorithm, but it outperforms the EM algorithm in global rate of convergence [63]. In the outer loop, we estimate  $v$  using the MLEs from the inner loop [111].

### Inner Loop

PX-EM algorithm for inverse gamma texture.

Recall that  $\mathbf{x}$ ,  $\Sigma$ , and  $v$  are the unknown parameters. We first estimate  $\boldsymbol{\theta} = \{\mathbf{x}, \Sigma\}$ , assuming that  $v$  is known. We implement the PX-EM algorithm by adding a new unknown parameter  $\mu_w$ , the mean of  $w$ , to this set; *i.e.*,  $\boldsymbol{\theta}_* = \{\mathbf{x}, \Sigma_*, \mu_w\}$ . In this model, the maximization step performs a more efficient analysis by fitting the expanded parameter set [63]. Under this expanded model the pdf of  $w$  is

$$p_w(w; v, \mu_w) = \frac{1}{\Gamma(v)} \left( \frac{v}{\mu_w} \right)^v w^{v-1} \exp[-vw/\mu_w]. \quad (4.10)$$

Consider  $\boldsymbol{\theta} = R(\boldsymbol{\theta}_*) = \{\mathbf{x}, \Sigma_*/\mu_w\}$ , where  $R(\cdot)$  is the reduction function (many-to-one) from the expanded to the original space. Moreover,  $\mu_w^0 = 1$  is the null value such that the complete-data model is preserved.

We define  $i$  and  $j$  as the inner and outer loop iteration indexes, respectively. Since the complete-data likelihood function belongs to an exponential family, the PX-EM algorithm reduces to first obtaining the conditional mean of the sufficient statistics using the unobserved data given the observed data, and then plugging these sufficient statistics values in the MLE expressions of the unknown variables (see also [111], [116]).

**PX-E Step:** Calculate the conditional expectation of the sufficient statistics under  $\mathcal{H}_1$ , concentrated at  $\hat{v}^{(j)}$ , the  $j^{\text{th}}$  iteration step estimate of  $v$ .

Using the properties of the compound-Gaussian model with inverse gamma distributed texture [117], we observe that  $w|\mathbf{Y}$  follows a gamma distribution with

$$\hat{w}_1^{(i)} = \mathbb{E}_{w|\mathbf{Y}}[w|\mathbf{Y}; \hat{\boldsymbol{\theta}}_*^{(i)}] = (\hat{v}^{(j)} + KMN) \cdot \left\{ \hat{v}^{(j)} + \sum_{k=1}^K d(k, \hat{\boldsymbol{\theta}}_*^{(i)}) \right\}^{-1}, \quad (4.11)$$

where  $\hat{\boldsymbol{\theta}}_*^{(i)} = \{\hat{\mathbf{x}}^{(i)}, \hat{\boldsymbol{\Sigma}}_*^{(i)}, \hat{\mu}_w^{(i)} = \hat{\mu}_w^0 = 1\}$  is the estimate of  $\boldsymbol{\theta}_*$  at the  $i^{\text{th}}$  iteration and  $d(k, \hat{\boldsymbol{\theta}}_*^{(i)}) = [\mathbf{y}(k) - A\hat{\mathbf{x}}^{(i)}\phi(k)]^H [\hat{\boldsymbol{\Sigma}}_*^{(i)}]^{-1} [\mathbf{y}(k) - A\hat{\mathbf{x}}^{(i)}\phi(k)]$ . Then,

$$\mathbf{T}_1^{(i)} = \frac{1}{K} \sum_{k=1}^K \mathbf{y}(k)\phi(k)^H \hat{w}_1^{(i)}, \quad (4.12a)$$

$$\mathbf{T}_2^{(i)} = \frac{1}{K} \sum_{k=1}^K \mathbf{y}(k)\mathbf{y}(k)^H \hat{w}_1^{(i)}, \quad (4.12b)$$

$$\mathbf{T}_3^{(i)} = \frac{1}{K} \sum_{k=1}^K \phi(k)\phi(k)^H \hat{w}_1^{(i)}, \quad (4.12c)$$

$$T_4^{(i)} = \hat{w}_1^{(i)}. \quad (4.12d)$$

**PX-M Step:** We obtain the maximum likelihood estimates similar to [113]

$$\hat{\boldsymbol{x}}_1^{(i+1)} = \left[ A^H \left( \boldsymbol{S}^{(i)} \right)^{-1} A \right]^{-1} A^H \left( \boldsymbol{S}^{(i)} \right)^{-1} \boldsymbol{T}_1^{(i)} \left( \boldsymbol{T}_3^{(i)} \right)^{-1}, \quad (4.13a)$$

$$\begin{aligned} \hat{\boldsymbol{\Sigma}}_*^{(i+1)} &= \left( \boldsymbol{S}^{(i)} \right)^{-1} + \left[ I_{MN} - \boldsymbol{Q}^{(i)} \left( \boldsymbol{S}^{(i)} \right)^{-1} \right] \boldsymbol{T}_1^{(i)} \left( \boldsymbol{T}_3^{(i)} \right)^{-1} \\ &\quad \cdot \left( \boldsymbol{T}_1^{(i)} \right)^H \left[ I_{MN} - \boldsymbol{Q}^{(i)} \left( \boldsymbol{S}^{(i)} \right)^{-1} \right]^H, \end{aligned} \quad (4.13b)$$

$$\hat{\mu}_w^{(i+1)} = T_4^{(i)}, \quad (4.13c)$$

$$\hat{\boldsymbol{\Sigma}}_1^{(i+1)} = \hat{\boldsymbol{\Sigma}}_*^{(i+1)} / \hat{\mu}_w^{(i+1)}, \quad (4.13d)$$

where  $\boldsymbol{S}^{(i)} = \boldsymbol{T}_2^{(i)} - \boldsymbol{T}_1^{(i)} \left( \boldsymbol{T}_3^{(i)} \right)^{-1} \left( \boldsymbol{T}_1^{(i)} \right)^H$  and  $\boldsymbol{Q}^{(i)} = A \left[ A^H \left( \boldsymbol{S}^{(i)} \right)^{-1} A \right]^{-1} A^H$ .

Under  $\mathcal{H}_0$ , we calculate  $\hat{\boldsymbol{\Sigma}}_0$  and  $\hat{w}_0$  with  $\boldsymbol{x} = \mathbf{0}$  and update the sufficient statistics accordingly.

## Outer Loop

MLE of the shape parameter of the inverse gamma texture.

We compute  $\hat{v}^{(j+1)}$  by maximizing the concentrated observed data  $(\boldsymbol{y}(k), k = 1, \dots, K)$  log-likelihood function using the estimates from the PX-EM step. We denote  $\hat{\boldsymbol{x}}^{(\infty)}$ ,  $\hat{\boldsymbol{\Sigma}}_0^{(\infty)}$ , and  $\hat{\boldsymbol{\Sigma}}_1^{(\infty)}$  as the estimates of  $\boldsymbol{x}$  and  $\boldsymbol{\Sigma}$  obtained upon the convergence of the inner loop and compute

$$\left[ \hat{v}_1^{(j+1)} \right]^T = \underset{v}{\operatorname{argmax}} \left[ \ln p_1 \left( \boldsymbol{Y}, \hat{\boldsymbol{x}}_1^{(\infty)}, \hat{\boldsymbol{\Sigma}}_1^{(\infty)}, v \right) \right] \quad (4.14)$$

Under  $\mathcal{H}_0$ , we calculate  $\hat{v}_0^{(j+1)}$  using  $\boldsymbol{x} = \mathbf{0}$  and  $\hat{\boldsymbol{\Sigma}}_0^{(\infty)}$  in (4.14).

The GLRT (4.8), computed upon convergence of (4.12), (4.13) and (4.14) under  $\mathcal{H}_0$  and  $\mathcal{H}_1$ , results in a complicated form which is not possible to analyze statistically. Therefore, we simplify it to the ratio of determinants of the covariance estimates under different hypotheses, (see (4.15)), which is also similar to the general form of GLRT presented in [113], to analyze its statistical characteristics (see Section 4.4). First, for a fixed texture component, we compute the GLRT. Then we assume that the target is present only in the range cell of interest and the texture is completely correlated over few neighboring range cells. Since the texture is the slow changing component, this assumption is reasonable for high resolution radar (see also [53]). Next, using the data from the target-free neighboring cells as the secondary data, we run the inner and outer loops of the estimation algorithm to compute the conditional mean of the texture component in (4.11) given the secondary data. We replace the texture component with its corresponding conditional mean value reducing the GLRT to

$$\lambda = \frac{|\mathbf{T}_2^{(\infty)}|}{\left| \mathbf{T}_2^{(\infty)} - \mathbf{Q}^{(\infty)} \left( \mathbf{S}^{(\infty)} \right)^{-1} \mathbf{T}_1^{(\infty)} \left( \mathbf{T}_3^{(\infty)} \right)^{-1} \left( \mathbf{T}_1^{(\infty)} \right)^{-1} \right|} > \eta', \quad (4.15)$$

where  $|\cdot|$  is the determinant operator, and  $\mathbf{T}_1^{(\infty)}$ ,  $\mathbf{T}_2^{(\infty)}$ ,  $\mathbf{T}_3^{(\infty)}$ ,  $\mathbf{S}^{(\infty)}$  and  $\mathbf{Q}^{(\infty)}$  are obtained using (4.11) in (4.12) in one step. That is, using the secondary data and the PX-EM algorithm the conditional mean of the texture component is computed as in (4.11). Then using (4.11) in (4.12), (4.15) is computed in one step.

## 4.4 Adaptive Design

In this section, we first demonstrate the asymptotic statistical characteristics of the detection test derived in Section 4.3. Based on this result, we then construct a utility

function for adaptive energy allocation to improve the detection performance. We determine the optimum transmitted energy by each transmitter according to this utility function.

We define  $\hat{w}_s^\infty$  as the conditional mean value of the texture component obtained from (4.11) upon the convergence of (4.12) and (4.14) using the target free secondary data. Note that since the unknown parameters  $\Sigma$ , and  $v$  of the secondary data belong to a canonical exponential family (since the complete-data likelihood function belongs to an exponential family and could be written in canonical form), their estimates are consistent and hence the conditional mean value in (4.11), computed given the secondary data, converges to the minimum mean-square error estimate (MMSE) of the texture component in probability (converges in probability) as the number of the observations increases (asymptotically) [116, Theorem 5.2.2]. Moreover from Theorem 5.5.2 and Theorem 5.5.3 of [116], we know that the MMSE asymptotically converges to MLE with probability 1 (almost surely). Therefore, since MLE is consistent in probability,  $\hat{w}_s^\infty$  asymptotically converges to the true texture value  $w_0$  in probability.

The test  $\lambda$  in (4.15) is a function of  $\hat{w}_s^\infty \mathbf{y}(k)$  for  $k = 1, \dots, K$ . We observe that  $\hat{w}_s^\infty \rightarrow w_0$  and  $\hat{w}_s^\infty \mathbf{y}(k) \rightarrow w_0 \mathbf{y}(k) = \mathbf{z}(k)$  in probability, such that  $\mathbf{z}(k) \sim \mathbb{CN}(\mathbf{0}, \Sigma)$  and  $\mathbb{CN}(\mathbf{A}\mathbf{x}\phi, \Sigma)$  under  $\mathcal{H}_0$  and  $\mathcal{H}_1$ , respectively. Then from [116, Appendix A.14.8],  $\lambda(\hat{w}_s^\infty \mathbf{y}(k))$  asymptotically converges to  $\lambda(\mathbf{z}(k))$  for  $k = 1, \dots, K$  in distribution. Moreover following a similar approach taken for real Gaussian random variables in [118], [119], we find that (4.15), as a function of  $\mathbf{z}(k)$  (complex version of Wilks' lambda) as  $K \rightarrow \infty$ ,  $K \ln \lambda$  has a complex chi-square distribution with  $NM$  degrees of freedom under  $\mathcal{H}_0$ . Since this distribution does not depend on the speckle covariance, in the limit (4.15) is asymptotically a constant false-alarm rate (CFAR) test.



Under  $\mathcal{H}_1$ , as  $K \rightarrow \infty$ ,  $K \ln \lambda$  has a non-central complex chi-square distribution with  $NM$  degrees of freedom. That is,  $K \ln \lambda \sim \mathbb{C}\chi_{NM}^2(\delta)$  [118], [120]. The non-centrality parameter is

$$\delta = \text{tr}(\mathbf{\Sigma}^{-1}(\mathbf{A}\mathbf{x}\boldsymbol{\phi})(\mathbf{A}\mathbf{x}\boldsymbol{\phi})^H). \quad (4.16)$$

We observe that detection performance is optimized by maximizing the detection probability for a fixed value of probability of false alarm. It is shown in [120] that, under asymptotic approximation, the non-centrality parameter and probability of detection are positively proportional. Therefore we maximize the non-centrality parameter with respect to the energy parameters,  $\beta_m$ ,  $m = 1, \dots, M$  (see (4.3) and (4.4) for the relation between the non-centrality parameter, and  $\beta$ 's). We also incorporate an energy constraint in the maximization,  $\sum_{m=1}^M |\beta_m|^2 = E$ , such that the total transmitted energy is the same, independent of the system configuration and energy distribution. We define  $\boldsymbol{\beta} = [\beta_1, \dots, \beta_M]^T$ , then the optimization problem reduces to

$$\hat{\boldsymbol{\beta}} = \underset{\boldsymbol{\beta}}{\text{argmax}} \left[ \text{tr}(\mathbf{\Sigma}^{-1}(\mathbf{A}\mathbf{x}\boldsymbol{\phi})(\mathbf{A}\mathbf{x}\boldsymbol{\phi})^H) - \mu \left( \sum_{m=1}^M |\beta_m|^2 - E \right) \right], \quad (4.17)$$

where  $\mu$  is the Lagrange multiplier. Without loss of generality, we assume  $E = 1$ , then after some algebraic manipulations using the structure of matrix  $\mathbf{A}$  from (4.4), we show that this optimization problem further reduces to

$$\hat{\boldsymbol{\beta}} = \underset{\boldsymbol{\beta} \text{ s.t. } \boldsymbol{\beta}^T \boldsymbol{\beta} = 1}{\text{argmax}} [\boldsymbol{\beta}^T \mathbf{P} \boldsymbol{\beta}], \quad (4.18)$$

where  $\mathbf{P}$  is computed as in Appendix C such that

$$\begin{aligned}\mathbf{P} &= K \text{diag}(p_{11}, \dots, p_{MM}), \\ &= K \text{diag}((\bar{\mathbf{A}}_1 \mathbf{x}_1)^H \Sigma_1^{-1} (\bar{\mathbf{A}}_1 \mathbf{x}_1), \dots, (\bar{\mathbf{A}}_M \mathbf{x}_M)^H \Sigma_M^{-1} (\bar{\mathbf{A}}_M \mathbf{x}_M)),\end{aligned}\quad (4.19)$$

where (recalling from (4.5))

- $\mathbf{A} = \text{blkdiag}(\mathbf{A}_1, \dots, \mathbf{A}_M)$
- $\mathbf{A}_i = \beta_i \text{diag}(\alpha_{1i} e^{-j\psi_{1i}}, \dots, \alpha_{Ni} e^{-j\psi_{Ni}}) = \beta_i \bar{\mathbf{A}}_i$
- $\mathbf{x} = [\mathbf{x}_1^T, \dots, \mathbf{x}_M^T]^T$
- $\mathbf{x}_i = [x_{1i}, \dots, x_{Ni}]^T$ , and
- $\Sigma = \text{blkdiag}(\Sigma_1, \dots, \Sigma_M)$ , see also Section 4.5 for the covariance matrix assumption.

Here  $q_{mm}$  corresponds to the total received power at all the receivers due to the  $m^{\text{th}}$  transmitter.

We solve (4.18) to obtain the optimum power allocation. This equation has a unique solution such that  $\hat{\boldsymbol{\beta}}$  is the eigenvector corresponding to the largest eigenvalue of the matrix  $\mathbf{P}$ . Since  $\mathbf{P}$  is diagonal, the maximum eigenvalue is the maximum of  $p_{mm}$ ,  $m = 1, \dots, M$ , (maximum total received power at all the receivers, maximum diagonal entry of  $\mathbf{Q}$ ). If  $p_{ii}$  is the maximum eigenvalue, the eigenvector is  $\mathbf{u}_i = [0 \ \dots \ 0 \ 1 \ 0 \ \dots \ 0]$ , all zeros but 1 at the  $i^{\text{th}}$  location. This suggests that for optimum power allocation we transmit all the power from the  $i^{\text{th}}$  transmitter. However, we modify this result and put minimum and maximum power constraints for each

transmitter, this means that for adaptive design we transmit the maximum available power from the transmitter having the maximum eigenvalue, and transmit minimum power from the rest of the transmitters. This approach also provides the positivity constraint. Note that  $\Sigma$ ,  $\mathbf{x}$  are unknown in practice and we replace them with their estimates for the adaptive design.

## 4.5 Numerical Examples

We present numerical examples using Monte Carlo (MC) simulations to illustrate our analytical results. We show the receiver operating characteristics and improvement in detection performance due to adaptive energy allocation for the MIMO system. The results are obtained from  $2 * 10^4$  MC runs. We follow the scenario shown in Fig. 4.1. We assume that our system is composed of  $M$  transmitters and  $N$  receivers, where the antennas are widely separated. The transmitters are located on the y-axis, whereas the receivers are on the x-axis; the target is 10km from each of the axes; the antenna gains ( $G_{tx}$  and  $G_{rx}$ ) are 30dB; the signal frequency ( $f_c$ ) is 1GHz. The angle between the transmitted signals  $a_1 = a_2 = \dots = a_M = 10^\circ$  and similarly between the received signals  $b_1 = \dots = b_N = 10^\circ$ . Hence  $R_m$ ,  $m = 1, \dots, M$ , and  $R_n$ ,  $n = 1, \dots, N$ , in (4.1) are calculated accordingly. In this scenario, all the transmitters and receivers see the target from different angles. Throughout the numerical examples, we choose  $M = 2$  and  $K = 40$  pulses for each transmitted signal.

We choose the spatial covariance of the speckle components in a block diagonal form ( $\Sigma = \text{blkdiag}[\Sigma_1, \dots, \Sigma_M]$ ) due to the assumption of low-cross-correlation signal transmission, see eqns. (4.2) and (4.3).  $\Sigma_m$ ,  $m = 1, \dots, M$ , are positive definite  $N \times N$  matrices with entries  $\Sigma_m[i, j] = \rho_s^{|i-j|}$ , with  $i, j = 1, \dots, N$ . This form

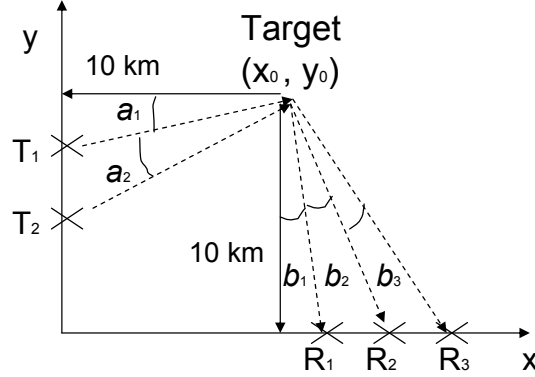
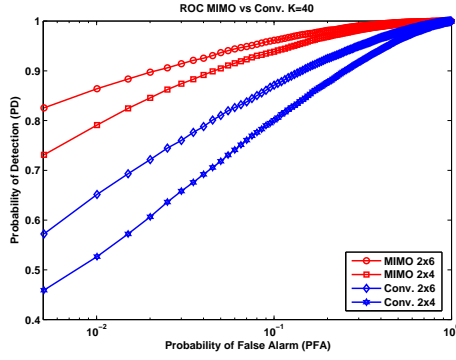


Figure 4.1: MIMO antenna system with  $M$  transmitters and  $N$  receivers.

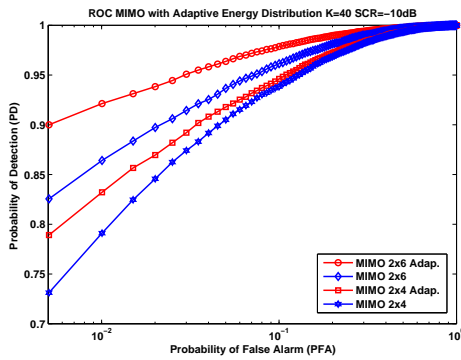
of covariance for MIMO radar is used in [53] to account for the correlation between the received signals at different receivers due to the same transmitter. The target parameters  $\boldsymbol{x}$  are chosen randomly for simulation purposes; that is, the entries are assigned as the realizations of a zero mean complex Gaussian random variable with unit variance. Later,  $\boldsymbol{x}$  is scaled to meet the desired signal-to-clutter ratio (SCR) conditions. We define the SCR similar to [111] in (4.20). Moreover, the shape parameter of the texture component is chosen to be  $v = 4$  (values between 3 and 9 are often good choices for heavy tail fitting [117]).

$$\text{SCR} = \frac{1}{K} \frac{\sum_{k=1}^K (\mathbf{A}\boldsymbol{x}\phi(k))^H (\mathbf{A}\boldsymbol{x}\phi(k))}{\text{E}\{u(k)\} \text{tr}\boldsymbol{\Sigma}}. \quad (4.20)$$

In Fig. 4.2(a). MIMO  $M \times N$  and Conv.  $M \times N$  stand for the MIMO and conventional radar systems, respectively, with  $M$  transmitters and  $N$  receivers. The model of Conv. radar is obtained from (4.1) similar to [45] using the fact that all the channel coefficients of the system (target RCS and distances of the radars to the target) are the same, since each transmitter and receiver pair sees the target from the same angle



(a)



(b)

Figure 4.2: (a) Receiver operating characteristics of MIMO and conventional phased-array radar (Conv.). (b) Receiver operating characteristics of MIMO radar with and without adaptive energy allocation.

and distance. For fairness of comparison, the total transmitted energy,  $E$ , is kept the same for both Conv. and MIMO systems.

In Fig. 4.2(a), we assume for that spatial correlation  $\rho_s = 0.01$  (low correlation due to widely separated setups),  $\text{SCR} = -10$  dB, and the total energy is equally divided among the transmitters. In MIMO radar applications, the use of multiple orthogonal waveforms results in  $10\log_{10}(M)$  dB loss in SCR [31, Chapter8]. Then, for fair comparison, we set  $\text{SCR} = -7$  dB for Conv. system. The observed advantage of MIMO over Conv. radar stems from the diversity gain obtained by multiple looks at the

target. That is, MIMO radar systems have the ability to exploit the spatial diversities, gaining sensitivity about the RCS variations of the target to enhance system performance.

In Fig. 4.2(b), we demonstrate the improvement in the detection performance due to the adaptive energy allocation. We compute the receiver operating characteristics for MIMO radar when the total energy ( $E$ ) is equally divided among the transmitters (MIMO  $M \times N$  on the figure) and subsequently when  $E$  is adaptively distributed among the transmitters using our algorithm (MIMO  $M \times N$  Adap. on the figure). The adaptive method optimally allocates the total energy to transmitters depending on the target RCS values such that the signal-to-clutter ratio increases for the same total energy,  $E$ , and environment conditions. Increasing the SCR under the same target and environment conditions also increases the performance.

## 4.6 Summary

We developed a statistical detector based on GLR for a MIMO radar system in compound-Gaussian clutter with inverse gamma distributed texture when the target and clutter parameters are unknown. First, we introduced measurement and statistical models within the GMANOVA framework and applied the PX-EM algorithm to estimate the unknown parameters. Using these parameters, we developed the statistical decision test detector. Moreover, we asymptotically approximated the statistical characteristics of this decision test and used it to propose an algorithm to adaptively distribute the total transmitted energy among the transmitters. We used Monte Carlo simulations and demonstrated the advantage of MIMO over conventional radar

for target detection and the detection performance enhancement due to our adaptive energy distribution algorithm.

# Chapter 5

## MIMO Radar Detection and Adaptive Design Under a Phase Synchronization Mismatch<sup>5</sup>

Due to imperfect knowledge of the locations and due to the local oscillator characteristics of the antennas, MIMO radars suffer from the phase error between each transmitter and receiver. We address target detection with MIMO radar under such phase errors. We model these phase errors using a von-Mises distribution and accordingly introduce a data measurement model. We develop a generalized likelihood ratio test (GLRT) target detector using estimates of the error distribution parameter, of target returns and of noise variance, all of which we obtain through an estimation algorithm based on an expectation-maximization (EM) algorithm. We compute an upper bound on the mutual information between the radar measurements and the phase error. Using this bound, we then propose an adaptive power distribution algorithm for the MIMO system. With numerical examples, we demonstrate both the

---

<sup>5</sup>Based on M. Akcakaya and A. Nehorai, "MIMO Radar Detection and Adaptive Design Under a Phase Synchronization Mismatch," *IEEE Trans. Signal Process.*, vol.58, no.10, pp.4994-5005, Oct. 2010 ©[2010] IEEE.



advantages of the robust detector that considers the phase error and the improvement in detection performance due to the adaptive power distribution.

## 5.1 Introduction

MIMO radars with widely separated antennas are categorized into two processing modes (i) non-coherent and (ii) coherent, depending on whether the phase information is ignored or included, respectively [31, Chapters 8 and 9]. For the non-coherent mode, with random target assumption, these systems have the ability to improve both target parameter estimation [47] and detection performance [45]; and they can handle slow-moving targets by exploiting Doppler estimates from multiple directions [55], [51].

In addition to the unknown deterministic target parameters assumption, the coherent MIMO radar assumes perfect knowledge of the orientation, location, and local oscillator characteristics of all the antennas (hence a perfect knowledge of phase information). In this mode, the MIMO systems are shown to support high-resolution target localization [46], and to improve target estimation [121] and detection in non-homogeneous clutter [59],[60],[61].

To realistically model the radar measurements, we consider the phase error, which is due to the widely separated nature of the radar system. The effect of the phase error within coherent MIMO radar has been investigated for target estimation [56], [57]. In our work, we develop a generalized likelihood-ratio test (GLRT) target detector for a MIMO radar system in the presence of a phase synchronization mismatch (phase error) between the transmitter and receiver pairs. In practice, the receivers

and transmitters may be frequency synchronized to a master source; however, phase mismatch may still occur due to imperfect knowledge of the locations and to the local oscillator/electronics characteristics of the antennas causing a phase offset between the transmitter receiver pairs [122], [123].

We assume that an estimate of the phase offset is available as a result of the tracking process of a phase-locked loop (PLL). For a transmitter receiver pair, the output of the PLL (the phase estimation error) was shown to follow a von-Mises distribution [124], [125], [126]. Therefore, we model the phase error terms randomly, using a von-Mises distribution (see Fig. 5.1). The von-Mises distribution is used in applications of directional statistics and generalizes the uniform distribution (with a zero shape parameter ( $\Delta = 0$ ), the von-Mises reduces to a uniform distribution) [66]. We model the uncertainty in the phase error using different shape parameters, and we demonstrate its negative effect on detection performance. We observe that an increase in the shape parameter (increasing the concentration of the phase error distribution around the mean value, zero in our case), decreases the uncertainty (the entropy), which corresponds to an increase in detection performance. Our assumption about the phase error distributions generalizes the assumptions in [56] and [57], which are respectively, Gaussian distribution and uniform distribution with a parameter that controls the range of the phase error.

Our work generalizes the coherent MIMO radar assuming the presence of the phase error. As the shape parameter of the phase error distribution goes to infinity, as the uncertainty becomes zero, our model converges to a coherent MIMO radar. Therefore, to demonstrate the effect of our approach, we use measurements that have a phase error and compare our detector with a coherent MIMO radar detector that ignores the phase error. For the non-coherent MIMO radar, the target reflection coefficients are

assumed to be random. An example is a complex Gaussian distribution. This example corresponds to the assumption that the amplitudes of the reflection coefficients follow a Rayleigh distribution and that the phases of the target reflections follow uniform distribution (shape parameter  $\Delta = 0$ ). For different  $\Delta$  values, there is no closed-form solution for the target reflection coefficient distribution, and hence to consider more general cases with different  $\Delta$  values, we assume a deterministic unknown model for the amplitude of the target reflection coefficients.

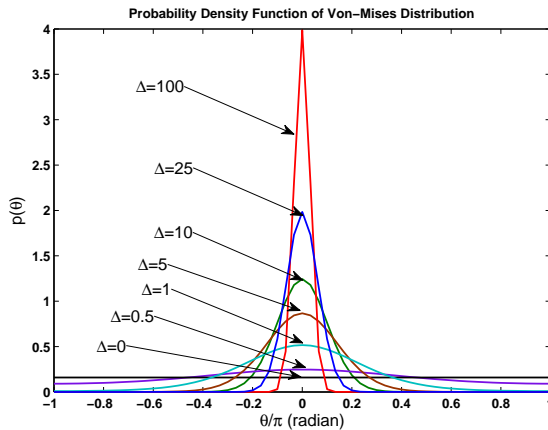


Figure 5.1: Probability density function of von-Mises distribution with shape parameter  $\Delta$ .

We propose an adaptive transmitted energy allocation scheme in Section 5.4. The mutual information (MI) between the received target responses and the radar measurements corresponds to the MI between the phase error and radar measurements. Since an analytical solution does not exist, we compute an upper bound for the latter MI. Then we develop an adaptive energy allocation algorithm that distributes the total transmitted energy among the transmitters, exploiting the RCS sensitivity of the system and optimizing the upper bound on the MI between the phase error and radar measurements. We show that our algorithm improves the detection performance. To study the MI, we follow a similar approach that has been taken for radar waveform

design (c.f. [127], [128]), but we model the randomness of the target returns with the phase error.

## 5.2 Radar Model

In this section, we develop the measurement and statistical models for a MIMO radar system to detect a target in a range cell of interest (COI). We will use these models to present an algorithm within a generalized multivariate analysis of variance (GMANOVA) framework [113] in the presence of the phase error when the signal and noise parameters are unknown.

### 5.2.1 Measurement Model

We consider a two dimensional (2D) spatial system with  $M$  transmitters and  $N$  receivers. Define  $(x_{\text{Tx}_m}, y_{\text{Tx}_m})$ ,  $m = 1, \dots, M$ , and  $(x_{\text{Rx}_n}, y_{\text{Rx}_n})$ ,  $n = 1, \dots, N$ , as the locations of the transmitters and receivers, respectively. We also assume a stationary point target located at  $(x_0, y_0)$  and having radar cross section values changing with respect to different angles (e.g., multiple scatterers, which cannot be resolved by the transmitted signals, with  $(x_0, y_0)$  as the center of gravity) [31]. Define the complex envelope of the narrow-band signal from the  $m^{\text{th}}$  transmitter as  $\beta_m s_m(t)$ ,  $m = 1, \dots, M$ , such that  $|\beta_m|^2$  is the transmitted energy with  $\sum_{m=1}^M |\beta_m|^2 = E$  ( $E$  is constant for any  $M$ ) and  $\int_{T_s} |s_m(t)|^2 dt = 1$ ,  $m = 1, \dots, M$ , with  $T_s$  as the signal duration. We write the low-pass equivalent of the received signal at the  $n^{\text{th}}$  receiver

as follows [31]:

$$r_n(t) = \sum_{m=1}^M \alpha_{nm} \sigma_{nm} \beta_m s_m(t - \tau_{nm}) e^{-j(\psi_{nm} + \theta_{nm})} + e_n(t), \quad (5.1)$$

where

- $\alpha_{nm} = \sqrt{\frac{G_{\text{Tx}} G_{\text{Rx}} \lambda^2}{(4\pi)^3 R_m^2 R_n^2}}$  is the channel parameter from the  $m^{\text{th}}$  transmitter to the  $n^{\text{th}}$  receiver, with  $G_{\text{Tx}}$  and  $G_{\text{Rx}}$  as the gains of the transmitting and receiving antennas, respectively;  $\lambda$  as the wavelength of the incoming signal;  $R_m$  and  $R_n$  as the distances from the  $m^{\text{th}}$  transmitter and  $n^{\text{th}}$  receiver to the target, respectively
- $\sigma_{nm}$  is the amplitude of the target reflection coefficient seen by the  $m^{\text{th}}$  transmitter and  $n^{\text{th}}$  receiver
- $\tau_{nm} = (R_m + R_n)/c$  with  $c$  the speed of the signal propagation in the medium
- $\psi_{nm} = 2\pi f_c \tau_{nm}$ , with  $f_c$  as the carrier frequency
- $\theta_{nm}$  is the phase offset between the  $n^{\text{th}}$  receiver and  $m^{\text{th}}$  transmitter, and
- $e(t)$  is additive noise.

To enable the data separation at the receiver side arriving from the different transmitters, we assume low-cross-correlation transmitted signals. The design of signals with these properties is a challenging research subject [58], but for simplification of the problem and demonstration of our methods and analysis, we assume that the required signal criteria are met (this assumption is commonly made for MIMO radar, see [31, Chapters 8 and 9] and references therein). Moreover, we use a PLL to obtain an estimate of the phase offset between each transmitter and receiver pair. Hence,

we apply matched-filtering and then the PLL, and we obtain the output of the  $n^{th}$  receiver corresponding to the  $i^{th}$  transmitter:

$$r_{ni} = \beta_i \alpha_{ni} \sigma_{ni} e^{-j(\psi_{ni} + \tilde{\theta}_{ni})} + e_{ni}, \quad (5.2)$$

where

- $r_{ni} = \int_{\tau_{ni}}^{\tau_{ni} + T_s} r_n(t) s_i^*(t - \tau_{ni}) dt$
- $\tilde{\theta}_{ni}$  is the output of the PLL (phase error, estimation error), and
- $e_{ni} = \int_{\tau_{ni}}^{\tau_{ni} + T_s} e_n(t) s_i^*(t - \tau_{ni}) dt$ .

Then, combining all the  $N$  received data corresponding to the transmitted signal  $s_i(t)$  for one pulse, we obtain

$$\mathbf{r}_i = \mathbf{A}_i \mathbf{X}_i \boldsymbol{\phi}_i + \mathbf{e}_i, \quad (5.3)$$

where

- $\mathbf{r}_i = [r_{1i}, \dots, r_{Ni}]^T$
- $\mathbf{A}_i = \beta_i \text{diag}(\alpha_{1i} e^{-j\psi_{1i}}, \dots, \alpha_{Ni} e^{-j\psi_{Ni}})$
- $\mathbf{X}_i = \text{diag}(\sigma_{1i}, \dots, \sigma_{Ni})$
- $\boldsymbol{\phi}_i = [e^{-j\tilde{\theta}_{1i}}, \dots, e^{-j\tilde{\theta}_{Ni}}]^T$ , and
- $\mathbf{e}_i = [e_{1i}, \dots, e_{Ni}]^T$ .

We stack the receiver outputs corresponding to all the signals into an  $NM \times 1$  vector:

$$\mathbf{y} = \mathbf{A} \mathbf{X} \boldsymbol{\phi} + \mathbf{e}, \quad (5.4)$$

where

- $\mathbf{y} = [\mathbf{r}_1^T, \dots, \mathbf{r}_M^T]^T$
- $\mathbf{A} = \text{blkdiag}(\mathbf{A}_1, \dots, \mathbf{A}_M)$
- $\mathbf{X} = \text{blkdiag}(\mathbf{X}_1, \dots, \mathbf{X}_M)$
- $\boldsymbol{\phi} = [\boldsymbol{\phi}_1^T, \dots, \boldsymbol{\phi}_M^T]^T$ , and
- $\mathbf{e} = [\mathbf{e}_1^T, \dots, \mathbf{e}_M^T]^T$ .

We transmit  $K$  pulses and assume that the target is stationary during this observation time; then

$$\mathbf{Y} = [\mathbf{y}(1) \ \mathbf{y}(2) \ \dots \ \mathbf{y}(K)]_{NM \times K} = \mathbf{A}\mathbf{X}\boldsymbol{\Phi} + \mathbf{E}, \quad (5.5)$$

where  $\boldsymbol{\Phi} = [\boldsymbol{\phi}(1) \ \dots \ \boldsymbol{\phi}(K)]_{NM \times K}$ , and  $\mathbf{E} = [\mathbf{e}(1) \ \mathbf{e}(2) \ \dots \ \mathbf{e}(K)]_{NM \times K}$  is the additive noise.

## 5.2.2 Statistical Model

In (5.4), we assume that  $\mathbf{X}$  (target reflection coefficients) is an unknown deterministic. Moreover, in our analysis  $\mathbf{e}(k)$ , for  $k = 1, \dots, K$  are independent identically distributed (i.i.d.) zero-mean complex multivariate normal random vectors with  $\sigma_e^2 I_{MN \times MN}$  as covariance for unknown  $\sigma_e^2$ . Define  $\boldsymbol{\phi}(k) = \exp(\tilde{\boldsymbol{\theta}}(k))$  with  $\tilde{\boldsymbol{\theta}}(k) = [\tilde{\theta}_{11}(k), \tilde{\theta}_{21}(k), \dots, \tilde{\theta}_{NM}(k)]$  (see also (5.3)), where  $\tilde{\theta}_{nm}(k)$  is the phase error between the  $n^{\text{th}}$  receiver and  $m^{\text{th}}$  transmitter pair at the  $k^{\text{th}}$  pulse. Then,  $\boldsymbol{\Theta} = [\tilde{\boldsymbol{\theta}}(1) \ \dots \ \tilde{\boldsymbol{\theta}}(K)]$ . We model  $\tilde{\theta}_{nm}(k)$  as i.i.d. von-Mises distributed random variables following [66] (recall that the output of a PLL is shown to follow von-Mises distribution [124], [125],

[126] ):

$$p(\tilde{\theta}_{nm}(k); \Delta) = \frac{\exp[\Delta \cos \tilde{\theta}_{nm}(k)]}{2\pi I_0(\Delta)} \quad -\pi \leq \tilde{\theta}_{nm}(k) \leq \pi, \quad (5.6)$$

where  $\Delta \geq 0$  is the (unknown) shape parameter and  $I_0(\cdot)$  is the modified Bessel function of the first kind and order zero;  $\Delta$  controls the spread of the density, reducing the density to uniform distribution when  $\Delta = 0$  [66].

For each pulse, at each receiver, we assume that the signals from  $M$  transmitters are processed through  $M$  different channels and independent PLLs. Hence the outputs of the PLLs are independent from each other, which justifies the independence of  $\tilde{\theta}_{n1}(k), \tilde{\theta}_{n2}(k), \dots, \tilde{\theta}_{nM}(k)$ . Also since the receivers are widely separated from each other, we assume that the PLLs are independent from receiver to receiver, which justifies the independence of  $\tilde{\theta}_{1m}(k), \tilde{\theta}_{2m}(k), \dots, \tilde{\theta}_{Nm}(k)$ . After receiving each pulse, the matched-filtering and PLL tracking is repeated at each receiver; therefore, there might be time correlation between the successive outputs of the each PLL ( $\tilde{\theta}_{nm}(k), \tilde{\theta}_{nm}(k+1)$ ). However, due to the narrow-band signal assumption, the time correlation can be ignored, which justifies the pulse-to-pulse independence.

Observe that conditioned on  $\Theta$ , with known  $\mathbf{A}$  and unknown  $\mathbf{X}$  and  $\sigma_e^2$ , we get a GMANOVA model for (5.5) with the following distribution:

$$\prod_{k=1}^K p(\mathbf{y}(k) | \tilde{\boldsymbol{\theta}}(k); \mathbf{X}, \sigma_e^2) = \prod_{k=1}^K \frac{1}{|\pi \sigma_e^2 \mathbf{I}|} \exp \left\{ \frac{-1}{\sigma_e^2} [\mathbf{y}(k) - \mathbf{A} \mathbf{X} \boldsymbol{\phi}(k)]^H [\mathbf{y}(k) - \mathbf{A} \mathbf{X} \boldsymbol{\phi}(k)] \right\}. \quad (5.7)$$



### 5.3 Detection and Estimation Algorithm

We derive the GLRT using the observed data likelihood function, with  $\mathbf{Y}$  as the observed and  $\tilde{\boldsymbol{\theta}}(k)$ ,  $k = 1, \dots, K$  as the unobserved data to decide about the presence of a target in the COI. Specifically, we choose between two hypotheses in the following parametric test:

$$\begin{cases} \mathcal{H}_0 & : & \mathbf{X} = 0, \sigma_e^2 \\ \mathcal{H}_1 & : & \mathbf{X} \neq 0, \sigma_e^2, \Delta \end{cases}, \quad (5.8)$$

with  $\sigma_e^2$  and  $\Delta$  as the nuisance parameters. We compute the GLRT and reject  $\mathcal{H}_0$  (target-free case) in favor of  $\mathcal{H}_1$  (target-present case) when

$$\text{GLRT} = \frac{p_1(\mathbf{Y}; \hat{\mathbf{X}}, \hat{\sigma}_{e1}^2, \hat{\Delta})}{p_0(\mathbf{Y}; \hat{\sigma}_{e0}^2)} > \eta, \quad (5.9)$$

where  $p_i(\cdot)$  and  $\hat{\sigma}_{ei}^2$  are the observed data likelihood function and the maximum-likelihood estimate (MLE) of  $\sigma_e^2$  under  $\mathcal{H}_i$  for  $i = 0, 1$ , respectively; where  $\hat{\mathbf{X}}$  and  $\hat{\Delta}$  are the MLEs of  $\mathbf{X}$  and  $\Delta$  under  $\mathcal{H}_1$ ; and where  $\eta$  is the detection threshold.

Under the given statistical assumptions in section 5.2.2, there is no closed-form solution for the MLEs of  $\mathbf{X}$ ,  $\sigma_e^2$ , and  $\Delta$  (see also (5.16) for the observed data probability density function). Therefore, we compute the MLEs of the unknown parameters using an EM algorithm with the hierarchical data model presented in (5.6) and (5.7). We define  $\mathbf{Y}$ ,  $\boldsymbol{\Theta}$ , and  $(\mathbf{Y}, \boldsymbol{\Theta})$  as the observed, unobserved, and complete data, respectively. First, we write the complete data log-likelihood function in canonical

exponential family form [116]:

$$\begin{aligned}
L_c(\mathbf{X}, \sigma_e^2, \Delta) &= \ln p(\mathbf{Y}, \Theta; \mathbf{X}, \sigma_e^2, \Delta) \\
&= \ln \prod_{k=1}^K p(\mathbf{y}(k) | \tilde{\boldsymbol{\theta}}(k); \mathbf{X}, \sigma_e^2) p(\tilde{\boldsymbol{\theta}}(k); \Delta) \\
&= \text{const} + \frac{-K}{\sigma_e^2} (\text{tr}[\mathbf{X}^H \mathbf{A}^H \mathbf{A} \mathbf{X} \mathbf{T}_3] \\
&\quad + \text{tr}[\mathbf{T}_2] - 2\text{Re}(\text{tr}[\mathbf{T}_1^H \mathbf{A} \mathbf{X}])) \\
&\quad - NMK \ln I_0(\Delta) + \Delta T_4,
\end{aligned} \tag{5.10}$$

where  $\mathbf{T}_i$ ,  $i = 1, 2, 3$  and  $T_4$  are the natural complete-data sufficient statistics (see (5.11) for the definitions) and “tr” stands for the trace. Since the complete-data likelihood function belongs to an exponential family, we simplify the EM algorithm [116]. In E step, we first calculate the conditional expectation of the natural complete-data sufficient statistics given the observed data (using  $p(\Theta | \mathbf{Y}; \mathbf{X}, \sigma_e^2, \Delta)$ ). Then, in the M step, in the MLE expressions, we simply replace the natural complete-data sufficient statistics with the ones obtained in the E step.

**E Step:** We define the  $i^{\text{th}}$  iteration estimates of the set of the unknown parameters as  $\Gamma^{(i)} = \{\hat{\mathbf{X}}^{(i)}, (\hat{\sigma}_e^2)^{(i)}, \hat{\Delta}^{(i)}\}$  and compute the conditional expectation  $[\mathbb{E}_{p(\Theta | \mathbf{Y})}(\cdot)]$  expectation w.r.t.  $p(\Theta | \mathbf{Y}; \mathbf{X}, \sigma_e^2, \Delta)$  of the sufficient statistics under  $\mathcal{H}_1$ :

$$\mathbf{T}_1^{(i)} = \mathbb{E}_{p(\Theta | \mathbf{Y})} \left( \frac{1}{K} \sum_{k=1}^K \mathbf{y}(k) \boldsymbol{\phi}(k)^H; \Gamma^{(i)} \right), \tag{5.11a}$$

$$\mathbf{T}_2^{(i)} = \frac{1}{K} \sum_{k=1}^K \mathbf{y}(k) \mathbf{y}(k)^H, \tag{5.11b}$$

$$\mathbf{T}_3^{(i)} = \mathbb{E}_{p(\Theta | \mathbf{Y})} \left( \frac{1}{K} \sum_{k=1}^K \boldsymbol{\phi}(k) \boldsymbol{\phi}(k)^H; \Gamma^{(i)} \right), \tag{5.11c}$$

$$T_4^{(i)} = \mathbb{E}_{p(\Theta | \mathbf{Y})} \left( \sum_{k=1}^K \sum_{n=1}^N \sum_{m=1}^M \cos(\tilde{\theta}_{nm}(k)); \Gamma^{(i)} \right). \tag{5.11d}$$

**M Step:** We simply replace the natural complete-data sufficient statistics with their conditional expectations from (5.11) in the MLE expressions. We apply the results of GMANOVA [113] for the MLEs of  $\mathbf{X}$  and  $\sigma_e^2$  (for the MLE of  $\sigma_e^2$ ; these results have been improved to fit in our case). We define  $\mathbf{S}^{(i)} = \mathbf{T}_2^{(i)} - \mathbf{T}_1^{(i)} \left(\mathbf{T}_3^{(i)}\right)^{-1} \left(\mathbf{T}_1^{(i)}\right)^H$  and  $P = NMK$ , then compute

$$\hat{\mathbf{X}}^{(i+1)} = \left[ \mathbf{A}^H \left(\mathbf{S}^{(i)}\right)^{-1} \mathbf{A} \right]^{-1} \mathbf{A}^H \cdot \left(\mathbf{S}^{(i)}\right)^{-1} \mathbf{T}_1^{(i)} \left(\mathbf{T}_3^{(i)}\right)^{-1} \quad (5.12a)$$

$$\begin{aligned} (\hat{\sigma}_e^2)^{(i+1)} = & \frac{1}{P} \left( \text{tr}[\mathbf{T}_2^{(i)}] - 2\text{Re}(\text{tr}[(\mathbf{T}_1^H)^{(i)} \mathbf{A} \mathbf{X}^{(i+1)}]) \right. \\ & \left. + \text{tr}[(\mathbf{X}^H)^{(i+1)} \mathbf{A}^H \mathbf{A} \mathbf{X}^{(i+1)}] \right) \end{aligned} \quad (5.12b)$$

Concentrating (5.10) w.r.t.  $\hat{\mathbf{X}}^{(i+1)}$  and  $(\hat{\sigma}_e^2)^{(i+1)}$ , we compute

$$\hat{\Delta}^{(i+1)} = \arg \max_{\Delta} -P \ln I_0(\Delta) + \Delta T_4^{(i)}. \quad (5.13)$$

Under  $\mathcal{H}_0$ ,  $p_0(\mathbf{Y}; \hat{\sigma}_e^2)$  is Gaussian distributed and hence the only unknown  $\hat{\sigma}_e^2 = \text{tr}(\mathbf{T}_2)$ .

The above iteration is performed until  $\hat{\mathbf{X}}^{(i)}$ ,  $(\hat{\sigma}_e^2)^{(i)}$ , and  $\hat{\Delta}^{(i)}$  converge. The computation of  $\hat{\Delta}^{(i+1)}$  is achieved by maximizing (5.13) using the Newton-Raphson method embedded within the “outer” EM iteration, similar to [129], [111]. We assume that the shape parameter of the phase error does not change in the processing time interval, therefore after the initial estimation, this estimate can be used in the successive radar dwells. The estimation of the shape parameter could also be achieved during a calibration process, and hence the estimation step (5.13) can be eliminated from the iterations of the EM algorithm. This elimination increases the processing speed; however, the performance of the system may change under possible modeling errors.

We provide numerical examples in Section 5.5 to compare the performances of the GLRT detector under known and unknown  $\Delta$  assumptions. We also consider possible modeling errors in the detector and illustrate the sensitivity of the system to changes in the shape parameter.

Recalling the assumptions from Sec. 5.2.2, we compute the conditional distribution,  $p(\Theta|\mathbf{Y}; \mathbf{X}, \sigma_e^2, \Delta) = \prod_{k=1}^K p(\tilde{\boldsymbol{\theta}}(k)|\mathbf{y}(k); \mathbf{X}, \sigma_e^2, \Delta)$ .

First, to obtain the marginal distribution

$$p(\mathbf{y}(k); \mathbf{X}, \sigma_e^2, \Delta) = \int_{-\pi}^{\pi} \cdots \int_{-\pi}^{\pi} p(\mathbf{y}(k)|\tilde{\boldsymbol{\theta}}(k))p(\tilde{\boldsymbol{\theta}}(k))d\tilde{\boldsymbol{\theta}}(k), \quad (5.14)$$

we employ

$$\int_{-\pi}^{\pi} \exp(a \cos \tilde{\theta} + b \sin \tilde{\theta})d\tilde{\theta} = 2\pi I_0(\sqrt{a^2 + b^2}) \quad (5.15)$$

for any complex  $a$  and  $b$  (see Appendix D for the proof of the identity in (5.15)); then

$$p(\mathbf{y}(k); \mathbf{X}, \sigma_e^2, \Delta) = \frac{\exp(\frac{-1}{\sigma_e^2}(\mathbf{y}(k)^H \mathbf{y}(k) + h))}{(\sigma_e^2 \pi)^{NM}} \prod_{m=1}^M \prod_{n=1}^N \frac{I_0(c_{nm}(k))}{I_0(\Delta)}, \quad (5.16)$$

where

- $h = \mathbf{1}^T \mathbf{X}^H \mathbf{A}^H \mathbf{A} \mathbf{X} \mathbf{1}$ , and  $\mathbf{1}$  is an  $NM \times 1$  vector of ones
- $c_{nm}(k) = \sqrt{a_{nm}(k)^2 + b_{nm}(k)^2}$
- $a_{nm}(k) = \frac{2}{\sigma_e^2} \text{Re}\{r_{nm}^*(k) \alpha_{nm} \beta_m e^{-j\psi_{nm} \sigma_{nm}}\} + \Delta$
- $b_{nm}(k) = \frac{2}{\sigma_e^2} \text{Im}\{r_{nm}^*(k) \alpha_{nm} \beta_m e^{-j\psi_{nm} \sigma_{nm}}\}$
- $r_{nm}^*(k)$  is the complex conjugate of the  $(N(m-1) + n)^{th}$  entry of  $\mathbf{y}(k)$
- $\alpha_{nm} \beta_m e^{-j\psi_{nm}}$  is the  $(N(m-1) + n)^{th}$  diagonal entry of  $\mathbf{A}$ , and

- $\sigma_{nm}$  is the  $(N(m-1) + n)^{th}$  diagonal entry of  $\mathbf{X}$  (see (5.4) and (5.5)).

Then, using (5.6), (5.7), and (5.16), we find the conditional distribution

$$p(\tilde{\boldsymbol{\theta}}(k)|\mathbf{y}(k); \mathbf{X}, \sigma_e^2, \Delta) = \prod_{m=1}^M \prod_{n=1}^N \frac{\exp(d_{nm}(k))}{2\pi I_0(c_{nm}(k))}, \quad (5.17)$$

where  $d_{nm}(k) = a_{nm}(k) \cos \tilde{\theta}_{nm}(k) + b_{nm}(k) \sin \tilde{\theta}_{nm}(k)$ .

We compute the conditional mean of the natural complete-data sufficient statistics in (5.11) using (5.17). We apply

$$\int_{-\pi}^{\pi} e^{\pm j\tilde{\theta}} \exp(a \cos \tilde{\theta} + b \sin \tilde{\theta}) d\tilde{\theta} = 2\pi \frac{a \pm jb}{\sqrt{a^2 + b^2}} I_1(\sqrt{a^2 + b^2}) \quad (5.18)$$

for any complex  $a$  and  $b$  where  $I_1(\cdot)$  is the modified Bessel function of the first kind with order one. We provide a proof of the identity in (5.18) in Appendix E. Then we obtain

$$\mathbb{E}_{p(\boldsymbol{\Theta}|\mathbf{Y})}(e^{\pm j\tilde{\theta}_{nm}(k)}) = \frac{a_{nm}(k) \pm jb_{nm}(k)}{c_{nm}(k)} \frac{I_1(c_{nm}(k))}{I_0(c_{nm}(k))}. \quad (5.19)$$

We denote  $\hat{\mathbf{X}}$ ,  $\hat{\sigma}_e^2$ , and  $\hat{\Delta}$  as the estimates of  $\mathbf{X}$ ,  $\sigma_e^2$ , and  $\Delta$  obtained upon the convergence of the EM algorithm under  $\mathcal{H}_1$ , and using (5.9), (5.12), (5.13), and (5.16), we obtain

$$(\text{GLRT})^{\frac{1}{P}} = \frac{\exp(\frac{-1}{NM\hat{\sigma}_e^2}(\text{tr}(\mathbf{T}_2) + h)) \text{tr}(\mathbf{T}_2)}{\exp(-1)} \frac{g^{\frac{1}{P}}}{\hat{\sigma}_e^2 I_0(\hat{\Delta})}, \quad (5.20)$$

where  $g = \prod_{k=1}^K \prod_{m=1}^M \prod_{n=1}^N I_0(c_{nm}(k))$ .

## 5.4 Adaptive Design

In this section, we compute an upper bound on the mutual information (MI) between the received target responses ( $\mathbf{A}\mathbf{X}\Phi$  in (5.5)) and the radar measurements [69]. Then we use this upper bound as a utility function for adaptive allocation of the total transmitted energy among the transmitters, exploiting the RCS sensitivity of the system. We determine the optimum transmitted energy by each transmitter according to this utility function. We show the effect of the optimum energy allocation on detection performance in Section 5.5.

Given the statistical assumptions in Section 5.2.2 and (5.5), the MI between the received target responses and the radar measurements is equal to the MI between the phase error and the radar measurements. Then, recalling (5.7), (5.14), and the statistical assumptions from Section 5.2.2, we compute the MI,  $I(\Theta; \mathbf{Y})$ , between the phase error ( $\Theta$ ) and the radar measurements ( $\mathbf{Y}$ ):

$$I(\Theta; \mathbf{Y}) = E_{p(\mathbf{Y}, \Theta)} \left( \log \frac{p(\mathbf{Y} | \Theta; \mathbf{X}, \sigma_e^2)}{p(\mathbf{Y}; \mathbf{X}, \sigma_e^2, \Delta)} \right), \quad (5.21)$$

where

- $p(\mathbf{Y}, \Theta; \mathbf{X}, \sigma_e^2, \Delta) = \prod_{k=1}^K p(\mathbf{y}(k), \tilde{\theta}(k); \mathbf{X}, \sigma_e^2, \Delta)$  is the complete data likelihood function
- $p(\mathbf{Y} | \Theta; \mathbf{X}, \sigma_e^2) = \prod_{k=1}^K p(\mathbf{y}(k) | \tilde{\theta}(k); \mathbf{X}, \sigma_e^2)$ , and
- $p(\mathbf{Y}; \mathbf{X}, \sigma_e^2, \Delta) = \prod_{k=1}^K p(\mathbf{y}(k); \mathbf{X}, \sigma_e^2, \Delta)$ .

Since an increase in the MI between  $\mathbf{Y}$  and  $\Theta$  corresponds to an increase in information about the received target returns, we expect to see an increase in the detection

performance as the MI between  $\mathbf{Y}$  and  $\Theta$  increases (see the results in [31, Chapter 10] explaining the relationship between the MI and the probability of detection). Therefore, for the adaptive energy allocation scheme, we form a utility function that depends on the mutual information and maximize it with respect to the the energy parameters,  $\beta_m$ ,  $m = 1, \dots, M$  (see (5.1)).

Since a closed-form solution does not exist, we compute an upper bound on the MI between  $\mathbf{Y}$  and  $\Theta$  for the optimization problem. Recall that the noise and the phase error are independent from pulse to pulse (see Section 5.2.2); then  $I(\Theta; \mathbf{Y}) = \sum_{k=1}^K I(\tilde{\theta}(k); \mathbf{y}(k)) = KI(\tilde{\theta}(1); \mathbf{y}(1))$  (MI for every pulse is equal). Hence we focus on mutual information for a single pulse (we drop the  $k$  dependency to simplify the notation).

**Theorem 5.1.** *The mutual information between the phase error (and hence the received target responses) and the radar measurements modeled in (5.4) is bounded by*

$$I(\tilde{\theta}; \mathbf{y}) \leq \sum_{m=1}^M \log \left( \prod_{n=1}^N \left[ 1 + \frac{\beta_m^2 \alpha_{nm}^2 \sigma_{nm}^2}{\sigma_e^2} \right] \right), \quad (5.22)$$

where

- $M$ ,  $N$ ,  $\beta_m$ ,  $\alpha_{nm}$ , and  $\sigma_{nm}$  are as defined in (5.1), and
- $\sigma_e^2$  is as defined in Section 5.2.2.

*Proof.* See Appendix F.

In order to optimize the upper bound in (5.22), we define  $\xi_{nm}^2 = \alpha_{nm}^2 \sigma_{nm}^2$  and rewrite it as

$$\sum_{m=1}^M \log \left( \prod_{n=1}^N \left[ 1 + \frac{\beta_m^2 \xi_{nm}^2}{\sigma_e^2} \right] \right) = \sum_{m=1}^M \log \left( 1 + \frac{q_m^2}{\sigma_e^2} \right), \quad (5.23)$$

where  $q_m^2$  is obtained after algebraic manipulation of (5.22):

$$\begin{aligned}
q_m^2 &= \beta_m^2 \sum_{n=1}^N \xi_{nm}^2 + \frac{\beta_m^4 \left( \sum_{n_1=1}^{N-1} \xi_{n_1 m}^2 \sum_{n_2=n_1+1}^N \xi_{n_2 m}^2 \right)}{\sigma_e^2} + \dots \\
&+ \frac{\beta_m^{2N-2} \left( \sum_{n_1=1}^{N-(N-2)} \xi_{n_1 m}^2 \sum_{n_2=n_1+1}^{N-(N-3)} \xi_{n_2 m}^2 \dots \sum_{n_{N-1}=n_{N-2}+1}^N \xi_{n_{N-1} m}^2 \right)}{\sigma_e^{2N-4}} \\
&+ \frac{\beta_m^{2N} \left( \prod_{n=1}^N \xi_{nm}^2 \right)}{\sigma_e^{2N-2}}. \tag{5.24}
\end{aligned}$$

We optimize the upper bound with respect to  $\mathbf{q} = [q_1, \dots, q_M]^T \succcurlyeq \mathbf{0}$ , where “ $\succcurlyeq$ ” is element-wise inequality. Since we assume  $\sum_{m=1}^M \beta_m^2 = E$ ,  $0 \leq \sigma_{nm}^2 \leq 1$ , and  $0 \leq \alpha_{nm}^2$  and since  $0 \leq \sigma_e^2$  are finite for  $n = 1, \dots, N$  and  $m = 1, \dots, M$ , we obtain a finite value  $p$  such that  $\sum_{m=1}^M q_m^2 \leq p$ . Then we write the optimization problem as

$$\begin{aligned}
&\text{maximize} && \sum_{m=1}^M \log \left( 1 + \frac{q_m^2}{\sigma_e^2} \right) \\
&\text{subject to} && \mathbf{q} \succcurlyeq \mathbf{0}, \quad \sum_{m=1}^M q_m^2 \leq p.
\end{aligned} \tag{5.25}$$

We apply a “water-filling” type of strategy, which is commonly encountered in information theory for power allocation to communication channels, to solve the problem of finding the unique maximizer [130]:

$$q_m^2 = (\nu - \sigma_e^2) \quad \text{Select } \nu \text{ s.t. } \sum_{m=1}^M \max(0, q_m^2) = p. \tag{5.26}$$

Since  $\sigma_e^2$  is the same for all the summands of the objective function in (5.25), then from (5.26) the optimum solution is  $q_1 = \dots = q_M$  and  $\sum_{m=1}^M \beta_m^2 = E$ . In Appendix G, we provide a solution for  $M = 2$  and  $N = 2, 4$ . In practice, since we do not know



the target reflection coefficients  $\mathbf{X}$  and the noise variance  $\sigma_e^2$ , we replace them with their estimates. Once there is a detection at one radar dwell, before continuing with the next dwell, we apply the adaptive energy allocation algorithm that we propose. We use the estimates of  $\mathbf{X}$ ,  $\sigma_e^2$  and  $\Delta$  (estimates obtained in the current dwell), and obtain new power distribution among the transmitters to use in the next dwell. As we demonstrate in Section 5.5, if the next dwell contains detection, this detection will be with a higher probability.

## 5.5 Numerical Examples

We demonstrate the performance of the GLRT detector with numerical examples using Monte Carlo (MC) simulations. First we consider an unknown shape parameter  $\Delta$  for the phase error distribution, and we compute the receiver operating characteristics (ROC) of the GLRT detector. We then assume that the system is calibrated beforehand and so  $\Delta$  is known. We compare the ROC of the GLRT detector under the unknown and known  $\Delta$  assumptions. We apply the adaptive energy allocation algorithm under these two assumptions and demonstrate the improvement in the ROC curves. We consider possible modeling errors and show our results on the sensitivity of the GLRT detector to the changes in the shape parameter  $\Delta$ . Finally, to demonstrate the advantages of employing phase information (realistic modeling), we compare the GLRT detector that we propose with a coherent MIMO radar detector that ignores the phase error.

The results are obtained from  $10^4$  MC runs. We assume that  $M$  transmitters and  $N$  receivers (denoting MIMO  $M \times N$ ) are located on the y-axis and x-axis, respectively. The target is 10km from each axis. The antenna gains ( $G_{Tx}$  and  $G_{Rx}$ ) are 30dB;

the signal frequency ( $f_c$ ) is 1GHz. The angle between the transmitters  $\mu_1 = \dots = \mu_M = 10^\circ$  and similarly between the receivers  $\delta_1 = \dots = \delta_N = 10^\circ$  (see Fig. 5.2). We choose  $M = 2$ ,  $K = 25$  pulses for each transmitted signal throughout the numerical examples.

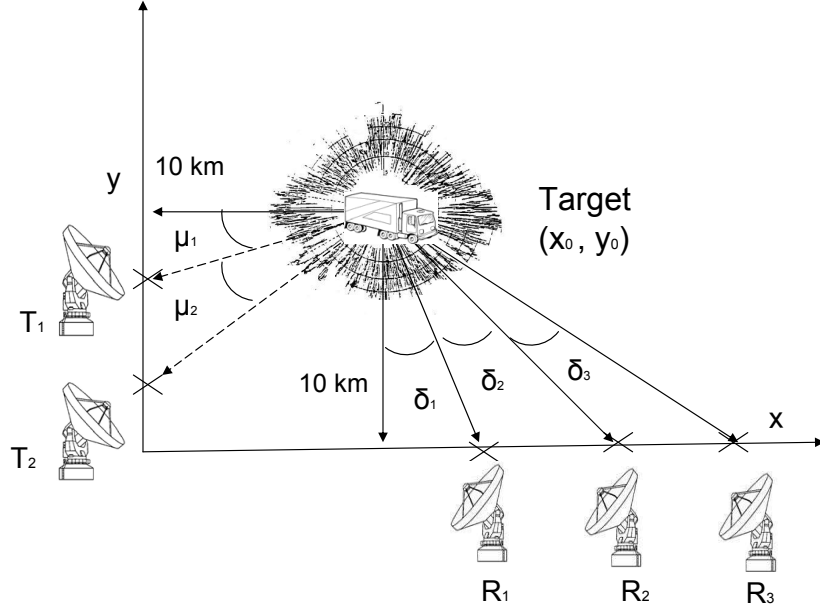


Figure 5.2: MIMO antenna system with  $M = 2$  transmitters and  $N = 3$  receivers.

We define signal-to-noise ratio (SNR) in a similar fashion to its definition in [111]

$$\text{SNR} = \sum_{k=1}^K (\mathbf{A}\mathbf{X}\mathbf{1})^H (\mathbf{A}\mathbf{X}\mathbf{1}) / (NMK\sigma_e^2) \quad (5.27)$$

The RCS values,  $\mathbf{X}$ , are assigned as the realizations of a zero-mean Gaussian random variable with unit variance for the simulation purposes. Later,  $\sigma_e^2$  is chosen to meet the desired SNR.

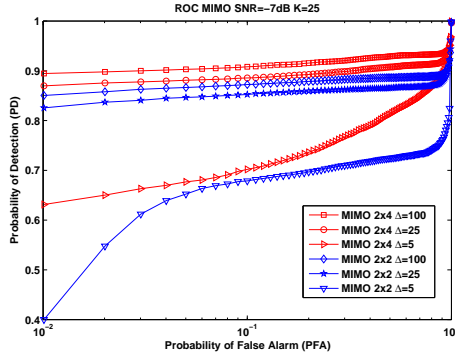


Figure 5.3: Receiver operating characteristics of MIMO radar for different number of receivers and shape parameter values, unknown shape parameter  $\Delta$ .

To obtain Figs. 5.3 and 5.4, we assume an unknown  $\Delta$ , and  $\text{SNR}=-7\text{dB}$ . In Fig. 5.3, we plot the receiver operating characteristics (ROC) of the MIMO radar detection in the presence of a phase error for a different number of receivers,  $N$ , and for different shape parameter (of the von-Mises distribution),  $\Delta$ , values. As expected when  $N$  increases, the performance of the MIMO system improves. We also observe that as  $\Delta$  increases, detection performance increases. We believe that the change in performance is due to the change in the entropy of the von-Mises distributed phase error. For a von-Mises distributed random variable  $\tilde{\theta}$  with a shape parameter  $\Delta$ , the entropy ( $h(\tilde{\theta})$ ) is calculated by

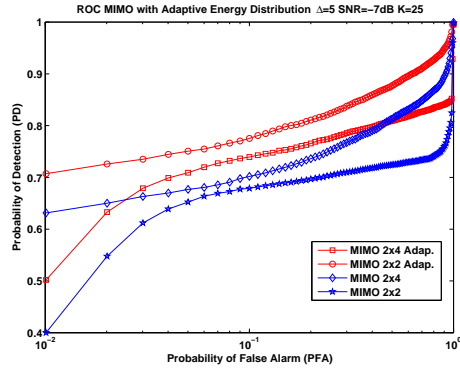
$$\begin{aligned}
 h(\tilde{\theta}) &= - \int_{-\pi}^{\pi} p(\tilde{\theta}; \Delta) \ln(p(\tilde{\theta}; \Delta)) d\tilde{\theta} \\
 &= \ln(2\pi I_0(\Delta)) - \Delta \frac{I_1(\Delta)}{I_0(\Delta)},
 \end{aligned} \tag{5.28}$$

where  $p(\tilde{\theta}; \Delta)$  is as defined in (5.6). The equation (5.28) is a decreasing function of  $\Delta$ . When  $\Delta = 0$ , it has the maximum entropy (maximum uncertainty, minimum performance); as  $\Delta$  increases, this entropy decreases, giving rise to an increase in the detection performance [66].

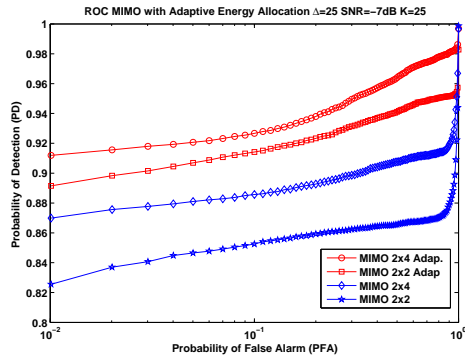
In Fig. 5.4, we demonstrate improvement in detection performance due to the adaptive energy allocation for different  $N$  and  $\Delta$  values. We compute the receiver operating characteristics for MIMO radar when the total energy ( $E$ ) is equally divided among the transmitters (MIMO  $M \times N$  on the figure) and subsequently when  $E$  is adaptively distributed among the transmitters using our algorithm (MIMO  $M \times N$  Adap. on the figure). We observe that our adaptive algorithm improves the detection performance. The adaptive method optimally allocates the total energy to transmitters depending on the target RCS values and noise variance such that the mutual information between the phase error and the radar measurements increases. This increase corresponds to an increase in the information about the received target responses; hence, there is improvement in detection performance.

In Figs. 5.5, 5.6, 5.7, and 5.8, we assume that the calibration was achieved beforehand, and hence  $\Delta$  is known. In Figs. 5.5, 5.6 and 5.8, SNR=-7dB. The known  $\Delta$  assumption increases the speed of the algorithm (because there is no Newton-Raphson step within the outer EM algorithm), and also improves the detection performance of the system. Comparing Figs. 5.3 and 5.5, one can observe improvement in the ROC curves. Moreover, in Fig. 5.5, we illustrate the performance of the GLRT detector for the extreme cases of  $\Delta$ . As  $\Delta \rightarrow \infty$ , the uncertainty in the phase error decreases, and the detector that we propose converges to the coherent MIMO radar detector (as  $\Delta \rightarrow \infty$ , there is no phase error in the measurements). The coherent MIMO radar detector under no phase error sets an upper bound for the detection performance. On the other hand, as  $\Delta \rightarrow 0$ , a small decrement in  $\Delta$  causes a larger decrease in the performance of the GLRT detector.

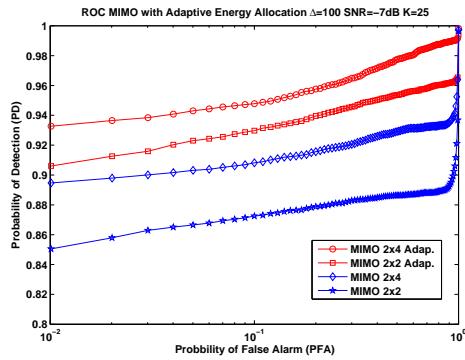
In Fig. 5.6, we apply the adaptive energy allocation algorithm and obtain further improvement in detection performance. The performance of the adaptively designed



(a)



(b)



(c)

Figure 5.4: Receiver operating characteristics of MIMO radar with and without adaptive energy allocation for (a)  $\Delta = 5$ ; (b)  $\Delta = 25$ ; (c)  $\Delta = 100$ , unknown shape parameter  $\Delta$ .

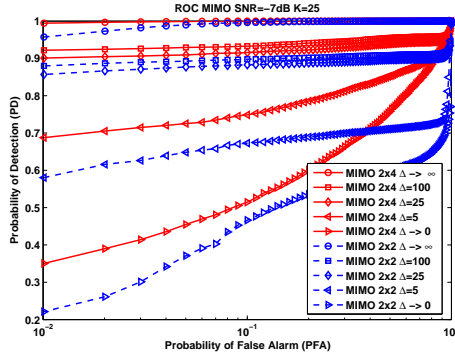
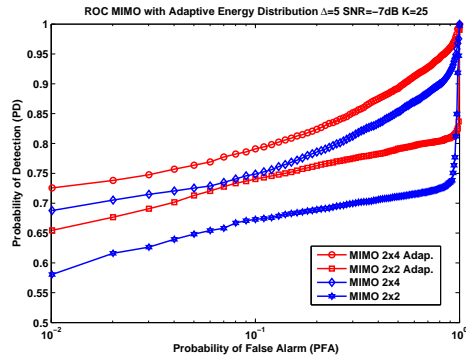


Figure 5.5: Receiver operating characteristics of MIMO radar for different number of receivers and shape parameter values, known shape parameter  $\Delta$ .

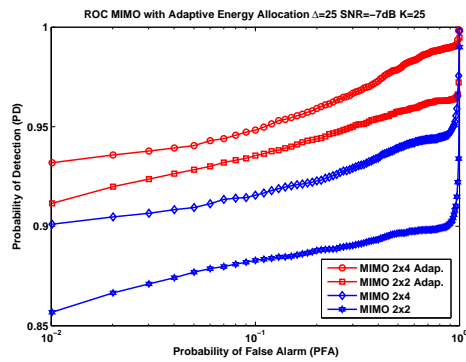
detector is better under the known  $\Delta$  assumption (see Fig. 5.4). In Fig. 5.7, to gain further insight into the system performance, we plot the probability of detection (PD) as a function of SNR for a fixed probability of false alarm (PFA =  $10^{-2}$ ). The outcome supports the results of Fig. 5.5, such that as both the number of the receivers and the value of the shape parameter  $\Delta$  increase, the PD also increases.

To demonstrate the improvement due to employing the phase error information, we compare the GLRT detector that we propose with a coherent MIMO radar detector that ignores the phase error. In Fig. 5.8, CMIMO  $M \times N \Delta = d$  refers to the coherent MIMO radar detector with  $M$  transmitters and  $N$  receivers, which ignores the phase error, and the phase error follows a von-Mises distribution with  $\Delta = d$ . The detector that we propose outperforms the coherent MIMO detector (the measurements include the phase error). Ignoring the phase error causes model mismatch, which deteriorates detection performance.

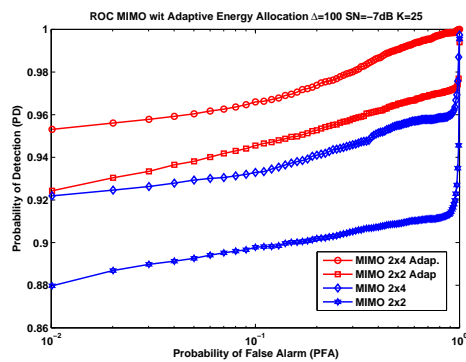
In Figs. 5.3 and 5.5, we compare the performances of the GLRT detector under both the unknown and the known shape parameter  $\Delta$  assumptions. We illustrate the improvement in the system performance for the known  $\Delta$  assumption. We assume



(a)



(b)



(c)

Figure 5.6: Receiver operating characteristics of MIMO radar with and without adaptive energy allocation for (a)  $\Delta = 5$ ; (b)  $\Delta = 25$ ; (c)  $\Delta = 100$ , and known shape parameter  $\Delta$ .

that  $\Delta$  estimation is achieved beforehand during the calibration process. However, estimation errors may deteriorate detection performance. In Fig. 5.9, we demonstrate the sensitivity of the detector to the changes in the shape parameter  $\Delta$ . We consider the cases where  $\Delta$  is set high but has a smaller value in the real data. In the Fig 5.9,  $\Delta_r$  and  $\Delta_s$  correspond, respectively, to the real and assumed (set) values of the shape parameter. That is, the real data has a phase error with a shape parameter  $\Delta_r$ , but the detector assumes this parameter is known and has the value  $\Delta_s$ . For  $\Delta_s = 100$ , we plot  $\Delta_r = 5, 10, 25$ , and we demonstrate that as the  $\Delta_r$  value goes below 10, the change in the detection performance is significant. However, for  $\Delta_r$  values larger than 10, the detector is more robust to the phase modeling errors.

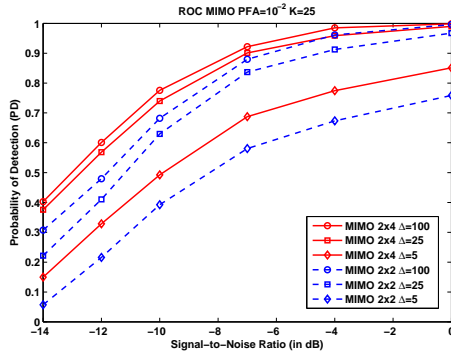


Figure 5.7: Probability of detection vs. signal-to-noise ratio for a fixed  $PFA=10^{-2}$ , and known shape parameter  $\Delta$ .

## 5.6 Summary

We developed a GLRT target detector for a MIMO radar system with widely separated antennas in the presence of a phase synchronization error. Using a von-Mises distribution to represent the phase error terms, we introduced a measurement model



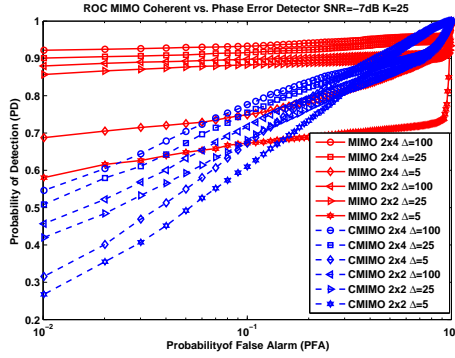


Figure 5.8: Comparison of the receiver operating characteristics of the coherent MIMO radar and MIMO radar phase error (GLRT) detectors, for known shape parameter  $\Delta$ .

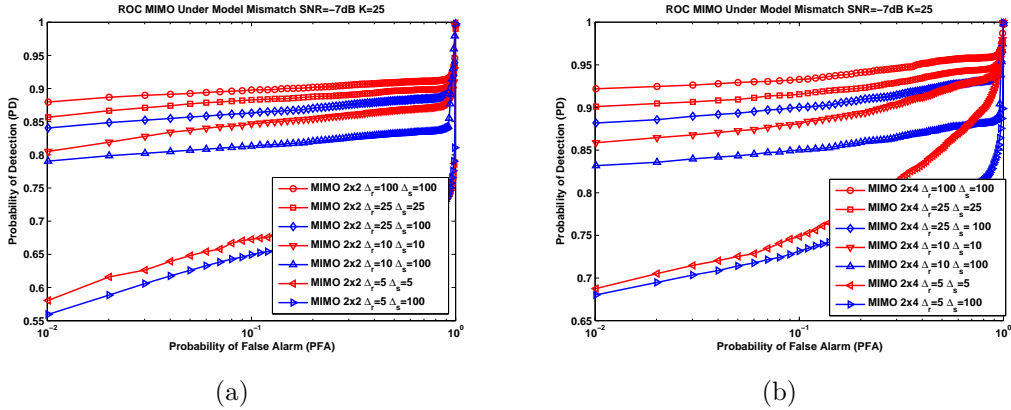


Figure 5.9: Receiver operating characteristics of MIMO radar under model mismatch (a) MIMO  $2 \times 2$  (b) MIMO  $2 \times 4$ .

under the GMANOVA framework and applied the EM algorithm to estimate the unknown parameters. We developed the GLRT detector using these estimates. In addition, we computed an upper bound on the mutual information between the radar measurements and the phase error, and we used the upper bound to propose an adaptive energy allocation algorithm that employs the RCS sensitivity of the system. Then, we solved the optimization problem analytically using a water-filling type strategy. We studied the GLRT detector under unknown and known shape

parameter assumptions. With different shape parameters, we modeled different uncertainties in the phase error distribution and demonstrated their effect on detection performance using Monte Carlo simulations. We considered the error in the modeling of the phase error in the detector, and we analyzed the sensitivity of the GLRT detector to changes in the phase error shape parameter. Comparing the GLRT detector, which we propose, with a coherent MIMO radar detector, we showed an improvement in detection performance due to employing the phase error information. We also illustrated the detection performance enhancement using our adaptive energy distribution algorithm.

# Chapter 6

## MIMO Radar Sensitivity Analysis for Target Detection<sup>6</sup>

For MIMO radar processing, in practice, mutual orthogonality among the received signals cannot be achieved for all delay and Doppler pairs. In this chapter, we address the effect of the imperfect orthogonality of the received signals on the detection performance. We introduce a data model considering the correlation terms among the received data as deterministic unknown. Using this model, we develop an algorithm to estimate the target, correlation, and noise parameters, and then we use these estimates to formulate a Wald target detection test. Next we compute the Cramér-Rao bound (CRB) on the error of parameter estimation, and using the CRB results, we analyze the asymptotic statistical characteristics of the Wald test. Using Monte Carlo simulations and theoretical results, we analyze the changes in the performance of the target detection for different cross-correlation levels (CCLs) among the received signals, and hence demonstrate the sensitivity of the MIMO radar target detection to the imperfect separation of different transmitted signals at each receiver.

---

<sup>6</sup>Based on M. Akcakaya and A. Nehorai, “MIMO Radar Sensitivity Analysis for Target Detection” *IEEE Trans. Signal Process.*, in revision.

## 6.1 Introduction

Previous work on MIMO radar assumes signal transmission with insignificant cross-correlation to separate the transmitted waveforms from each other at each receiver [31, Chapters 8 and 9], [34]. However, for a MIMO radar, since the waveform separation is limited by the Doppler and time delay resolution [58] (see also [131], [132]), the absent or low cross-correlation of the waveform for any Doppler and time delay is not only important but also challenging. In our work, to realistically model the radar measurements, we also consider the non-zero cross-correlation among the signals received from different transmitters. We model these parameters as deterministic unknowns, and then we analyze the sensitivity of the MIMO radar target detection with respect to changes in the cross-correlation levels (CCLs) of the received signals. To the best of our knowledge, this issue has never been addressed before. We here show that an increase in the CCL decreases the detection performance. Moreover, we observe that radar systems with more receivers and/or transmitters have better detection performance, but such systems are more sensitive to changes in the CCL. Therefore, the performance analysis that was made under an assumption of no- or low-cross-correlation signal might be too optimistic. To simplify the analysis and better demonstrate our results, we focus on stationary target scenarios; however, we will extend our results to moving target detection in future work.

In the following, we demonstrate our analytical and numerical results on MIMO radar target detection in the presence of cross-correlation among the received signals using a Wald decision test [68], [112]. We demonstrate the sensitivity of the detection performance to changes in the CCL.

## 6.2 Radar Model

In this section, we develop measurement and statistical models for a MIMO radar system in the presence of non-zero cross-correlation among the transmitted waveforms. We use these models to develop a statistical decision test and obtain its asymptotical statistical characteristics.

### 6.2.1 Measurement Model

We consider a two dimensional (2D) spatial system with  $M$  transmitters and  $N$  receivers. We define  $(x_{\text{T}x_m}, y_{\text{T}x_m})$ ,  $m = 1, \dots, M$ , and  $(x_{\text{R}x_n}, y_{\text{R}x_n})$ ,  $n = 1, \dots, N$ , as the locations of the transmitters and receivers, respectively. We assume a stationary point target located at  $(x_0, y_0)$  and having RCS values changing w.r.t. the angle aspect (e.g., multiple scatterers, which cannot be resolved by the transmitted signals, with  $(x_0, y_0)$  as the center of gravity) [31]. Define the complex envelope of the narrow-band signal from the  $m^{\text{th}}$  transmitter as  $\beta_m s_m(t)$ ,  $m = 1, \dots, M$ , such that  $|\beta_m|^2$  is the transmitted energy with  $\sum_{m=1}^M |\beta_m|^2 = E$  ( $E$  is constant for any  $M$ ) and  $\int_{T_s} |s_m(t)|^2 dt = 1$ ,  $m = 1, \dots, M$ , with  $T_s$  as the signal duration. We write the complex envelope of the received signal at the  $n^{\text{th}}$  receiver as follows [31]:

$$r_n(t) = \sum_{m=1}^M \alpha_{nm} \xi_{nm} \beta_m s_m(t - \tau_{nm}) e^{-j\psi_{nm}} + e_n(t), \quad (6.1)$$

where

- $\xi_{nm}$  is the complex target reflection coefficient seen by the  $m^{\text{th}}$  transmitter and  $n^{\text{th}}$  receiver pair

- $\alpha_{nm} = \sqrt{\frac{G_{Tx}G_{Rx}\lambda^2}{(4\pi)^3 R_m^2 R_n^2}}$  is the channel parameter from the  $m^{th}$  transmitter to the  $n^{th}$  receiver, with  $G_{Tx}$  and  $G_{Rx}$  as the gains of the transmitting and receiving antennas, respectively;  $\lambda$  is the wavelength of the incoming signal; and  $R_m = \sqrt{(x_{Tx_m} - x_0)^2 + (y_{Tx_m} - y_0)^2}$  and  $R_n = \sqrt{(x_{Rx_n} - x_0)^2 + (y_{Rx_n} - y_0)^2}$  are the distances from transmitter and receiver to target, respectively
- $\tau_{nm} = (R_m + R_n)/c$ , and  $c$  is the speed of the signal propagation in the medium
- $\psi_{nm} = 2\pi f_c \tau_{nm}$ , with  $f_c$  as the carrier frequency, and
- $e(t)$  is additive measurement noise.

We will apply matched filtering to (6.1) and obtain the measurement at the  $n^{th}$  receiver corresponding to the  $i^{th}$  transmitter for a single pulse as

$$r_{ni} = \beta_i \alpha_{ni} \xi_{ni} e^{-j(\psi_{ni})} x_{ii}^n + \sum_{m=1, m \neq i}^M \beta_m \alpha_{nm} \xi_{nm} e^{-j(\psi_{nm})} x_{mi}^n + e_{ni}, \quad (6.2)$$

where

- $r_{ni} = \int_{\tau_{ni}}^{\tau_{ni}+T_s} r_n(t) s_i^*(t - \tau_{ni}) dt$
- $x_{ii}^n = \int_{\tau_{ni}}^{\tau_{ni}+T_s} s_i(t - \tau_{ni}) s_i^*(t - \tau_{ni}) dt$ , self correlation of the  $i^{th}$  signal
- $x_{mi}^n = \int_{\max(\tau_{ni}, \tau_{nm})}^{\min(\tau_{ni}, \tau_{nm})+T_s} s_m(t - \tau_{nm}) s_i^*(t - \tau_{ni}) dt$  is the cross-correlation between  $m^{th}$  and  $i^{th}$  signals at the  $n^{th}$  receiver, and
- $e_{ni} = \int_{\tau_{ni}}^{\tau_{ni}+T_s} e_n(t) s_i^*(t - \tau_{ni}) dt$ .

Note here that since perfect signal separation is not possible for all delay and Doppler values, unlike previous approaches, we do not ignore the cross-correlation terms  $x_{mi}^n$ .

Then, we collect the data at the  $n^{\text{th}}$  receiver corresponding to different transmitters for one pulse in an  $M \times 1$  column vector

$$\mathbf{r}_n = \mathbf{X}_n \tilde{\Phi}_n \boldsymbol{\xi}_n + \mathbf{e}_n, \quad (6.3)$$

where

- $\mathbf{r}_n = [r_{n1}, \dots, r_{nM}]^T$
- $[\mathbf{X}_n]_{mm'} = ([\mathbf{X}_n]_{m'm})^* = x_{m'm}^n$  for  $(\cdot)^*$  as the complex conjugate,  $m, m' = 1, \dots, M$  and  $m \neq m'$
- for  $m = m'$ ,  $[\mathbf{X}_n]_{mm} = x_{mm}^n$
- $\tilde{\Phi}_n = \text{diag}(\beta_1 \alpha_{n1} e^{-j(\psi_{n1})}, \dots, \beta_M \alpha_{nM} e^{-j(\psi_{nM})})$  is an  $M \times M$  diagonal matrix with  $mm^{\text{th}}$  entry as  $\beta_m \alpha_{nm} e^{-j(\psi_{nm})}$
- $\boldsymbol{\xi}_n = [\xi_{n1}, \dots, \xi_{nM}]^T$ , and
- $\mathbf{e}_n = [e_{n1}, \dots, e_{n2}]$ .

We stack the receiver outputs corresponding to all the signals into an  $NM \times 1$  vector:

$$\mathbf{y} = \mathbf{X} \tilde{\Phi} \boldsymbol{\xi} + \mathbf{e}, \quad (6.4)$$

where

- $\mathbf{y} = [\mathbf{r}_1^T, \dots, \mathbf{r}_N^T]^T$
- $\mathbf{X} = \text{blkdiag}(\mathbf{X}_1, \dots, \mathbf{X}_N)$  is an  $NM \times NM$  block diagonal matrix with  $\mathbf{X}_n$  as the  $n^{\text{th}}$  block diagonal entry

- $\tilde{\Phi} = \text{blkdiag}(\tilde{\Phi}_1, \dots, \tilde{\Phi}_N)$
- $\boldsymbol{\xi} = [\boldsymbol{\xi}_1^T, \dots, \boldsymbol{\xi}_N^T]^T$ , and
- $\mathbf{e} = [\mathbf{e}_1^T, \dots, \mathbf{e}_N^T]^T$ .

We assume that  $K$  pulses are transmitted from each transmitter; then

$$\mathbf{Y} = [\mathbf{y}(1) \ \mathbf{y}(2) \ \cdots \ \mathbf{y}(K)]_{NM \times K} = \mathbf{X} \tilde{\Phi} \boldsymbol{\Xi} + \mathbf{E}, \quad (6.5)$$

where  $\boldsymbol{\Xi} = [\boldsymbol{\xi}(1) \ \cdots \ \boldsymbol{\xi}(K)]_{NM \times K}$ , and  $\mathbf{E} = [\mathbf{e}(1) \ \mathbf{e}(2) \ \cdots \ \mathbf{e}(K)]_{NM \times K}$  is the additive noise.

## 6.2.2 Statistical Model

We now introduce our statistical assumptions for the measurement model. We assume, in (6.5),

- $\mathbf{X}$  is the  $NM \times NM$  matrix of the deterministic unknown correlation parameters
- $\boldsymbol{\xi}(k)$  is the  $NM \times 1$  vector of the complex Gaussian distributed target reflection coefficients,  $\mathbb{E}[\boldsymbol{\xi}(k)] = \mathbf{0}$ ,  $\mathbb{E}[\boldsymbol{\xi}(k)\boldsymbol{\xi}(k')^H] = \sigma_\xi^2 \mathbf{I} \delta_{kk'}$  and  $\mathbb{E}[\boldsymbol{\xi}(k)\boldsymbol{\xi}(k')^T] = \mathbf{0}$ , with  $\sigma_\xi^2$  as the unknown variance, and for  $k, k' = 1, \dots, K$   $\delta_{kk'} = 1$  when  $k = k'$ , and zero otherwise
- $\mathbf{e}(k)$  is the  $NM \times 1$  vector of the complex Gaussian distributed additive noise,  $\mathbb{E}[\mathbf{e}(k)] = \mathbf{0}$ ,  $\mathbb{E}[\mathbf{e}(k)\mathbf{e}(k')^H] = \sigma_e^2 \mathbf{I} \delta_{kk'}$  and  $\mathbb{E}[\mathbf{e}(k)\mathbf{e}(k')^T] = \mathbf{0}$ , such that  $\sigma_e^2$  is the unknown variance, and
- $\boldsymbol{\xi}(k)$  and  $\mathbf{e}(k')$  are uncorrelated for all  $k$  and  $k'$ .



To sum up, we consider the reflection coefficient variance  $\sigma_\xi^2$ , noise variance  $\sigma_e^2$ , and the correlation terms  $\mathbf{X}$  as the deterministic unknown parameters. We use the deterministic unknown parameter assumption for  $\mathbf{X}$  to demonstrate the sensitivity of the system to changes in the level of the cross-correlation values among the received signals. In practice, the matched-filter output is sampled at discrete delay values [114] (see also [32]), and we assume each range gate is represented by a single sample. However a target in one range gate, even though represented by a delay  $\tau$ , might actually be located at a delay  $\tilde{\tau}$  such that  $|\tau - \tilde{\tau}| \leq T_r$ , and  $cT_r$  is the range that can be resolved by the system. Therefore, even though we know the delay  $\tau$  that represents the range gate of interest, we assume we do not know the exact value of the matched-filter output (cross-correlation and self correlation terms). Hence we represent the correlation terms as deterministic unknowns. Note also that since multiple orthogonal signals are transmitted, the ambiguity in the matched-filter output is larger for a MIMO radar than a single antenna radar [58]. The increase in ambiguity for MIMO radar also justifies the deterministic unknown assumption for correlation terms.

Due to the distributed nature of the MIMO radar system, we assume that the target returns for different transmitter and receiver pairs are independent from each other. We also assume that the target returns for different pulses are independent realizations of the same random variable. Under these assumptions, we write the distribution of the data in (6.5) as

$$\prod_{k=1}^K p(\mathbf{y}(k); \sigma_\xi^2, \sigma_e^2, \mathbf{X}) = \prod_{k=1}^K \frac{1}{|\pi \Sigma|} \exp - (\mathbf{y}(k)^H \Sigma^{-1} \mathbf{y}(k)), \quad (6.6)$$

where

- $\Sigma = \text{blkdiag}(\Sigma_1, \dots, \Sigma_N)$ , and
- $\Sigma_n = \sigma_\xi^2 \mathbf{X}_n \tilde{\Phi}_n \tilde{\Phi}_n^H \mathbf{X}_n^H + \sigma_e^2 \mathbf{I}$ .

## 6.3 Statistical Decision Test for Target Detection

In this Section, we propose a Wald test for the detection of a target located in the range cell of interest (COI). This test depends on the maximum likelihood estimates (MLEs) of the unknown parameters as well as on the CRB on the estimation error under the alternative hypothesis. Therefore, we also develop a method for the estimation of the unknown parameters based on the expectation-maximization (EM) algorithm, then accordingly compute the CRB on the estimation error to derive the statistical test.

### 6.3.1 Wald Test

We choose between two hypotheses in the following parametric test:

$$\begin{cases} \mathcal{H}_0 : & \sigma_\xi^2 = 0, \mathbf{X}, \sigma_e^2 \\ \mathcal{H}_1 : & \sigma_\xi^2 \neq 0, \mathbf{X}, \sigma_e^2 \end{cases}, \quad (6.7)$$

where the correlation  $\mathbf{X}$  and the noise variance  $\sigma_e^2$  are the nuisance parameters. This is a composite hypothesis test, therefore a uniformly most powerful (UMP) test does not exist for the problem. As a sub-optimum approximation, a generalized likelihood ratio test (GLRT) is the most commonly used solution. Even though there is no optimality associated with the GLRT solution [68], it is known to work well in practice

[112], [133], [134], [135]. However, in (6.7), since the MLEs of the nuisance parameters cannot be obtained under  $\mathcal{H}_0$ , we do not use the GLRT; instead, we propose to use a Wald test. The Wald test depends only on the estimates of the unknown parameters under  $\mathcal{H}_1$ . Moreover, to demonstrate the results of our analysis, we focus on the asymptotic statistical characteristics of the decision test. Because the Wald test and GLRT were shown to have the same asymptotic performance [68], we choose a Wald test instead of the GLRT.

We define the set of unknown variables as  $\boldsymbol{\theta} = \{\sigma_\xi^2, \sigma_e^2, \mathbf{X}\}$ , and compute the Wald test as

$$T_w = (\hat{\sigma}_{\xi 1}^2 - \hat{\sigma}_{\xi 0}^2) \left( \left[ \mathbf{J}^{-1}(\hat{\boldsymbol{\theta}}_1) \right]_{\sigma_\xi^2 \sigma_\xi^2} \right)^{-1} (\hat{\sigma}_{\xi 1}^2 - \hat{\sigma}_{\xi 0}^2), \quad (6.8)$$

where

- $\hat{\sigma}_{\xi 1}^2$  and  $\hat{\sigma}_{\xi 0}^2$  are the estimates of  $\sigma_\xi^2$  under  $\mathcal{H}_1$  and  $\mathcal{H}_0$ , respectively ( $\hat{\sigma}_{\xi 0}^2 = 0$  under  $\mathcal{H}_0$ )
- $\mathbf{J}^{-1}(\hat{\boldsymbol{\theta}}_1)$  is the inverse of the Fisher information matrix (FIM) calculated at the estimate of  $\boldsymbol{\theta}$  under  $\mathcal{H}_1$ , and
- the subscript  $\sigma_\xi^2 \sigma_\xi^2$  of the inverse of the FIM is the value of the inverse FIM corresponding to  $\sigma_\xi^2$ , that is, the CRB on the  $\sigma_\xi^2$  estimation error.

We reject  $\mathcal{H}_0$  (the target-free case) in favor of  $\mathcal{H}_1$  (the target-present case) when  $T_w$  is greater than a preset threshold value.

### 6.3.2 Estimation Algorithm

The Wald test proposed in (6.8) requires estimation of the unknown parameters  $\boldsymbol{\theta}$  under the alternative hypothesis  $\mathcal{H}_1$ . Since the number of the measurements is the same as the number of the random reflections from the target, there is no closed-form solution to the estimates of unknown parameters, so we cannot use the concentrated likelihood methods proposed in [82], [97], [96], [83] to estimate  $\boldsymbol{\theta}$ . Instead we propose to develop an estimation method based on the EM algorithm.

We consider  $\mathbf{Y}$ ,  $\boldsymbol{\Xi}$ , and  $(\mathbf{Y}, \boldsymbol{\Xi})$  as the observed, unobserved, and complete data, respectively. Then, we rewrite the distribution of the observed data in (6.6) as a hierarchical data model:

$$\begin{aligned}
 p(\mathbf{Y}|\boldsymbol{\Xi}; \sigma_e^2, \mathbf{X}) &= \prod_{k=1}^K p(\mathbf{y}(k)|\boldsymbol{\xi}(k); \sigma_e^2, \mathbf{X}) \\
 &= \prod_{k=1}^K \prod_{n=1}^N p(\mathbf{y}_n(k)|\boldsymbol{\xi}_n(k); \sigma_e^2, \mathbf{X}_n) \\
 &= \prod_{k=1}^K \prod_{n=1}^N \frac{1}{|\pi\sigma_e^2\mathbf{I}|} \exp \left\{ -\frac{1}{\sigma_e^2} \left( \mathbf{y}_n(k) - \mathbf{X}_n \tilde{\boldsymbol{\Phi}}_n \boldsymbol{\xi}_n(k) \right)^H \right. \\
 &\quad \left. \left( \mathbf{y}_n(k) - \mathbf{X}_n \tilde{\boldsymbol{\Phi}}_n \boldsymbol{\xi}_n(k) \right) \right\}, \tag{6.9}
 \end{aligned}$$

and

$$\begin{aligned}
 p(\boldsymbol{\Xi}; \sigma_\xi^2) &= \prod_{k=1}^K p(\boldsymbol{\xi}(k); \sigma_\xi^2) \\
 &= \prod_{k=1}^K \prod_{n=1}^N p(\boldsymbol{\xi}_n(k); \sigma_\xi^2) \\
 &= \prod_{k=1}^K \prod_{n=1}^N \frac{1}{|\pi\sigma_\xi^2\mathbf{I}|} \exp \left\{ -\frac{1}{\sigma_\xi^2} \boldsymbol{\xi}_n^H(k) \boldsymbol{\xi}_n(k) \right\}. \tag{6.10}
 \end{aligned}$$

Then, using (6.9) and (6.10), we write the complete data log-likelihood function in canonical exponential family form as [116]

$$\begin{aligned}
L(\sigma_\xi^2, \sigma_e^2, \mathbf{X}) &= \ln p(\mathbf{Y}, \Xi; \sigma_\xi^2, \sigma_e^2, \mathbf{X}) \\
&= \text{const} - N M K \ln(\sigma_e^2) - \frac{K}{\sigma_e^2} \left[ \sum_{n=1}^N \text{tr}(\mathbf{T}_{1n}) + \text{tr}(\mathbf{X}_n^H \mathbf{X}_n \mathbf{T}_{2n}) + \right. \\
&\quad \left. 2\text{Re} \{ \text{tr}(\mathbf{T}_{3n} \mathbf{X}_n^H) \} \right] - N M K \ln(\sigma_\xi^2) - \frac{K}{\sigma_\xi^2} \sum_{n=1}^N \text{tr}(\mathbf{T}_{4n}), \quad (6.11)
\end{aligned}$$

where

$$\begin{aligned}
\mathbf{T}_{1n} &= \frac{1}{K} \sum_{k=1}^K \mathbf{y}_n(k) \mathbf{y}_n^H, \\
\mathbf{T}_{2n} &= \frac{1}{K} \sum_{k=1}^K \tilde{\Phi}_n \boldsymbol{\xi}_n(k) \boldsymbol{\xi}_n^H \tilde{\Phi}_n^H, \\
\mathbf{T}_{3n} &= \frac{1}{K} \sum_{k=1}^K \mathbf{y}_n(k) \boldsymbol{\xi}_n^H \tilde{\Phi}_n^H, \\
\mathbf{T}_{4n} &= \sum_{k=1}^K \boldsymbol{\xi}_n(k) \boldsymbol{\xi}_n^H,
\end{aligned}$$

for  $n = 1, \dots, N$ , are the natural complete-data sufficient statistics.

The complete-data likelihood function belongs to an exponential family; hence we simplify the EM algorithm [116]. In the estimation (E) step, we first calculate the conditional expectation of the natural complete-data sufficient statistics given the observed data [using  $p(\boldsymbol{\xi}_n(k) | \mathbf{y}_n(k); \sigma_\xi, \sigma_e^2, \mathbf{X}_n)$ ]. Then, in the maximization (M) step, we obtain the MLE expressions for the unknown parameters using the complete-data log-likelihood function, and simply replacing the natural complete-data sufficient statistics, obtained in the E step, in the MLE expressions.

**E Step:** We assume that the  $i^{\text{th}}$  iteration estimates of the set of the unknown parameters as  $\boldsymbol{\theta}_n^{(i)} = \{(\hat{\sigma}_\xi^2)^{(i)}, (\hat{\sigma}_e^2)^{(i)}, \hat{\mathbf{X}}_n^{(i)}\}$ , and we compute the conditional expectation w.r.t.  $p(\boldsymbol{\xi}_n(k)|\mathbf{y}_n(k); \boldsymbol{\theta}_n^{(i)})$  of the sufficient statistics under  $\mathcal{H}_1$ :

$$\mathbf{T}_{1n}^{(i)} = \frac{1}{K} \sum_{k=1}^K \mathbf{y}_n(k) \mathbf{y}_n(k)^H, \quad (6.12a)$$

$$\mathbf{T}_{2n}^{(i)} = \frac{1}{K} \sum_{k=1}^K \tilde{\boldsymbol{\Phi}}_n(k) \left[ \tilde{\boldsymbol{\Sigma}}_n^{(i)} + \boldsymbol{\mu}_n^{(i)}(k) (\boldsymbol{\mu}_n^{(i)}(k))^H \right] \tilde{\boldsymbol{\Phi}}_n^H(k), \quad (6.12b)$$

$$\mathbf{T}_{3n}^{(i)} = \frac{1}{K} \sum_{k=1}^K \mathbf{y}_n(k) (\boldsymbol{\mu}_n^{(i)}(k))^H \tilde{\boldsymbol{\Phi}}_n^H(k), \quad (6.12c)$$

$$\mathbf{T}_{4n}^{(i)} = \frac{1}{K} \sum_{k=1}^K \tilde{\boldsymbol{\Sigma}}_n^{(i)} + \boldsymbol{\mu}_n^{(i)}(k) (\boldsymbol{\mu}_n^{(i)}(k))^H, \quad (6.12d)$$

where

- $\boldsymbol{\mu}_n^{(i)}(k) = (\hat{\sigma}_\xi^2)^{(i)} \tilde{\boldsymbol{\Phi}}_n^H \left( \hat{\mathbf{X}}_n^{(i)} \right)^H \left( \boldsymbol{\Sigma}_n^{(i)} \right)^{-1} \mathbf{y}_n(k)$ , and
- $\tilde{\boldsymbol{\Sigma}}_n^{(i)} = (\hat{\sigma}_\xi^2)^{(i)} \mathbf{I} - (\hat{\sigma}_s^2)^{(i)} \tilde{\boldsymbol{\Phi}}_n^H \left( \hat{\mathbf{X}}_n^{(i)} \right)^H \left( \boldsymbol{\Sigma}_n^{(i)} \right)^{-1} \hat{\mathbf{X}}_n^{(i)} \tilde{\boldsymbol{\Phi}}_n$ , where from (6.6),  $\boldsymbol{\Sigma}_n^{(i)} = (\hat{\sigma}_\xi^2)^{(i)} \hat{\mathbf{X}}_n^{(i)} \tilde{\boldsymbol{\Phi}}_n \tilde{\boldsymbol{\Phi}}_n^H \left( \hat{\mathbf{X}}_n^{(i)} \right)^H + (\hat{\sigma}_e^2)^{(i)} \mathbf{I}$ .

Thus,  $\boldsymbol{\mu}_n^{(i)}(k)$  and  $\tilde{\boldsymbol{\Sigma}}_n^{(i)}$  are the mean and the covariance of the conditional distribution  $p(\boldsymbol{\xi}_n(k)|\mathbf{y}_n(k); \boldsymbol{\theta}_n^{(i)})$ , see Appendix H for the details of the computation.

**M Step:** We replace the natural complete-data sufficient statistics with their conditional expectations from (6.12) in the MLE expressions. We first apply the results of the generalized multivariate analysis of variance framework [113] for the MLE of  $\mathbf{X}_n$ , for  $n = 1, \dots, N$ . After concentrating the complete data log-likelihood function in

(6.11) w.r.t. the MLE of  $\mathbf{X}_n$ , we compute the MLEs of  $\sigma_\xi^2$  and  $\sigma_e^2$ .

$$\hat{\mathbf{X}}_n^{(i+1)} = \mathbf{T}_{3n}^{(i)} \left( \mathbf{T}_{2n}^{(i)} \right)^{-1}, \quad (6.13a)$$

$$\begin{aligned} (\hat{\sigma}_e^2)^{(i+1)} &= \frac{1}{NM} \sum_{n=1}^M \left( \text{tr} \left[ \mathbf{T}_{1n}^{(i)} \right] - 2\text{Re}(\text{tr} \left[ (\mathbf{T}_{3n}^H)^{(i)} \mathbf{X}_n^{(i+1)} \tilde{\Phi}_n \right]) \right. \\ &\quad \left. + \text{tr} \left[ (\mathbf{X}^H)^{(i+1)} \tilde{\Phi}_n^H \tilde{\Phi}_n \mathbf{X}^{(i+1)} \mathbf{T}_{2n} \right] \right), \end{aligned} \quad (6.13b)$$

$$(\hat{\sigma}_\xi^2)^{(i+1)} = \frac{1}{NM} \sum_{n=1}^N \text{tr} \left[ \mathbf{T}_{4n}^{(i)} \right]. \quad (6.13c)$$

The above iteration is performed until  $(\hat{\sigma}_\xi^2)^{(i)}$ ,  $(\hat{\sigma}_e^2)^{(i)}$ , and  $\hat{\mathbf{X}}^{(i)}$  converge.

### 6.3.3 Computation of the Cramér-Rao Bound

In this section, to obtain the Wald test in (6.8), we compute the CRB on the error of the  $\sigma_\xi^2$  estimation. We define  $\boldsymbol{\rho} = [\sigma_\xi^2, \sigma_e^2, \text{Re}\{\text{vech}(\mathbf{X}_1)\}^T, \text{Im}\{\text{vech}(\mathbf{X}_1)\}^T, \dots, \text{Re}\{\text{vech}(\mathbf{X}_n)\}^T, \text{Im}\{\text{vech}(\mathbf{X}_n)\}^T]^T$ , such that  $\text{vech}$  creates a single column vector by stacking elements on and below the main diagonal. Then

$\text{vech}(\mathbf{X}_n) = [x_{11}^n, x_{21}^n, \dots, x_{M1}^n, x_{22}^n, x_{32}^n, \dots, x_{M2}^n, \dots, x_{(M-1)(M-1)}^n, x_{(M-1)(M-2)}^n, x_{M(M-2)}^n, x_{M(M-1)}^n, x_{MM}^n]^T$  is an  $\left(\frac{M^2+M}{2}\right) \times 1$  vector of the unknown correlation terms at the  $n^{\text{th}}$  receiver.

Recall that  $\mathbf{X}_n$  for  $n = 1, \dots, N$  is Hermitian symmetric. Therefore, estimating  $\boldsymbol{\rho}$  is the same as estimating  $\boldsymbol{\theta}$  in Section 6.3.1.

Considering the statistical assumptions in Section 6.2.2, we obtain the elements of the FIM [136]:

$$[\mathbf{J}(\boldsymbol{\rho})]_{ij} = \text{tr} \sum_{k=1}^K \sum_{n=1}^N \left( \boldsymbol{\Sigma}_n^{-1} \frac{\partial \boldsymbol{\Sigma}_n}{\partial \rho_i} \boldsymbol{\Sigma}_n^{-1} \frac{\partial \boldsymbol{\Sigma}_n}{\partial \rho_j} \right). \quad (6.14)$$

Next, we obtain

$$\begin{aligned} \frac{\partial \boldsymbol{\Sigma}_n}{\partial \sigma_\xi^2} &= \mathbf{X}_n \tilde{\boldsymbol{\Phi}}_n \tilde{\boldsymbol{\Phi}}_n^H \mathbf{X}_n^H, \\ \frac{\partial \boldsymbol{\Sigma}_n}{\partial \sigma_e^2} &= \mathbf{I}, \\ \frac{\partial \boldsymbol{\Sigma}_n}{\partial \text{Re}\{x_{m'm}^n\}} &= \sigma_\xi^2 \frac{\partial \mathbf{X}_n}{\partial \text{Re}\{x_{m'm}^n\}} \tilde{\boldsymbol{\Phi}}_n \tilde{\boldsymbol{\Phi}}_n^H \mathbf{X}_n^H + \\ &\quad \sigma_\xi^2 \mathbf{X}_n \tilde{\boldsymbol{\Phi}}_n \tilde{\boldsymbol{\Phi}}_n^H \frac{\partial \mathbf{X}_n^H}{\partial \text{Re}\{x_{m'm}^n\}}, \quad m' \geq m \\ \frac{\partial \boldsymbol{\Sigma}_n}{\partial \text{Im}\{x_{m'm}^n\}} &= \sigma_\xi^2 \frac{\partial \mathbf{X}_n}{\partial \text{Im}\{x_{m'm}^n\}} \tilde{\boldsymbol{\Phi}}_n \tilde{\boldsymbol{\Phi}}_n^H \mathbf{X}_n^H + \\ &\quad \sigma_\xi^2 \mathbf{X}_n \tilde{\boldsymbol{\Phi}}_n \tilde{\boldsymbol{\Phi}}_n^H \frac{\partial \mathbf{X}_n^H}{\partial \text{Im}\{x_{m'm}^n\}}, \quad m' \geq m, \end{aligned} \quad (6.15)$$

where

- $\frac{\partial \mathbf{X}_n}{\partial \text{Re}\{x_{m'm}^n\}}$  is an  $M \times M$  matrix of zeros, except for the  $(m'm)^{th}$  and  $(mm')^{th}$  elements, which are equal to one
- $\frac{\partial \mathbf{X}_n}{\partial \text{Re}\{x_{mm}^n\}}$  is an  $M \times M$  matrix of zeros, except for the  $(mm)^{th}$  element, which is equal to one
- $\frac{\partial \mathbf{X}_n}{\partial \text{Im}\{x_{m'm}^n\}}$  is an  $M \times M$  matrix of zeros, except that the  $(mm')^{th}$  element is equal to  $i = \sqrt{-1}$  and the  $(m'm)^{th}$  element is equal to  $-i$ , and
- $\frac{\partial \mathbf{X}_n}{\partial \text{Im}\{x_{mm}^n\}}$  is an  $M \times M$  matrix of zeros, except for the  $(mm)^{th}$  element, which is equal to  $i$ .



The elements of the Fisher information matrix can easily be obtained using (6.15) in (6.14), see Appendix I.

Then  $[\mathbf{J}^{(-1)}(\boldsymbol{\rho})]_{\sigma_\xi^2 \sigma_\xi^2} = [\mathbf{J}^{(-1)}(\boldsymbol{\rho})]_{11}$  is the CRB on the  $\sigma_\xi^2$  estimation error.

### 6.3.4 Detection Performance

In this section, we analyze the asymptotic statistical characteristics of the Wald test proposed in (6.8). In Section 6.4, we use these asymptotic characteristics to demonstrate the change in detection performance due to changes in the level of the cross-correlation terms.

When we apply the Wald test in (6.8) to the hypothesis testing problem formulated in (6.7), following the results in [68, Chapter 6 and Appendix 6C], we can show that

$$T_W \sim \begin{cases} \mathcal{X}_1^2 & \text{under } \mathcal{H}_0 \\ \mathcal{X}_1^2(\lambda) & \text{under } \mathcal{H}_1 \end{cases}, \quad (6.16)$$

where

- $\mathcal{X}_1^2$  is a central chi-square distribution with one degree of freedom
- $\mathcal{X}_1^2(\lambda)$  is a non-central chi-square distribution with one degree of freedom and a non-centrality parameter  $\lambda$ , and
- $\lambda = (\sigma_\xi^2) \left( \text{CRB}_{\sigma_\xi^2} \right)^{-1} (\sigma_\xi^2)$ .

Here  $\sigma_\xi^2$  is the true value under  $\mathcal{H}_1$ , and following the discussions in Section 6.3.3,  $\text{CRB}_{\sigma_\xi^2} = [\mathbf{J}^{(-1)}(\boldsymbol{\rho})]_{\sigma_\xi^2 \sigma_\xi^2}$  is the CRB on  $\sigma_\xi^2$  estimation error, and it is computed using the true values of  $\boldsymbol{\rho}$  under  $\mathcal{H}_1$ .

We rewrite  $\boldsymbol{\rho} = [\sigma_\xi^2, \tilde{\boldsymbol{\rho}}^T]^T$ , such that  $\tilde{\boldsymbol{\rho}} = [\sigma_e^2, \text{Re}\{\text{vech}(\mathbf{X}_1)\}^T, \text{Im}\{\text{vech}(\mathbf{X}_1)\}^T, \dots, \text{Re}\{\text{vech}(\mathbf{X}_n)\}^T, \text{Im}\{\text{vech}(\mathbf{X}_n)\}^T]^T$ . Accordingly we partition the Fisher information matrix

$$\mathbf{J}(\boldsymbol{\rho}) = \begin{bmatrix} \mathbf{J}_{\sigma_\xi^2 \sigma_\xi^2}(\boldsymbol{\rho}) & \mathbf{J}_{\sigma_\xi^2 \tilde{\boldsymbol{\rho}}}(\boldsymbol{\rho}) \\ \mathbf{J}_{\tilde{\boldsymbol{\rho}} \sigma_\xi^2}(\boldsymbol{\rho}) & \mathbf{J}_{\tilde{\boldsymbol{\rho}} \tilde{\boldsymbol{\rho}}}(\boldsymbol{\rho}) \end{bmatrix}. \quad (6.17)$$

Then  $[\mathbf{J}^{(-1)}(\boldsymbol{\rho})]_{\sigma_\xi^2 \sigma_\xi^2} = \left[ \mathbf{J}_{\sigma_\xi^2 \sigma_\xi^2} - \mathbf{J}_{\sigma_\xi^2 \tilde{\boldsymbol{\rho}}} \mathbf{J}_{\tilde{\boldsymbol{\rho}} \tilde{\boldsymbol{\rho}}}^{-1} \mathbf{J}_{\tilde{\boldsymbol{\rho}} \sigma_\xi^2} \right]^{-1}$  is a scalar, and hence

$$\lambda = (\sigma_\xi^2)^2 \left( \mathbf{J}_{\sigma_\xi^2 \sigma_\xi^2}(\boldsymbol{\rho}) - \mathbf{J}_{\sigma_\xi^2 \tilde{\boldsymbol{\rho}}}(\boldsymbol{\rho}) \mathbf{J}_{\tilde{\boldsymbol{\rho}} \tilde{\boldsymbol{\rho}}}^{-1}(\boldsymbol{\rho}) \mathbf{J}_{\tilde{\boldsymbol{\rho}} \sigma_\xi^2}(\boldsymbol{\rho}) \right). \quad (6.18)$$

Using the asymptotic distribution of the detector, we compute the probability of false alarm ( $P_{\text{FA}}$ ) and probability of detection ( $P_{\text{D}}$ ):

$$P_{\text{FA}} = \mathcal{Q}_{\mathcal{X}_1^2}(\nu) = \eta, \quad (6.19)$$

where  $\mathcal{Q}_{\mathcal{X}_1^2}(\cdot)$  is the right tail of the central chi-square  $\mathcal{X}_1^2$  probability density function (pdf). For a given  $P_{\text{FA}}$ , the threshold value is  $\nu = \mathcal{Q}_{\mathcal{X}_1^2}^{-1}(\eta)$ . Then considering  $\nu$ ,

$$P_{\text{D}} = \mathcal{Q}_{\mathcal{X}_1^2(\lambda)}(\nu), \quad (6.20)$$

where  $\mathcal{Q}_{\mathcal{X}_1^2(\lambda)}(\cdot)$  is the right tail of the non-central chi-square  $\mathcal{X}_1^2(\lambda)$  pdf, with  $\lambda$  as the non-centrality parameter.

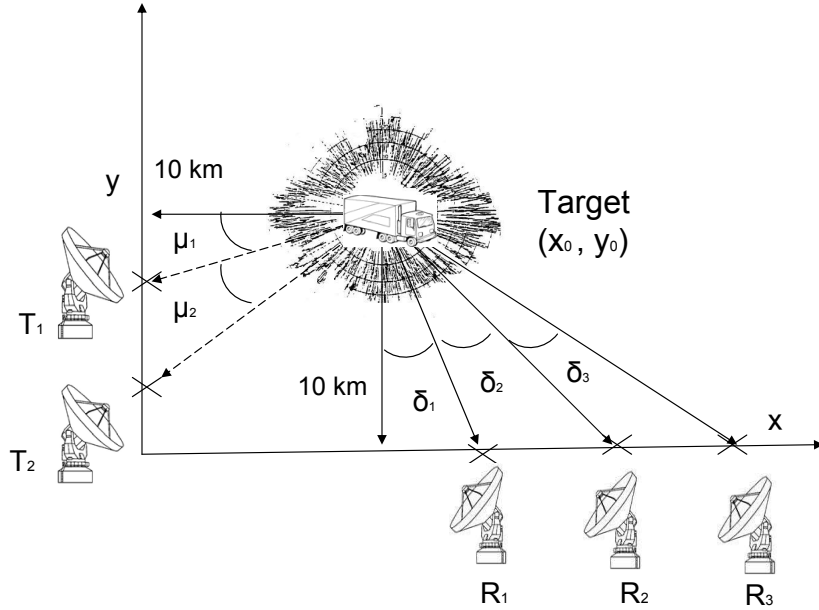


Figure 6.1: MIMO antenna system with  $M$  transmitters and  $N$  receivers.

## 6.4 Numerical Examples

We present numerical examples to illustrate our analytical results on the sensitivity of MIMO radar target detection to changes in the cross-correlation levels of multiple signals received from different transmitters. Using the asymptotic theoretical results from Section 6.3.4, we show the effect of the changes in CCL on the distribution, the receiver operating characteristics (ROC), and the detection probability of the statistical test. We also compare the asymptotic and actual ROCs of the Wald detector. We use the EM algorithm from Section 6.3.2 to numerically compute the actual ROC curve of the decision test in Section 6.3.1. The numerical results are obtained from  $2 * 10^3$  Monte Carlo simulation runs.

We follow the scenario shown in Fig. 6.1. We assume that our system is composed of  $M$  transmitters and  $N$  receivers, where the antennas are widely separated. The

transmitters are located on the y-axis, whereas the receivers are on the x-axis; the target is 10km from each of the axes (i.e.,  $(x_0, y_0) = (10 \text{ km}, 10 \text{ km})$ ); the antenna gains ( $G_{Tx}$  and  $G_{Rx}$ ) are 30dB; the signal frequency ( $f_c$ ) is 1GHz. The angles between the transmitted signals are  $\mu_1, \mu_2, \dots, \mu_M$  and similarly between the received signals are  $\delta_1, \dots, \delta_N$ . We consider three different MIMO setups in our examples.

- $M = 2$  and  $N = 3$  (MIMO  $2 \times 3$ );  $\mu_1 = 10^\circ$ , and  $\mu_2 = 20^\circ$ ;  $\delta_1 = 10^\circ$ ,  $\delta_2 = 10^\circ$ , and  $\delta_3 = 25^\circ$ ;
- $M = 3$  and  $N = 3$  (MIMO  $3 \times 3$ );  $\mu_1, \mu_2$  are the same as MIMO  $2 \times 3$ , and  $\mu_3 = 35^\circ$ ;  $\delta_1, \delta_2$ , and  $\delta_3$  are the same as MIMO  $2 \times 3$ ;
- $M = 3$  and  $N = 5$  (MIMO  $3 \times 5$ );  $\mu_1, \mu_2$ , and  $\mu_3$  are the same as MIMO  $3 \times 3$ ;  $\delta_1, \delta_2$ , and  $\delta_3$  are the same as MIMO  $2 \times 3$ ,  $\delta_4 = 20^\circ$ , and  $\delta_5 = 20^\circ$ .

Then  $R_m, m = 1, \dots, M$ , and  $R_n, n = 1, \dots, N$ , in (6.1) are calculated accordingly. In this scenario, all the transmitters and receivers see the target from different angles.

We define the signal-to-noise ratio (SNR) as the ratio between the traces of the signal covariance and noise covariance:

$$\text{SNR} = \frac{\sigma_\xi^2}{\sigma_e^2} \left[ \frac{\sum_{n=1}^N \text{tr} \left( \mathbf{X}_n \tilde{\Phi}_n \tilde{\Phi}_n^H \mathbf{X}_n^H \right)}{NM} \right]. \quad (6.21)$$

We define the average CCL (ACCL) as the ratio between the total power of the non-zero cross-correlation terms and the self correlation of the individual signals, then ACCL becomes

$$\text{ACCL} = -10 \log_{10} \left[ \frac{M-1}{2} \left( \frac{\sum_{n=1}^N \sum_{m=1}^M (x_{mm}^n)(x_{mm}^n)^*}{\sum_{n=1}^N \sum_{m'=2}^M \sum_{m=1}^{m'} (x_{m'm}^n)(x_{m'm}^n)^*} \right) \right]. \quad (6.22)$$

For example  $\text{ACCL} = -10$  dB means that the ACCL is 10 dB below the average self-correlation values. As the ACCL decreases, separation of the transmitted signals for different delays gets easier. In the following we investigate the effect of changes in the ACCL on detection performance.

In Fig. 6.2, for fixed  $P_{\text{FA}} = 0.01$  and  $\text{SNR} = -5$  dB, using the asymptotic statistical characteristics from Section 6.3.4, we plot the pdf of the Wald test detector for different MIMO configurations, MIMO  $2 \times 3$  (Fig. 6.2(a)), MIMO  $3 \times 3$  (Fig. 6.2(b)) and MIMO  $3 \times 5$  (Fig. 6.2(c)) at different ACCL values (-5, -10 and -20 dB). In the figure,  $\lambda_x$  corresponds to the non-centrality  $\lambda$  in (6.18) computed for  $\text{ACCL} = x$  dB. For Figs. 6.2(a), 6.2(b) and 6.2(c), we observe that as the ACCL decreases, the pdf shifts to the right. For non-central  $\mathcal{X}_1^2$ , this corresponds to an increase in the non-centrality parameter  $\lambda$ . This increase is expected because as the ACCL decreases, the CRB for  $\sigma_\xi^2$  decreases, and accordingly  $\lambda$  increases [see (6.18)]. For a given  $P_{\text{FA}} = 0.01$  and the corresponding threshold  $\nu = 6.6349$ , the  $P_{\text{D}}$  is obtained by computing the area under the pdf starting from  $\nu$  (right tail probability). Therefore, as  $\lambda$  increases,  $P_{\text{D}}$  also increases. Then, we conclude that a decrease in the ACCL corresponds to an increase in  $P_{\text{D}}$ . Moreover, in these figures, we observe that as the number of the receivers and transmitters increases, the  $P_{\text{D}}$  increases, but a system with more receivers and/or transmitters is more sensitive to changes in the ACCL.

In Fig. 6.3, for fixed  $\text{SNR} = -5$  dB and for different MIMO configurations, MIMO  $2 \times 3$  (Fig. 6.3(a)), MIMO  $3 \times 3$  (Fig. 6.3(b)) and MIMO  $3 \times 5$  (Fig. 6.3(c)) at different ACCL values (-5, -10 and -20 dB), we demonstrate both the asymptotic and numerical receiver operating characteristics of the statistical decision test. For a large number of transmitted pulses,  $K = 500$ , we obtain the numerical ROC using the EM algorithm proposed in Section 6.3.2 in (6.8). We show that for sufficiently large  $K$ , the actual

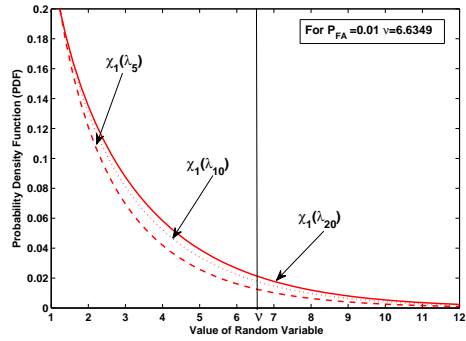
ROC of the Wald test is very close to the asymptotic one. Similar to Fig. 6.3, we observe that as the ACCL decreases, the detection performance improves. As we also mention above, this improvement is due to the fact that a decrease in the ACCL results in a decrease in the CRB of the  $\sigma_\xi^2$  estimation error, causing an increase in the non-centrality parameter in (6.18), and hence an increase in  $P_D$ . Moreover, a system with more transmitters and/or receivers has better detection performance, but also more sensitivity to changes in ACCL.

In Fig. 6.4, for fixed  $P_{FA} = 0.01$ , we plot the  $P_D$  as a function of the SNR for different MIMO configurations and different ACCL values. This figure also supports our argument on the relationship between changes in the ACCL and detection performance: a decrease in the ACCL improves the detection performance. In this figure, we can also observe the effect of the number of the transmitters and/or receivers on the detection performance. Systems with more antennas have better performance, but the increase in performance comes with a price: such a system becomes more sensitive to changes in the ACCL.

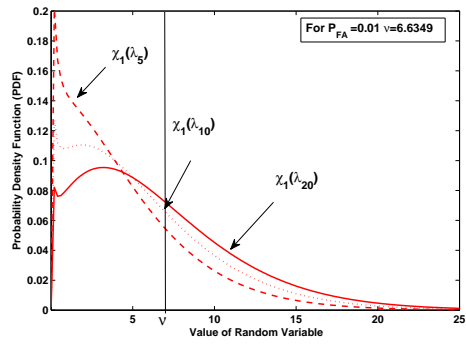
## 6.5 Summary

We analyzed the detection sensitivity of MIMO radar to changes in the cross-correlation levels of the signals at each receiver from different transmitters. We formulated a MIMO radar measurement model considering the correlation terms as deterministic unknowns. We proposed to use an EM based algorithm to estimate the target, correlation, and noise parameters. We then developed a Wald test for target detection, using the estimates obtained from the EM estimation step. We also computed the CRB on the error of parameter estimation, and used these results to obtain an

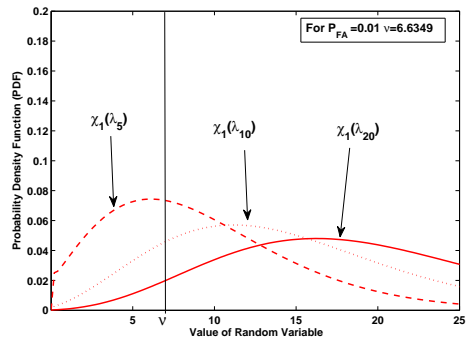
asymptotical statistical characterization of the detection test. Using the asymptotical results and Monte Carlo simulations, we demonstrated the sensitivity of the MIMO radar target detection performance to changes in the cross-correlation levels of the received signals. We showed that as the level of the correlation increases, the detection performance deteriorates. We observed that MIMO systems with more transmitters and/or receivers have better detection performance, but they are more sensitive to changes in the correlation levels.



(a)



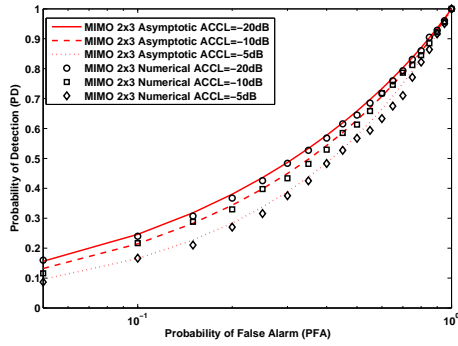
(b)



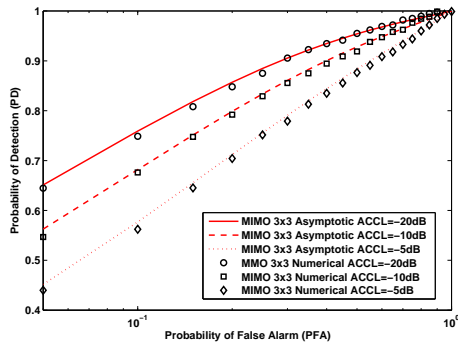
(c)

Figure 6.2: Probability density function of the test statistics under  $\mathcal{H}_1$  for different ACCL values and (a) MIMO  $2 \times 3$  (b) MIMO  $3 \times 3$  (c) MIMO  $3 \times 5$  configurations.

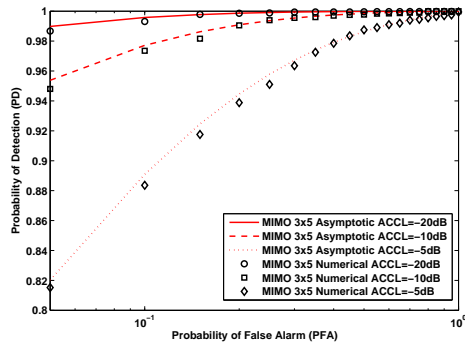




(a)



(b)



(c)

Figure 6.3: Receiver operating characteristics of the target detector for different ACCL values and (a) MIMO  $2 \times 3$  (b) MIMO  $3 \times 3$  (c) MIMO  $3 \times 5$  configurations.

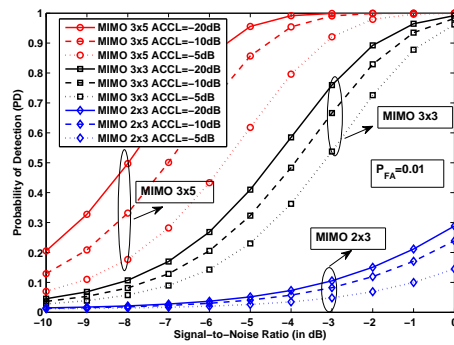


Figure 6.4: Probability of detection vs. SNR for different ACCL values ( $P_{FA} = 0.01$ ).

# Chapter 7

## Conclusions and Future Work

In this dissertation, we reported our contributions to biologically inspired sensing and multi-input multi-output radar processing. We quantitatively demonstrated the localization accuracy of the mechanically coupled ears of a female *Ormia ochracea*. Then inspired by the *Ormia*'s ears we developed a multiple-antenna array system with improved localization and radiation performance. Moreover, we addressed multiple problems related to target detection using MIMO radar: target detection in non-homogeneous clutter, the effect of phase synchronization mismatch between transmitter and receiver pairs on the detection performance, and the sensitivity analysis for the target detection performance. In the following, first we summarize our results and then give some examples as possible future extensions to our work.

### 7.1 Conclusions

In our work on biologically inspired sensing we focused on the mechanically coupled ears of a female *Ormia ochracea*. The female *Ormia ochracea*, a parasitoid fly, locates male crickets very accurately as part of its reproduction. This is unexpected as the

distance between its ears is much smaller than the wavelength of the cricket's mating call. This phenomenon has been explained by a mechanical coupling between the ears. In our research, we analyzed the localization accuracy of the female *Ormia*'s coupled ears using a statistical approach. We converted the mechanical coupling model to a statistical one and analyzed the accuracy by computing the Cramér-Rao bound (CRB) on estimating directions of arrival. We quantitatively demonstrated that the coupling improves the accuracy of direction estimation in the presence of interference and noise.

We developed a multiple-antenna array system with couplings inspired by the female *Ormia ochracea*'s ears. The mechanical coupling between the *Ormia*'s ears has been modeled by a pair of differential equations. We first solved the differential equations governing the female *Ormia*'s ear response. We then transformed the response to fit desired radio frequencies, and computed the array response of the biologically inspired multiple-antenna array. For the resulting system, we derived the maximum likelihood estimates of source directions and analyzed the performance improvement by computing the error bounds. Moreover, we considered an active transmitting antenna array with coupling, and obtained the array factor of the desired multiple-antenna system for pre-specified radio frequencies. We computed the radiation intensity of this system and analyzed its half-power beamwidth, sidelobe levels and directivity of the radiation pattern. We demonstrated the improvement in these performance measures due to the biologically inspired coupling using numerical examples. The improvement in the localization and radiation performance of small-sized arrays is very exciting, since such compact systems are crucial for many applications that require small confined spaces (cellular phones using their own signals for localization, for instance).

Next, we studied target detection problems using MIMO radar in the presence of realistic clutter and practical limitations. MIMO radars are useful to discriminate a target from clutter using the spatial diversity of the scatterers in the illuminated scene. We considered the detection of targets in compound-Gaussian clutter, to fit such scenarios as scatterers with heavy-tailed distributions for high-resolution and/or low-grazing-angle radars in the presence of sea or foliage clutter. First, we introduced a data model using an inverse gamma distribution to represent the clutter texture. Then, we applied the parameter-expanded expectation-maximization algorithm to estimate the clutter texture and speckle as well as the target parameters. We developed a statistical decision test using these estimates and approximate its statistical characteristics. Based on this test, we proposed an algorithm that adaptively distributes the total transmitted energy among the transmitters to improve the detection performance. We demonstrated the advantages of MIMO radar and the adaptive power allocation algorithm in clutter environments using Monte Carlo simulations.

Then, we considered the problem of target detection for MIMO radar in the presence of a phase synchronization mismatch between the transmitter and receiver pairs. Such mismatch often occurs due to imperfect knowledge of the locations and local oscillator characteristics of the antennas. First, we introduced a data model using a von-Mises distribution to represent the phase error terms. Then, we proposed a method based on the expectation-maximization algorithm to estimate the error distribution parameter, target returns, and noise variance. We developed a generalized likelihood ratio test target detector using these estimates. Based on the mutual information between the radar measurements and received target returns (and hence the phase error), we proposed an algorithm to adaptively distribute the total transmitted energy among

the transmitters. Using Monte Carlo simulations, we demonstrated that the adaptive energy allocation, increase in the phase information, and realistic measurement modeling improve the detection performance.

Finally, we considered the effect of the imperfect separability of the received signals on detection performance. In practice, mutual orthogonality among the received signals cannot be achieved for all delay and Doppler pairs. We introduced a data model considering the correlation among the data from different transmitter-receiver pairs as unknown parameters. We formulated a method to estimate the target, correlation, and noise parameters, and then used these estimates to develop a statistical decision test. Using the asymptotical statistical characteristics and the numerical performance of the test, we analyzed the sensitivity of the MIMO radar with respect to changes in the cross-correlation levels of the measurements. Using theoretical results and numerical examples, we demonstrated the effect of changes in the correlation among the received signals from different transmitters on the detection performance. We observed that a decrease in the correlation corresponds to an increase in detection performance, and that as the number of the receivers and transmitters increases, the probability of detection increases, but a system with more receivers and/or transmitters is more sensitive to changes in the correlation values.

## 7.2 Future Work

We believe our results on biologically inspired antenna array design are promising, and building on them motivates our future plans as follows. We will consider other possible array configurations. We will develop algorithms to optimize the array configuration for the maximum biologically inspired coupling effect. We will consider

realistic unknown undesired electromagnetic coupling. It is of interest to investigate the deterioration in performance due to the undesired coupling. In this context, we will compute the maximum likelihood estimation algorithm and corresponding Cramér-Rao bound for finding the source directions as well as the unknown, undesired mutual coupling parameters (calibration). Then, we will also analyze the effect of calibration error on the estimation accuracy by computing the Cramér-Rao bound on direction of arrival estimation error in the presence of calibration error. Moreover, we will add polarimetry vector sensors, and demonstrate the improvement in the source identifiability capacity and angular resolution of the system. We will employ the different polarizations as additional degrees of freedom for optimum beam pattern design.

For the MIMO radar, we have analyzed the effects of the phase mismatch between the transmitting and receiving antennas, and the cross-correlation levels of the received signals on the detection performance separately. For more realistic radar processing, we will extend our model to include the effects of both the phase ambiguity and non-orthogonality of the received signals, and demonstrate the changes in the detection performance. We will also analyze the effect of these practical limitations in the presence of homogeneous and non-homogeneous clutter. We will develop more realistic target models to demonstrate the effect of spatial diversity. Then, we will apply our approach to the moving target scenarios, first for target detection and then for target tracking. Considering realistic scenarios and conditions, we will develop target tracking algorithms for MIMO radar using sequential Bayesian inference approach. The use of sequential Bayesian framework will also allow us to predict the future system-states making it feasible to adaptively design the system. We will use sequential

Morkov chain Monte Carlo methods to deal with the complexity and non-linearity of the realistic target environments.



# Appendix A

## Definitions of Block Matrix Operators

In this appendix we define several block matrix operators used in Section 3.2.2 similar to [99]. We employ the following notation for a blockwise partitioned matrix  $\mathbf{A}$  of  $m\mu \times n\nu$

$$\mathbf{A} = \begin{bmatrix} \mathbf{A}_{\langle 11 \rangle} & \cdots & \mathbf{A}_{\langle 1n \rangle} \\ \cdot & & \cdot \\ \cdot & & \cdot \\ \cdot & & \cdot \\ \mathbf{A}_{\langle m1 \rangle} & \cdots & \mathbf{A}_{\langle mn \rangle} \end{bmatrix}, \quad (\text{A.1})$$

where  $\mathbf{A}_{ij}$  is an  $\mu \times \nu$  sized block matrix. We use the following definitions.

**Definition A.1.** *Block transpose* The block transposed matrix  $\mathbf{A}^{bT}$  is an  $n\mu \times m\nu$  matrix with block entries

$$(\mathbf{A}^{bT})_{\langle ij \rangle} = \mathbf{A}_{\langle ji \rangle}. \quad (\text{A.2})$$

**Definition A.2.** *Block Schur-Hadamard product* Similar to  $\mathbf{A}$ , a matrix  $\mathbf{B}$  of size  $m\nu \times n\eta$  has blocks  $\mathbf{B}_{\langle ij \rangle}$  of dimension  $\nu \times \eta$  (equal size). Then the block Schur-Hadamard product  $\mathbf{A} \boxtimes \mathbf{B}$  is an  $m\mu \times n\eta$  block-wise partitioned matrix with the following entries:

$$(\mathbf{A} \boxtimes \mathbf{B})_{\langle ij \rangle} = \mathbf{A}_{\langle ij \rangle} \mathbf{B}_{\langle ij \rangle}, \quad (\text{A.3})$$

such that each block entry is an  $\mu \times \eta$  matrix.

**Definition A.3.** *Block trace operator* Assume  $\mathbf{A}$  of (A.1) has  $\mu = \nu$ . Then the block trace operator  $\text{btr}[\mathbf{A}]$  is an  $m \times n$  matrix with entries

$$(\text{btr}[\mathbf{A}])_{ij} = \text{tr} \mathbf{A}_{\langle ij \rangle}. \quad (\text{A.4})$$

# Appendix B

## Computation of Matrix $C$ in (3.23)

An antenna in the transmitting mode can be modeled as in Figure B.1. Assuming  $M$  element antenna array, and considering the mutual effect of the other antennas in the array, the induced current on the  $i^{th}$  antenna can be computed through (see also [84] and [105])

$$p_i(Z_{ii} + Z_g) = v_{gi} - \sum_{k \neq i}^M p_k Z_{ik}, \quad (\text{B.1})$$

where,

- $p_j$ ,  $j = 1, \dots, M$ , is the induced current on the  $j^{th}$  antenna;
- $Z_{jj}$  is the self impedance of the  $j^{th}$  antenna;

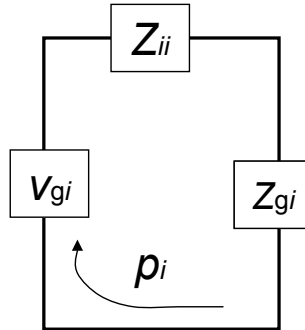


Figure B.1: Circuit model of the  $i^{th}$  antenna element in the transmitting mode.

- $Z_g$  is the generator impedance;
- $v_{gj}$  is the generator voltage applied to the  $j^{\text{th}}$  antenna; and
- $Z_{jk}$  is the mutual impedance between the  $j^{\text{th}}$  and  $k^{\text{th}}$  antennas.

Assuming identical antennas and generators (identical self and generator impedances), we can rewrite (B.1) and obtain

$$\begin{bmatrix} Z_{11} + Z_g & Z_{12} & \cdots & Z_{1M} \\ Z_{21} & Z_{22} + Z_g & \cdots & Z_{2M} \\ & & \cdots & \\ Z_{M1} & Z_{M2} & \cdots & Z_{MM} + Z_g \end{bmatrix} \begin{bmatrix} p_1 \\ \cdot \\ \cdot \\ \cdot \\ p_M \end{bmatrix} = \begin{bmatrix} v_{g1} \\ \cdot \\ \cdot \\ \cdot \\ v_{gM} \end{bmatrix}. \quad (\text{B.2})$$

Then recalling from Section 3.3.1 that  $\mathbf{p} = \mathbf{C}\mathbf{v}$ , we get

$$\mathbf{C} = \begin{bmatrix} Z_{11} + Z_g & Z_{12} & \cdots & Z_{1M} \\ Z_{21} & Z_{22} + Z_g & \cdots & Z_{2M} \\ & & \cdots & \\ Z_{M1} & Z_{M2} & \cdots & Z_{MM} + Z_g \end{bmatrix}^{-1} \quad (\text{B.3})$$

# Appendix C

## Computation of the matrix $P$ in (4.18)

In this appendix, we compute the matrix  $P$  of (4.18). Since  $\phi = [1, \dots, 1]_{1 \times K}$ ,

$$\text{tr}(\Sigma^{-1}(\mathbf{A}\mathbf{x}\phi)(\mathbf{A}\mathbf{x}\phi)^H) = K(\mathbf{A}\mathbf{x})^H \Sigma^{-1}(\mathbf{A}\mathbf{x}). \quad (\text{C.1})$$

Recall from (4.5) that

- $\mathbf{A} = \text{blkdiag}(\mathbf{A}_1, \dots, \mathbf{A}_M)$
- $\mathbf{A}_i = \beta_i \text{diag}(\alpha_{1i} e^{-j\psi_{1i}}, \dots, \alpha_{N_i i} e^{-j\psi_{N_i i}}) = \beta_i \bar{\mathbf{A}}_i$
- $\mathbf{x} = [\mathbf{x}_1^T, \dots, \mathbf{x}_M^T]^T$
- $\mathbf{x}_i = [x_{1i}, \dots, x_{N_i i}]^T$ , and
- $\Sigma = \text{blkdiag}(\Sigma_1, \dots, \Sigma_M)$ , see also Section 4.5 for the covariance matrix assumption.

Then

$$\begin{aligned} K(\mathbf{A}\mathbf{x})^H \boldsymbol{\Sigma}^{-1}(\mathbf{A}\mathbf{x}) &= K \sum_{m=1}^M \beta_m^2 (\bar{\mathbf{A}}_m \mathbf{x}_m)^H \boldsymbol{\Sigma}_m^{-1} (\bar{\mathbf{A}}_m \mathbf{x}_m), \\ &= \boldsymbol{\beta}^H \mathbf{P} \boldsymbol{\beta}, \end{aligned} \tag{C.2}$$

where  $\mathbf{P} = K \text{diag}((\bar{\mathbf{A}}_1 \mathbf{x}_1)^H \boldsymbol{\Sigma}_1^{-1} (\bar{\mathbf{A}}_1 \mathbf{x}_1), \dots, (\bar{\mathbf{A}}_M \mathbf{x}_M)^H \boldsymbol{\Sigma}_M^{-1} (\bar{\mathbf{A}}_M \mathbf{x}_M))$ .

# Appendix D

## Proof of the identity in (5.15)

The identity in (5.15) is in common use; c.f. [66]. However, for the sake of completeness, we provide an outline of the proof in this section.

To prove the identity, we need the following lemma.

**Lemma D.1.**

$$B\left(\frac{1}{2}, m + \frac{1}{2}\right) = 2 \int_0^{\pi/2} (\cos \tilde{\theta})^{2m} d\tilde{\theta}, \quad (\text{D.1})$$

and

$$B\left(\frac{1}{2}, m + \frac{1}{2}\right) = \frac{\pi(2m)!}{2^{2m}\Gamma(m+1)\Gamma(m+1)}, \quad (\text{D.2})$$

where  $B(\cdot, \cdot)$  and  $\Gamma(\cdot)$  are the Beta and Gamma functions, respectively.

*Proof.* Taking the definition of Beta function from [137]:

$$\begin{aligned} B(x, y) &= 2 \int_0^{\pi/2} (\sin \tilde{\theta})^{2x-1} (\cos \tilde{\theta})^{2y-1} d\tilde{\theta} \\ &= \frac{\Gamma(x)\Gamma(y)}{\Gamma(x+y)}. \end{aligned} \quad (\text{D.3})$$

Direct application of  $x = 1/2$  and  $y = m + 1/2$  results in (D.1). To obtain (D.2), we use the Legendre duplication formula [137]:

$$\Gamma(m)\Gamma\left(m + \frac{1}{2}\right) = 2^{\frac{1}{2}-2m} \sqrt{(2\pi)}\Gamma(2m).$$

□

In the proof of (5.15), we also employ the series expansion of the modified Bessel function of the first kind with order  $p$  [66, Appendix A]:

$$I_p(K) = \sum_{m=0}^{\infty} \frac{1}{\Gamma(p+m+1)\Gamma(m+1)} \left(\frac{K}{2}\right)^{2m+p}. \quad (\text{D.4})$$

Using the Maclaren series expansion of the exponential function, (5.15) becomes

$$Q1 = \int_{-\pi}^{\pi} \sum_{r=0}^{\infty} \frac{(a \cos \tilde{\theta} + b \sin \tilde{\theta})^r}{r!} d\tilde{\theta}. \quad (\text{D.5})$$

It is not difficult to show that the integral of terms corresponding to  $r = 2m + 1$ ,  $m = 0, 1, , \dots$  in (D.5) is equal to zero.

For  $r = 2m$ ,  $m = 1, 2, \dots$ , using the binomial expansion of  $(a \cos \tilde{\theta} + b \sin \tilde{\theta})^r$ , we write

$$\begin{aligned} Q1 &= \int_{-\pi}^{\pi} \sum_{r=0,2, \text{ (even)}}^{\infty} \frac{1}{r!} \sum_{k=0,2, \text{ (even)}}^r \binom{r}{k} a^{r-k} b^k (\cos \tilde{\theta})^{r-k} (\sin \tilde{\theta})^k d\tilde{\theta} \\ &= \int_{-\pi}^{\pi} \sum_{r=0,2 \text{ (even)}}^{\infty} \frac{1}{r!} \sum_{k=0,2, \text{ (even)}}^r \binom{r}{k} a^{r-k} b^k \sum_{n=0}^{k/2} \binom{k/2}{n} (-1)^n (\cos \tilde{\theta})^{r-k+2n} d\tilde{\theta}. \end{aligned} \quad (\text{D.6})$$



The integration of odd powers in the binomial expansion results in zero. On the right hand side (R.H.S.) of the second line in (D.6), we write  $(\sin \tilde{\theta})^k = (1 - (\cos \tilde{\theta})^2)^{k/2}$  and use its binomial expansion. Then computing the integration and using (D.1) from Lemma D.1, we obtain

$$Q1 = \sum_{r=0,2,(\text{even})}^{\infty} \frac{1}{r!} \sum_{k=0,2,(\text{even})}^r \binom{r}{k} a^{r-k} b^k \sum_{n=0}^{k/2} \binom{k/2}{n} (-1)^n 2B\left(1/2, \frac{r-k+2n}{2} + \frac{1}{2}\right). \quad (\text{D.7})$$

We define  $r = 2m$  and compute the last summation on the R.H.S. of (D.7) employing (D.2) from Lemma D.1. Then

$$\begin{aligned} Q1 &= \sum_{m=0}^{\infty} \frac{1}{(2m)!} \sum_{k=0,2,(\text{even})}^{2m} 2 \binom{m}{k/2} a^{2(m-k/2)} b^{2(k/2)} B\left(\frac{1}{2}, m + \frac{1}{2}\right) \\ &= \sum_{m=0}^{\infty} \frac{2\pi}{\Gamma(m+1)\Gamma(m+1)} \left(\frac{(a^2 + b^2)^{1/2}}{2}\right)^{2m} \\ &= 2\pi I_0(\sqrt{a^2 + b^2}). \end{aligned} \quad (\text{D.8})$$

To compute the second line from the first, we use (D.2) and the identity  $\sum_{k=0,2,(\text{even})}^{2m} \binom{m}{k/2} a^{2(m-k/2)} b^{2(k/2)} = ((a^2 + b^2)^{1/2})^{2m}$ . To obtain the third line from the second we employ the series expansion of the modified Bessel function of the first kind with order 0 from (D.4).

# Appendix E

## Proof of the identity in (5.18)

We follow an approach similar to Appendix D for the proof of (5.18). Using the Maclaurin series expansion of the exponential function, we write (5.18) as

$$Q2 = \int_{-\pi}^{\pi} (\cos \tilde{\theta} + j \sin \tilde{\theta}) \sum_{r=1,3, \text{ (odd)}}^{\infty} \frac{(a \cos \tilde{\theta} + b \sin \tilde{\theta})^r}{r!} d\tilde{\theta}. \quad (\text{E.1})$$

The integral of the terms corresponding to  $r = 2m$ ,  $m = 0, 1, , \dots$  in (E.1) is equal to zero.

We separate (E.1) into two integrals (E.2) and (E.5). Using the binomial expansion of  $(a \cos \tilde{\theta} + b \sin \tilde{\theta})^r$ , we have

$$Q21 = \int_{-\pi}^{\pi} \sum_{r=1,3, \text{ (odd)}}^{\infty} \frac{1}{r!} \cos \tilde{\theta} \sum_{k=0,2, \text{ (even)}}^{r-1} \binom{r}{k} a^{r-k} b^k (\cos \tilde{\theta})^{r-k} (\sin \tilde{\theta})^k d\tilde{\theta}. \quad (\text{E.2})$$

The integral of the terms with odd  $k$  in (E.2) is equal to zero. Following the steps in (D.6) and (D.7),

$$Q_{21} = \sum_{r=1,3, \text{ (odd)}}^{\infty} \frac{1}{r!} \sum_{k=0,2, \text{ (even)}}^{r-1} \binom{r}{k} a^{r-k} b^k \sum_{n=0}^{k/2} \binom{k/2}{n} (-1)^n {}_2B \left( 1/2, \frac{r-k+2n+1}{2} + \frac{1}{2} \right). \quad (\text{E.3})$$

Employing (D.2) from Lemma D.1 and computing the last summation on the R.H.S.,

$$Q_{21} = \sum_{r=1,3, \text{ (odd)}}^{\infty} \frac{1}{r!} \sum_{k=0,2, \text{ (even)}}^{r-1} \binom{(r-1)/2}{k/2} a^{r-k} b^k B \left( 1/2, \frac{r+1}{2} + \frac{1}{2} \right). \quad (\text{E.4})$$

Similarly,

$$Q_{22} = j \int_{-\pi}^{\pi} \sum_{r=1,3, \text{ (odd)}}^{\infty} \frac{1}{r!} \sin \tilde{\theta} \sum_{k=1,3, \text{ (odd)}}^r \binom{r}{k} a^{r-k} b^k (\cos \tilde{\theta})^{r-k} (\sin \tilde{\theta})^k d\tilde{\theta}. \quad (\text{E.5})$$

Note that the integral of the binomial expansion terms for which  $k = 2m$ ,  $m = 1, 2, \dots$  is zero. Writing the binomial expansion of  $(\sin \tilde{\theta})^{k+1} = (1 - (\cos \tilde{\theta})^2)^{\frac{k+1}{2}}$  and using the definition of Beta function from (D.1),

$$Q_{22} = j \sum_{r=1,3, \text{ (odd)}}^{\infty} \frac{1}{r!} \sum_{k=1,3, \text{ (odd)}}^r \binom{r}{k} a^{r-k} b^k \sum_{n=0}^{(k+1)/2} \binom{(k+1)/2}{n} (-1)^n {}_2B \left( 1/2, \frac{r-k+2n}{2} + \frac{1}{2} \right). \quad (\text{E.6})$$

Plugging (D.2) into (E.6) and computing the last summation on the R.H.S. yields

$$Q_{22} = j \sum_{r=1,3,(\text{odd})}^{\infty} \frac{1}{r!} \sum_{k=1,3,(\text{odd})}^r 2 \binom{(r-1)/2}{(k-1)/2} a^{r-k} b^k B\left(1/2, \frac{r+1}{2} + \frac{1}{2}\right). \quad (\text{E.7})$$

Noting that  $r = 2m + 1$ ,  $m = 1, 2, \dots$ , we combine (E.4) and (E.7):

$$Q_2 = Q_{21} + Q_{22} \quad (\text{E.8})$$

$$\begin{aligned} &= (a + jb) \sum_{m=0}^{\infty} \frac{1}{r!} \sum_{k=0,2,(\text{even})}^{2m} 2 \binom{m}{(k)/2} \\ &\quad (a^2)^{(m-\frac{k}{2})} (b^2)^{\frac{k}{2}} B\left(1/2, \frac{2m+2}{2} + \frac{1}{2}\right). \end{aligned} \quad (\text{E.9})$$

We use (D.2) and multiply and divide (E.9) by  $(a^2 + b^2)^{\frac{1}{2}}$

$$\begin{aligned} Q_2 &= \frac{a + jb}{\sqrt{(a^2 + b^2)}} 2\pi \sum_{m=0}^{\infty} \frac{1}{\Gamma(m+2)\Gamma(m+1)} \left(\frac{\sqrt{(a^2 + b^2)}}{2}\right)^{2m+1} \\ &= \frac{a + jb}{\sqrt{(a^2 + b^2)}} I_1(\sqrt{(a^2 + b^2)}). \end{aligned} \quad (\text{E.10})$$

To obtain the second line from the first, we used the series expansion of the modified Bessel function of the first kind with order 1 from (D.4)

# Appendix F

## Proof of Theorem 5.1

We rewrite  $\mathbf{y}$  from (5.4)

$$\begin{aligned}\mathbf{y} &= [\mathbf{y}_1^T, \dots, \mathbf{y}_M^T] + [\mathbf{e}_1^T, \mathbf{e}_2^T, \dots, \mathbf{e}_M^T] \\ &= [\beta_1 \boldsymbol{\gamma}_1^T, \beta_2 \boldsymbol{\gamma}_2^T, \dots, \beta_M \boldsymbol{\gamma}_M^T]^T + [\mathbf{e}_1^T, \mathbf{e}_2^T, \dots, \mathbf{e}_M^T],\end{aligned}\tag{F.1}$$

where

- $\boldsymbol{\gamma}_m = [\alpha_{1m} \sigma_{1m} e^{-j\psi_{1m}} e^{-j\tilde{\theta}_{1m}}, \dots, \alpha_{Nm} \sigma_{nm} e^{-j\psi_{Nm}} e^{-j\psi_{N_i}}]^T$ , for  $m = 1, \dots, M$  (see also (5.2) and (5.3)),
- $\mathbf{e}_m \sim \mathcal{CN}(\mathbf{0}, \sigma_e^2 \mathbf{I})$  for  $m = 1, \dots, M$  are i.i.d.

We define  $\tilde{\boldsymbol{\theta}} = [\tilde{\boldsymbol{\theta}}_1^T \dots \tilde{\boldsymbol{\theta}}_M^T]^T$ , where  $\tilde{\boldsymbol{\theta}}_m = [\tilde{\theta}_{1m}, \dots, \tilde{\theta}_{Nm}]^T$ . Recalling from Section 5.2.2 that the  $\tilde{\theta}_{nm}$  for  $n = 1, \dots, N$  and  $m = 1, \dots, M$  are i.i.d. and independent of the noise,  $\mathbf{e}_m$ , we obtain

$$\begin{aligned}I(\tilde{\boldsymbol{\theta}}; \mathbf{y}) &= \sum_{m=1}^M I(\tilde{\boldsymbol{\theta}}_m; \mathbf{y}_m) \\ &= \sum_{m=1}^M H(\mathbf{y}_m) - H(\mathbf{y}_m | \tilde{\boldsymbol{\theta}}_m),\end{aligned}\tag{F.2}$$

where  $H(\cdot)$  and  $H(\cdot|\cdot)$  are entropy and conditional entropy, respectively. Note that  $H(\mathbf{y}_m|\tilde{\boldsymbol{\theta}}) = H(\mathbf{e}_m)$ , and since  $\mathbf{e}_m \sim \mathcal{CN}(\mathbf{0}, \sigma_e^2 \mathbf{I})$ , then following an argument analogous to [69, Theorem 8.4.1]

$$H(\mathbf{e}) = \log \left( (\pi e)^N |\sigma_e^2 \mathbf{I}| \right), \quad (\text{F.3})$$

where “ $|\cdot|$ ” represents the determinant. Similarly, for  $H(\mathbf{y}_m)$  we follow an argument analogous to [69, Theorem 8.6.5], which shows that multivariate normal distribution maximizes the entropy over all distributions with the same covariance. Then

$$H(\mathbf{y}_m) \leq \log \left( (\pi e)^N |\text{Cov}(\mathbf{y}_m)| \right). \quad (\text{F.4})$$

We apply  $\int_{-\pi}^{\pi} \exp(-j\tilde{\theta}) \exp(\Delta \cos(\tilde{\theta})) d\tilde{\theta} = 2\pi I_1(\Delta)$  (recall that  $I_p(\cdot)$  is the modified Bessel function of the first kind with order  $p$ ), and compute

$$\text{Cov}(\mathbf{y}_m) = \beta_m^2 \text{diag} \left( \xi_{1m}^2 \left[ 1 - \left( \frac{I_1(\Delta)}{I_0(\Delta)} \right)^2 \right], \dots, \xi_{Nm}^2 \left[ 1 - \left( \frac{I_1(\Delta)}{I_0(\Delta)} \right)^2 \right] \right) + \sigma_e \mathbf{I}, \quad (\text{F.5})$$

with for  $\xi_{nm}^2 = \alpha_{nm}^2 \sigma_{nm}^2$ . Since  $\frac{I_1(\Delta)}{I_0(\Delta)} \leq 1$ , then

$$|\text{Cov}(\mathbf{y}_m)| \leq |\beta_m^2 \text{diag}(\xi_{1m}^2, \dots, \xi_{Nm}^2) + \sigma_e \mathbf{I}| = |\mathbf{W}_m + \sigma_e \mathbf{I}|. \quad (\text{F.6})$$

From (F.3), (F.4), and (F.6), we obtain

$$H(\mathbf{y}_m) - H(\mathbf{y}_m|\tilde{\boldsymbol{\theta}}) \leq \log \left( \frac{|\mathbf{W}_m + \sigma_e \mathbf{I}|}{|\sigma_e \mathbf{I}|} \right). \quad (\text{F.7})$$

Then the result in (5.22) follows from (F.2) and (F.7).

# Appendix G

## Solution to (5.25) for $M = 2$ and $N = 2, 4$

For  $M = 2$  and  $N = 2$ , (5.24) reduces to

$$q_m = \beta_m^2(\xi_{1m}^2 + \xi_{2m}^2) + \beta_m^2 \left( \frac{\xi_{1m}^2 \xi_{2m}^2}{\sigma_e^2} \right) \quad \text{for } m = 1, 2. \quad (\text{G.1})$$

We showed in (5.26) that the optimum solution to (5.25) is achieved when  $q_1 = q_2$ . Then using also the transmitted energy constraint  $\beta_2^2 = E - \beta_1^2$  (without loss of generality we take  $E = 1$ ), we obtain

$$c_1 \beta_1^4 + c_2 \beta_1^2 + c_3 = 0, \quad (\text{G.2})$$

where

- $c_1 = \left( \frac{\xi_{11}^2 \xi_{21}^2 - \xi_{12}^2 \xi_{22}^2}{\sigma_e^2} \right)$
- $c_2 = \left( \xi_{11}^2 + \xi_{21}^2 + \xi_{12}^2 + \xi_{22}^2 + \frac{2\xi_{12}^2 \xi_{22}^2}{\sigma_e^2} \right)$ , and
- $c_3 = - \left( \xi_{12}^2 + \xi_{22}^2 + \frac{\xi_{12}^2 \xi_{22}^2}{\sigma_e^2} \right)$ .

We easily find the roots of (G.2):

$$\beta_1^2 = \frac{-c_2 \pm \sqrt{c_2^2 - 4c_1c_3}}{2c_1}. \quad (\text{G.3})$$

Similarly for  $M = 2$  and  $N = 4$ , the problem reduces to a root finding of a polynomial equation of  $\beta_1^2$  of the fourth degree. The result can be obtained numerically using, for example, Newton's or a BFGS method [138].



# Appendix H

## Computation of the Conditional Mean and Covariance in (6.12)

In this appendix, we demonstrate how to obtain the conditional distribution,  $p(\boldsymbol{\xi}_n(k)|\mathbf{y}_n(k); \sigma_s^2, \sigma_e^2, \mathbf{X}_n)$ , and its mean  $\boldsymbol{\mu}_n$  and covariance,  $\tilde{\boldsymbol{\Sigma}}_n$  in (6.12). First, using (6.9) and (6.10), we write the joint distribution of  $\mathbf{y}_n$  and  $\boldsymbol{\xi}_n$ :

$$\begin{aligned} \begin{bmatrix} \mathbf{y}_n(k) \\ \boldsymbol{\xi}_n(k) \end{bmatrix} &= \mathbf{A} \begin{bmatrix} \boldsymbol{\xi}_n(k) \\ \mathbf{e}_n(k) \end{bmatrix} \\ &= \begin{bmatrix} \mathbf{X}_n \tilde{\boldsymbol{\Phi}}_n & \mathbf{I} \\ \mathbf{I} & \mathbf{0} \end{bmatrix} \begin{bmatrix} \boldsymbol{\xi}_n(k) \\ \mathbf{e}_n(k) \end{bmatrix}. \end{aligned} \quad (\text{H.1})$$

From Section 6.2.2, we know that  $\begin{bmatrix} \boldsymbol{\xi}_n(k) \\ \mathbf{e}_n(k) \end{bmatrix} \sim \mathcal{CN} \left( \mathbf{0}, \begin{bmatrix} \sigma_\xi^2 \mathbf{I} & \mathbf{0} \\ \mathbf{0} & \sigma_e^2 \mathbf{I} \end{bmatrix} \right)$ .

Then  $\begin{bmatrix} \mathbf{y}_n(k) \\ \boldsymbol{\xi}_n(k) \end{bmatrix} \sim \mathcal{CN} \left( \mathbf{0}, \begin{bmatrix} \boldsymbol{\Sigma}_n & \sigma_\xi^2 \mathbf{X}_n \tilde{\boldsymbol{\Phi}}_n \\ \sigma_\xi^2 \tilde{\boldsymbol{\Phi}}_n^H \mathbf{X}_n^H & \sigma_\xi^2 \mathbf{I} \end{bmatrix} \right)$  [see (6.6) for the definition of  $\boldsymbol{\Sigma}_n$ ].

Using the results from [118], we can show that  $\boldsymbol{\xi}_n | \mathbf{y}_n \sim \mathbb{CN}(\boldsymbol{\mu}_n, \tilde{\boldsymbol{\Sigma}}_n)$ , where

- $\boldsymbol{\mu}_n(k) = (\hat{\sigma}_\xi^2) \tilde{\boldsymbol{\Phi}}_n^H (\hat{\mathbf{X}}_n)^H (\boldsymbol{\Sigma}_n)^{-1} \mathbf{y}_n(k)$ , and
- $\tilde{\boldsymbol{\Sigma}}_n = (\hat{\sigma}_\xi^2)^{(i)} \mathbf{I} - (\hat{\sigma}_\xi^2) \tilde{\boldsymbol{\Phi}}_n^H (\hat{\mathbf{X}}_n)^H (\boldsymbol{\Sigma}_n)^{-1} \hat{\mathbf{X}}_n \tilde{\boldsymbol{\Phi}}_n$ .

# Appendix I

## Computation of the Elements of the Fisher Information Matrix in (6.14)

In this appendix, using (6.14) and (6.15), we compute the elements of the FIM.

We can easily show that

$$\begin{aligned} \bullet \mathbf{J}(\boldsymbol{\rho})_{(\text{Re}[\text{vech}(\mathbf{X}_n)]\text{Re}[\text{vech}(\mathbf{X}_{n'})])} &= \mathbf{J}(\boldsymbol{\rho})_{(\text{Re}[\text{vech}(\mathbf{X}_{n'})]\text{Re}[\text{vech}(\mathbf{X}_n)])} = \mathbf{J}(\boldsymbol{\rho})_{(\text{Re}[\text{vech}(\mathbf{X}_n)]\text{Im}[\text{vech}(\mathbf{X}_{n'})])} = \\ \mathbf{J}(\boldsymbol{\rho})_{(\text{Im}[\text{vech}(\mathbf{X}_{n'})]\text{Re}[\text{vech}(\mathbf{X}_n)])} &= \mathbf{J}(\boldsymbol{\rho})_{(\text{Im}[\text{vech}(\mathbf{X}_n)]\text{Re}[\text{vech}(\mathbf{X}_{n'})])} = \mathbf{J}(\boldsymbol{\rho})_{(\text{Im}[\text{vech}(\mathbf{X}_{n'})]\text{Re}[\text{vech}(\mathbf{X}_n)])} = \\ \mathbf{0}, & \text{ for } n, n' = 1, \dots, N \text{ and } n \neq n'. \end{aligned}$$

Here, for example,  $\mathbf{J}(\boldsymbol{\rho})_{(\text{Re}[\text{vech}(\mathbf{X}_n)]\text{Re}[\text{vech}(\mathbf{X}_{n'})])}$  is a partition of the Fisher information matrix corresponding to cross information between the elements of  $\text{Re}[\text{vech}(\mathbf{X}_n)]$  and  $\text{Re}[\text{vech}(\mathbf{X}_{n'})]$ , such that the index  $i$  in (6.14) is chosen from the index set of the elements of  $\text{Re}[\text{vech}(\mathbf{X}_n)]$ , and similarly  $j$  is chosen from the index set of the elements of  $\text{Re}[\text{vech}(\mathbf{X}_{n'})]$ .

Using the identity 3.4 from [139]

$$(\mathbf{I} - \mathbf{A})^{-1} = \mathbf{I} - \mathbf{A} + \mathbf{A}^2 - \mathbf{A}^3 + \dots, \quad (\text{I.1})$$

(6.15), and the definition of  $\Sigma_n$  in (6.6), we show that

$$\frac{\partial \Sigma_n}{\partial \sigma_\xi^2} \Sigma_n^{-1} = \frac{1}{\sigma_\xi^2} (\mathbf{I} - \sigma_e^2 \Sigma_n^{-1}). \quad (\text{I.2})$$

Then

$$[\mathbf{J}(\boldsymbol{\rho})]_{\sigma_\xi^2 \sigma_e^2} = \sum_{n=1}^N \left( \frac{1}{\sigma_\xi^2} \right)^2 [M - 2\sigma_e^2 \text{tr}(\Sigma_n^{-1}) + \sigma_e^4 [\mathbf{J}(\boldsymbol{\rho})]_{\sigma_e^2 \sigma_e^2}], \quad (\text{I.3})$$

$$[\mathbf{J}(\boldsymbol{\rho})]_{\sigma_e^2 \sigma_e^2} = \sum_{n=1}^N \text{tr}(\Sigma_n^{-1} \Sigma_n^{-1}), \quad (\text{I.4})$$

$$[\mathbf{J}(\boldsymbol{\rho})]_{\sigma_\xi^2 \sigma_e^2} = \sum_{n=1}^N \frac{1}{\sigma_\xi^2} [\text{tr}(\Sigma_n^{-1}) - \sigma_e^2 [\mathbf{J}(\boldsymbol{\rho})]_{\sigma_e^2 \sigma_e^2}]. \quad (\text{I.5})$$

We define  $\mathbf{X}_n = [\mathbf{X}_n^{(1)} \dots \mathbf{X}_n^{(M)}]$ , s.t.  $\mathbf{X}_n^{(m)}$  is the  $m^{\text{th}}$  column. Then

$$\frac{\partial \Sigma_n}{\partial \text{Re}\{x_{m_1 m_2}^n\}} = \sigma_\xi^2 ([\mathbf{0} \dots \mathbf{0} \mathbf{Q}_{m_2}^T \mathbf{0} \dots \mathbf{Q}_{m_1}^T \mathbf{0} \dots \mathbf{0}]^T \quad (\text{I.6})$$

$$[\mathbf{0} \dots \mathbf{0} \mathbf{Q}_{m_2}^H \mathbf{0} \dots \mathbf{Q}_{m_1}^H \mathbf{0} \dots \mathbf{0}]), \quad (\text{I.7})$$

where  $\mathbf{Q}_{m_1} = \beta_{m_2}^2 \alpha_{nm_2}^2 (\mathbf{X}_n^{(m_2)})^T$ , and  $\mathbf{Q}_{m_2} = \beta_{m_1}^2 \alpha_{nm_1}^2 (\mathbf{X}_n^{(m_1)})^T$  (recall the definitions of  $\beta$  and  $\alpha$  from (6.1)). We define  $\Sigma_n = [\boldsymbol{\sigma}_1 \dots \boldsymbol{\sigma}_M]$  with  $\boldsymbol{\sigma}_n$  as the  $n^{\text{th}}$  column,

and for  $m_1 \geq m_2$ , we obtain

$$\frac{\partial \Sigma_n}{\partial \text{Re}\{x_{m_1 m_2}^n\}} \Sigma_n^{-1} = \sigma_\xi^2 \mathbf{Q} \mathbf{Q} + \sigma_\xi^2 (\mathbf{Q}_{m_1}^H \boldsymbol{\sigma}_{m_1}^H + \mathbf{Q}_{m_2}^H \boldsymbol{\sigma}_{m_2}^H), \quad (\text{I.8})$$

where  $\mathbf{Q} \mathbf{Q} = \begin{bmatrix} 0 & \cdots & 0 \\ & \cdots & \\ \mathbf{Q}_{m_1} \boldsymbol{\sigma}_1 & \cdots & \mathbf{Q}_{m_1} \boldsymbol{\sigma}_M \\ 0 & \cdots & 0 \\ & \cdots & \\ \mathbf{Q}_{m_2} \boldsymbol{\sigma}_1 & \cdots & \mathbf{Q}_{m_2} \boldsymbol{\sigma}_M \\ 0 & \cdots & 0 \\ & \cdots & \end{bmatrix}$ . Note here that only the  $m_1^{\text{th}}$  and  $m_2^{\text{th}}$  rows

are non-zero. For  $m_1 = m_2 = m$ , only one row  $m^{\text{th}}$  row will be non-zero. Therefore we have only one  $\mathbf{Q}_m = \beta_m^2 \alpha_{nm}^2 (\mathbf{X}_n^{(m)})^T$ . We update (I.9) and (I.10) accordingly.

Then

$$[\mathbf{J}(\boldsymbol{\rho})]_{\text{Re}\{x_{m_1 m_2}^n\} \sigma_\xi^2} = \sum_{i=1}^M (\boldsymbol{\sigma}_{m_1})_i \mathbf{Q}_{m_1} \boldsymbol{\sigma}_i + (\boldsymbol{\sigma}_{m_2})_i \mathbf{Q}_{m_2} \boldsymbol{\sigma}_i + \boldsymbol{\sigma}_{m_1}^H (\mathbf{Q}_{m_1}^H)_i \boldsymbol{\sigma}_i + \boldsymbol{\sigma}_{m_2}^H (\mathbf{Q}_{m_2}^H)_i \boldsymbol{\sigma}_i, \quad (\text{I.9})$$

where for example  $(\boldsymbol{\sigma}_{m_1})_i$  and  $(\mathbf{Q}_{m_1}^H)_i$  are the  $i^{\text{th}}$  elements of the column vectors  $\boldsymbol{\sigma}_{m_2}$  and  $\mathbf{Q}_{m_1}^H$ , respectively.

We then compute

$$[\mathbf{J}(\boldsymbol{\rho})]_{\text{Re}\{x_{m_1 m_2}^n\} \sigma_\xi^2} = 2\text{Re}\{\mathbf{Q}_{m_1} \boldsymbol{\sigma}_{m_1} + \mathbf{Q}_{m_1} \boldsymbol{\sigma}_{m_1}\}. \quad (\text{I.10})$$

Finally, we obtain

$$\begin{aligned}
[\mathbf{J}(\boldsymbol{\rho})]_{\text{Re}\{x_{m_1 m_2}^n\}\text{Re}\{x_{m_3 m_4}^n\}} &= 2\sigma_\xi^4 \left[ \text{Re} \left\{ \mathbf{Q}_{m_1} \boldsymbol{\sigma}_{m_3} \mathbf{Q}_{m_3} \boldsymbol{\sigma}_{m_1} + \mathbf{Q}_{m_1} \boldsymbol{\sigma}_{m_4} \mathbf{Q}_{m_4} \boldsymbol{\sigma}_{m_1} + \right. \right. \\
&\quad \left. \left. \mathbf{Q}_{m_2} \boldsymbol{\sigma}_{m_3} \mathbf{Q}_{m_3} \boldsymbol{\sigma}_{m_2} + \mathbf{Q}_{m_2} \boldsymbol{\sigma}_{m_4} \mathbf{Q}_{m_4} \boldsymbol{\sigma}_{m_2} \right\} + QQ_{m_1 m_2 m_3} + \right. \\
&\quad \left. QQ_{m_1 m_2 m_4} + QQ_{m_3 m_4 m_1} + QQ_{m_3 m_4 m_2} \right], \tag{I.11}
\end{aligned}$$

where  $QQ_{mnp} = \text{tr}\{(\boldsymbol{\sigma}_p^H)_m \sum_{i=1}^M \mathbf{Q}_m \boldsymbol{\sigma}_i (\mathbf{Q}_p^H)_i + (\boldsymbol{\sigma}_p^H)_n \sum_{i=1}^M \mathbf{Q}_n \boldsymbol{\sigma}_i (\mathbf{Q}_p^H)_i\}$ .

For  $\text{Im}\{x_{m_1 m_2}^n\}$ , the Fisher information matrix elements are obtained similar to (I.9), (I.10), and (I.11) simply by replacing  $\mathbf{Q}_{m_1}$  and  $\mathbf{Q}_{m_2}$  with  $\mathbf{Q}_{m_1} = i\beta_{m_2}^2 \alpha_{nm_2}^2 \left(\mathbf{X}_n^{(m_2)}\right)^T$ , and  $\mathbf{Q}_{m_2} = -i\beta_{m_1}^2 \alpha_{nm_1}^2 \left(\mathbf{X}_n^{(m_1)}\right)^T$ .

# References

- [1] R. N. Miles, D. Robert, and R. R. Hoy, “Mechanically coupled ears for directional hearing in the parasitoid fly *Ormia ochracea*,” *J. Acoust. Soc. Am.*, vol. 98, no. 6, pp. 3059–3070, 1995.
- [2] A. Popper and R. Fay, Eds., *Sound Source Localization*, ser. Handbook of auditory research. New York, NY: Springer, 2005, vol. 22.
- [3] P. Morse and K. Ingard, *Theoretical Acoustics*. New York, NY: McGraw-Hill, 1968.
- [4] C. Brown, M. Beecher, D. Moody, and W. Stebbins, “Localization of primate calls by Old World monkeys,” *Science*, vol. 201, pp. 753–754, 1978.
- [5] D. Houben and G. Gourevitch, “Auditory localization in monkeys: an examination of two cues serving directional hearing,” *J. Acoust. Soc. Am.*, vol. 66, pp. 1057–1063, 1979.
- [6] B. Masterton, H. Heffner, and R. Ravizza, “The evolution of human hearing,” *J. Acoust. Soc. Am.*, vol. 45, pp. 966–985, 1969.
- [7] J. Blauert, *Spatial Hearing, The Psychophysics of Human Sound Localization*. Cambridge, MA: MIT Press., 1997.
- [8] A. Huang and B. May, “Spectral cues for sound localization in cats: effects of frequency domain on minimum audible angles in the median and horizontal planes,” *J. Acoust. Soc. Am.*, vol. 100, pp. 2341–2348, 1996.
- [9] H. Heffner and R. Heffner, “Sound localization in large mammals: localization of complex sounds by horses,” *Behav. Neurosci*, vol. 98, pp. 541–555, 1984.
- [10] R. Heffner and H. Heffner, “Sound localization, use of binaural cues, and the superior olivary complex in pigs,” *Brain Behav. Evol.*, vol. 33, pp. 248–258, 1989.
- [11] A. Michelsen, “Hearing and sound communication in small animals: evolutionary adaptations to the laws of physics,” in *The Evolutionary Biology of Hearing*, D. Webster, R. Fay, and A. Popper, Eds. New York, NY: Springer-Verlag, 1992.

- [12] N. H. Fletcher and S. Thwaites, “Acoustical analysis of the auditory system of the cricket *Teleogryllus commodus* (walker),” *J. Acoust. Soc. Am.*, vol. 66, no. 2, pp. 350–357, Aug. 1979.
- [13] A. Michelsen, A. V. Popov, and B. Lewis, “Physics of directional hearing in the cricket *Gryllus bimaculatus*,” *J. Comp. Soc. Physiol. A*, vol. 175, no. 2, pp. 153–164, Aug. 1994.
- [14] A. R. Palmer and A. Pinder, “The directionality of the frog ear described by a mechanical model,” *J. Theor. Biol.*, vol. 110, no. 2, pp. 205–215, 1984.
- [15] J. Eggermont, “Mechanism of sound localization in anurans,” in *The Evolution of the amphibian auditory system*, B. Fritzsche, M. Ryan, W. Wilczynski, T. Hetherington, and W. Walkowiak, Eds. New York, NY: John Wiley, 1988.
- [16] P. Narins, G. Ehret, and J. Tautz, “Accessory pathway for sound transfer in a neotropical frog,” in *Proc. Natl. Acad. Sci.*, USA, 1988, pp. 1508–1512.
- [17] E. Knudsen, “Sound localization in birds,” in *Comparative studies of hearing in vertebrates*, A. Popper and R. Fay, Eds. New York, NY: Springer, 1980.
- [18] W. Cade, “Acoustically Orienting Parasitoids: Fly Phonotaxis to Cricket Song,” *Science*, vol. 190, pp. 1312–1313, Dec. 1975.
- [19] T. Walker, “Monitoring the flight of field crickets (*Gryllus* spp.) and a tachinid fly (euphasiopterix ochracea) in north florida,” *Fl. Entomol.*, vol. 69, pp. 678–685, 1986.
- [20] W. Cade, M. Ciceran, and A. Murray, “Temporal patterns of parasitoid fly (*Ormia ochracea*) attraction to field cricket song (*Gryllus integer*),” *Can. J. Zool.*, vol. 74, pp. 393–395, 1996.
- [21] D. Robert, M. J. Amoroso, and R. R. Hoy, “The evolutionary convergence of hearing in a parasitoid fly and its cricket host,” *Science*, vol. 258, no. 5085, pp. 1135–1137, 1992.
- [22] D. Robert, M. P. Read, and R. R. Hoy, “The tympanal hearing organ of the parasitoid fly *Ormia ochracea* (diptera, tachinidae, ormiini),” *Cell Tissue Res.*, vol. 275, no. 1, pp. 63–78, 1994.
- [23] A. C. Mason, M. L. Oshinsky, and R. R. Hoy, “Hyperacute directional hearing in a microscale auditory system,” *Nature*, vol. 410, pp. 686–690, Apr. 2001.
- [24] D. Robert, R. N. Miles, and R. R. Hoy, “Directional hearing by mechanical coupling in the parasitoid fly *Ormia ochracea*,” *J. Comp. Physiol. A*, vol. 179, no. 1, pp. 29–44, Jul. 1996.



- [25] —, “Tympanal mechanics in the parasitoid fly *Ormia ochracea*: intertympanal coupling during mechanical vibration,” *J. Comp. Physiol. A*, vol. 183, no. 4, pp. 443–452, Oct. 1998.
- [26] M. Akcakaya and A. Nehorai, “Performance analysis of *Ormia ochracea*’s coupled ears,” *J. Acoust. Soc. Am.*, vol. 124, no. 4, pp. 2100–2105, Oct. 2008.
- [27] M. Akcakaya, C. Muravchik, and A. Nehorai, “Biologically inspired coupled antenna array for direction of arrival estimation,” in *Proc. 44th Asilomar Conf. Signals, Syst. Comput.*, Pacific Grove, CA, USA, Nov. 7-10 2010.
- [28] —, “Biologically inspired coupled antenna array for direction of arrival estimation,” *IEEE Trans. Signal Process.*, in revision.
- [29] M. Akcakaya and A. Nehorai, “Biologically inspired coupled antenna beam pattern design,” *Bioinspiration and Biomimetics*, vol. 5, no. 4, p. 046003, 2010.
- [30] —, “Biologically inspired coupled beam pattern design,” in *Proc. IEEE 5th Int. Waveform Diversity and Design Conf.*, Niagara Falls, ON, Canada, Aug. 8-13 2010, pp. 48–52.
- [31] J. Li and P. Stoica, *MIMO Radar Signal Processing*. Wiley-IEEE Press, Oct. 2008.
- [32] M. I. Skolnik, *Introduction to Radar Systems*, 3rd ed. McGraw-Hill, 2002.
- [33] J. Li and P. Stoica, “MIMO radar with colocated antennas,” *IEEE Signal Process. Mag.*, vol. 24, pp. 106–114, Sept. 2007.
- [34] A. Haimovich, R. Blum, and L. Cimini, “MIMO radar with widely separated antennas,” *IEEE Signal Process. Mag.*, vol. 25, pp. 116–129, Jan. 2008.
- [35] J. Li, P. Stoica, L. Xu, and W. Roberts, “On parameter identifiability of mimo radar,” *IEEE Signal Process Lett.*, vol. 14, no. 12, pp. 968–971, dec. 2007.
- [36] I. Bekkerman and J. Tabrikian, “Target detection and localization using MIMO radars and sonars,” *IEEE Trans. Signal Process.*, vol. 54, pp. 3873–3883, Oct 2006.
- [37] K. Forsythe, D. Bliss, and G. Fawcett, “Multiple-input multiple-output (MIMO) radar: Performance issues,” in *Proc. 38th Asilomar Conf. Signals, Systems and Computers*, Pacific Grove, CA, Nov. 2004, pp. 310–315.
- [38] C. Y. Chen and P. P. Vaidyanathan, “MIMO radar spacetime adaptive processing using prolate spheroidal wave functions,” *IEEE Trans. Signal Process.*, vol. 56, pp. 623–635, Feb 2008.

- [39] D. Fuhrmann and G. S. Antonio, "Transmit beamforming for MIMO radar systems using partial signal correlation," in *In Proc. of the Thirty-Eighth Asilomar Conf. on Signals, Systems and Computers*, vol. 1, Nov. 2004, pp. 295–299 Vol.1.
- [40] P. Stoica, J. Li, and Y. Xie, "On probing signal design for MIMO radar," *IEEE Trans. on Signal Process.*, vol. 55, no. 8, pp. 4151–4161, Aug. 2007.
- [41] D. Fuhrmann and G. S. Antonio, "Transmit beamforming for MIMO radar systems using signal cross-correlation," *IEEE Trans. Aerospace and Electronic Systems*, vol. 44, no. 1, pp. 171–186, Jan. 2008.
- [42] J. Li, L. Xu, P. Stoica, K. Forsythe, and D. Bliss, "Range compression and waveform optimization for MIMO radar: A Cramer-Rao bound based study," *IEEE Trans. Signal Process.*, vol. 56, no. 1, pp. 218–232, Jan. 2008.
- [43] N. Levanon, *Radar Principles*, 1st ed. Wiley-Interscience, 1988.
- [44] H. L. V. Trees, *Detection, Estimation, and Modulation Theory, Part III*. New York, NY: Wiley, 1968.
- [45] E. Fishler, A. Haimovich, R. Blum, L. Cimini, D. Chizhik, and R. Valenzuela, "Spatial diversity in radars - models and detection performance," *IEEE Trans. Signal Process.*, vol. 54, no. 3, pp. 823–838, Mar. 2006.
- [46] N. Lehmann, A. Haimovich, R. Blum, and L. Cimini, "High resolution capabilities of MIMO radar," in *Proc. 40th Asilomar Conf. Signals, Systems and Computers*, Pacific Groove, CA, Nov. 2006, pp. 25–30.
- [47] N. Lehmann, E. Fishler, A. Haimovich, R. Blum, D. Chizhik, L. Cimini, and R. Valenzuela, "Evaluation of transmit diversity in MIMO-radar direction finding," *IEEE Trans. Signal Process.*, vol. 55, no. 5, pp. 2215–2225, May 2007.
- [48] H. Godrich, A. Haimovich, and R. Blum, "Target localization techniques and tools for multiple-input multiple-output radar," *IET Radar, Sonar Navigation*, vol. 3, no. 4, pp. 314–327, Aug. 2009.
- [49] —, "Target localization accuracy gain in MIMO radar-based systems," *IEEE Trans. Information Theory*, vol. 56, no. 6, pp. 2783–2803, Jun. 2010.
- [50] Q. He, R. Blum, H. Godrich, and A. Haimovich, "Target velocity estimation and antenna placement for MIMO radar with widely separated antennas," *IEEE Journal of Selected Topics in Signal Processing*, vol. 4, no. 1, pp. 79–100, Feb. 2010.
- [51] Q. He, N. Lehmann, R. Blum, and A. Haimovich, "MIMO radar moving target detection in homogeneous clutter," *IEEE Trans. Aerospace and Electronic Systems*, vol. 46, no. 3, pp. 1290–1301, Jul. 2010.

- [52] A. Sheikhi and A. Zamani, “Temporal coherent adaptive target detection for multi-input multi-output radars in clutter,” *Radar Sonar and Navigation IET*, pp. 86–96, Apr. 2008.
- [53] P. Sammartino, C. Baker, and H. Griffiths, “Adaptive MIMO radar system in clutter,” *Radar Conference 2007 IEEE*, pp. 276–281, Apr. 2007.
- [54] H. Godrich, V. Chiriac, A. Haimovich, and R. Blum, “Target tracking in MIMO radar systems: Techniques and performance analysis,” in *IEEE Radar Conference*, May. 2010, pp. 1111–1116.
- [55] N. Lehmann, A. Haimovich, R. Blum, and L. Cimini, “MIMO-radar application to moving target detection in homogenous clutter,” in *Proc. Adaptive Array Processing Workshop (ASAP)*, MIT Lincoln Laboratory, MA, Jul. 2006.
- [56] H. Godrich, A. Haimovich, and H. Poor, “An analysis of phase synchronization mismatch sensitivity for coherent MIMO radar systems,” in *Computational Advances in Multi-Sensor Adaptive Processing (CAMSAP), 2009 3rd IEEE International Workshop on*, Dec. 2009, pp. 153–156.
- [57] Q. He and R. Blum, “Cramer-Rao bound for MIMO radar target localization with phase errors,” *Signal Processing Letters, IEEE*, vol. 17, no. 1, pp. 83–86, Jan. 2010.
- [58] Y. Abramovich and G. Frazer, “Bounds on the volume and height distributions for the MIMO radar ambiguity function,” *IEEE Signal Processing Letters*, vol. 15, pp. 505–508, 2008.
- [59] M. Akcakaya, M. Hurtado, and A. Nehorai, “MIMO radar detection of targets in compound-Gaussian clutter,” in *Proc. 42nd Asilomar Conf. Signals, Syst. Comput.*, Pacific Grove, CA, USA, Oct. 2008 (invited).
- [60] M. Akcakaya and A. Nehorai, “MIMO radar detection and adaptive design in compound-Gaussian clutter,” in *IEEE Radar Conference*, May. 2010, pp. 236–241.
- [61] —, “Adaptive MIMO radar design and detection in compound-Gaussian clutter,” *IEEE Trans. Aerospace and Electronic Systems*, accepted for publication.
- [62] A. Balleri, A. Nehorai, and J. Wang, “Maximum likelihood estimation for compound-Gaussian clutter with inverse gamma texture,” *IEEE Trans. Aerosp. and Electron. Syst.*, vol. 43, no. 2, pp. 775–779, 2007.
- [63] C. Liu, D. Rubin, and Y. Wu, “Parameter expansion to accelerate EM: The PX-EM algorithm,” *Biometrika*, vol. 85, pp. 755–770, Dec. 1998.

- [64] M. Akcakaya and A. Nehorai, “MIMO radar detection under phase synchronization errors,” in *IEEE 35th Int. Conf. Acoust., Speech, Signal Process (ICASSP)*., Dallas, TX, USA, Mar. 2010, pp. 2578 –2581.
- [65] —, “MIMO radar detection and adaptive design under a phase synchronization mismatch,” *IEEE Trans. Signal Process.*, vol. 58, no. 10, pp. 4994 –5005, Oct. 2010.
- [66] K. V. Mardia and P. E. Jupp, *Directional Statistics*, 2nd ed. Wiley, 1999.
- [67] A. P. Dempster, N. M. Laird, and D. B. Rubin, “Maximum likelihood from incomplete data via the EM algorithm,” *Journal of the Royal Statistical Society, Series B (Methodological)*, vol. 39, no. 1, pp. 1–38, 1977.
- [68] S. M. Kay, *Fundamentals of Statistical Signal Processing: Detection Theory*. Upper Saddle River, NJ: Prentice Hall PTR, 1998.
- [69] T. M. Cover and J. A. Thomas, *Elements of Information Theory*, 2nd ed. Wiley-Interscience, Jul. 2006.
- [70] M. Akcakaya and A. Nehorai, “MIMO radar sensitivity analysis for target detection,” *IEEE Trans. Signal Process.*, in revision.
- [71] K. Ogata, *Modern Control Engineering*, 4th ed. Upper Saddle River, NJ: Prentice Hall PTR.
- [72] W. E. Boyce and R. C. DiPrima, *Elementary Differential Equations and Boundary Value Problems*, 7th ed. Wiley, 2000.
- [73] A. V. Oppenheim, R. W. Schaffer, and J. R. Buck, *Discrete-Time Signal Processing*, 2nd ed. Upper Saddle River, NJ: Prentice Hall PTR.
- [74] P. Whittle, “The analysis of multiple stationary time series,” *Journal of the Royal Statistical Society, Series B (Methodological)*, vol. 15, no. 1, pp. 125–139, 1953.
- [75] S. M. Kay, *Fundamentals of Statistical Signal Processing: Estimation Theory*. Upper Saddle River, NJ: Prentice Hall PTR, 1993.
- [76] Y. Bar-Shalom, *Tracking and data association*. San Diego, CA, USA: Academic Press Professional, Inc., 1987.
- [77] I. Pavildis, V. Morellas, P. TsiamyrTzis, and S. Harp, “Urban surveillance systems: From the laboratory to the commercial world,” *Proc. IEEE*, vol. 89, pp. 1478–1497, Oct. 2001.

- [78] N. J. Reddingt, D. M. Bootht, and R. Jonest, “Urban video surveillance from airborne and ground-based platforms,” in *IEE Int. Symp. Imaging for Crime Detection and Prevention (ICDP)*, Australia, 7-8.
- [79] M. W. Long, *Radar Reflectivity of Land and Sea*. Dedham, MA: Artech House, 2001.
- [80] A. R. Brenner and L. Roessing, “Radar imaging of urban areas by means of very high-resolution SAR and interferometric SAR,” *IEEE Trans. Geoscience and Remote Sensing*, vol. 46, pp. 2971–2982, Oct. 2008.
- [81] A. Nehorai and E. Paldi, “Vector-sensor array processing for electromagnetic source localization,” *IEEE Trans. Signal Process.*, vol. 42, no. 2, pp. 376–398, Feb 1994.
- [82] P. Stoica and K. Sharman, “Maximum likelihood methods for direction-of-arrival estimation,” *IEEE Trans. on Acoust., Speech and Signal Process.*, vol. 38, no. 7, pp. 1132–1143, jul 1990.
- [83] A. Swindlehurst and P. Stoica, “Maximum likelihood methods in radar array signal processing,” *Proc. IEEE*, vol. 86, no. 2, pp. 421–441, feb 1998.
- [84] C. Balanis, *Antenna Theory: Analysis and Design*. New York: John Wiley and sons, Inc., 1982.
- [85] C. Knapp and G. Carter, “The generalized correlation method for estimation of time delay,” *IEEE Trans. Acoust., Speech, Signal Process.*, vol. 24, no. 4, pp. 320–327, aug 1976.
- [86] P. Roth, “Effective measurements using digital signal analysis,” *IEEE Spectrum*, vol. 8, no. 4, pp. 62–70, april 1971.
- [87] G. Carter, A. Nuttall, and P. Cable, “The smoothed coherence transform,” *Proc. IEEE (Lett.)*, vol. 61, no. 10, pp. 1497–1498, oct. 1973.
- [88] —, “The smoothed coherence transform (scot),” Naval Underwater Systems Center, New London Lab., New London, CT, Tech. Rep. TC-159-72, Aug. 8 1972.
- [89] C. Eckart, “Optimal rectifier systems for the detection steady signals,” Scripps Inst. Oceanography, Marine Physical Lab., Univ. California., Tech. Rep. SIO 12692 SIO Ref. 52-11, 1952.
- [90] E. J. Hannan and P. J. Thomson, “Estimating group delay,” *Biometrika*, vol. 60, no. 2, pp. 241–253, Aug. 1973.

- [91] A. Quazi, “An overview on the time delay estimate in active and passive systems for target localization,” *IEEE Trans. Acoust., Speech, Signal Process.*, vol. 29, no. 3, pp. 527 – 533, jun 1981.
- [92] K. Scarbrough, N. Ahmed, and G. Carter, “On the simulation of a class of time delay estimation algorithms,” *IEEE Trans. Acoust., Speech, Signal Process.*, vol. 29, no. 3, pp. 534 – 540, jun 1981.
- [93] J. Chen, J. Benesty, and Y. Huang, “Robust time delay estimation exploiting redundancy among multiple microphones,” *IEEE Trans. Speech and Audio Process.*, vol. 11, no. 6, pp. 549 – 557, 2003.
- [94] A. Dogandzic and A. Nehorai, “Cramer-rao bounds for estimating range, velocity, and direction with an active array,” *IEEE Trans. Signal Process.*, vol. 49, no. 6, pp. 1122 –1137, Jun. 2001.
- [95] B. Ottersten, M. Viberg, P. Stoica, and A. Nehorai, “Exact and large sample approximations of maximum likelihood techniques for parameter estimation and detection in array processing,” in *Radar Array Processing*, S. Haykin, J. Litva, and T. Shepherd, Eds. Springer-Verlag, 1993, pp. 99–151.
- [96] H. Krim and M. Viberg, “Two decades of array signal processing research: the parametric approach,” *IEEE Signal Process. Magazine*, vol. 13, no. 4, pp. 67 –94, jul. 1996.
- [97] P. Stoica and A. Nehorai, “On the concentrated stochastic likelihood function in array signal processing,” *Circ., Syst., and Sig. Proc.*, vol. 14, no. 5, pp. 669–674, Sept. 1995.
- [98] ———, “Performance study of conditional and unconditional direction-of-arrival estimation,” *IEEE Trans. Acoust., Speech, and Signal Process.*, vol. 38, no. 10, pp. 1783–1795, Oct. 1990.
- [99] A. Nehorai and E. Paldi, “Vector-sensor array processing for electromagnetic source localization,” *IEEE Trans. Signal Process.*, pp. 376–398, Feb 1994.
- [100] B. Hochwald and A. Nehorai, “Identifiability in array processing models with vector-sensor applications,” *IEEE Trans. Signal Process.*, vol. 44, no. 1, pp. 83 –95, jan 1996.
- [101] D. Tucker, “Superdirective arrays: the use of decoupling between elements to ease design and increase bandwidth,” *Radio and Electronic Engineer*, vol. 34, no. 4, pp. 251 –256, october 1967.
- [102] E. Newman, J. Richmond, and C. Walter, “Superdirective receiving arrays,” *IEEE Trans. Antennas Propag.*, vol. 26, no. 5, pp. 629 – 635, sep 1978.

- [103] B. Popovic, B. Notaros, and Z. Popovic, "Supergain antennas: a novel philosophy of synthesis and design,," in *Proc. 26th URSI General Assembly*, Toronto, Ontario, Canada, August 1999, p. 7675.
- [104] T. Lee and Y. E. Wang, "Mode-Based Information Channels in Closely Coupled Dipole Pairs," *IEEE Trans. Antennas Propag.*, vol. 56, pp. 3804–3811, Dec. 2008.
- [105] J. Allen and B. Diamond, "Mutual coupling in array antennas," MIT Lincoln Laboratory, Lexington, MA, Tech. Rep. 424, Oct. 1966.
- [106] I. Gupta and A. Ksienski, "Effect of mutual coupling on the performance of adaptive arrays," *IEEE Trans. Antennas Propag.*, vol. 31, no. 5, pp. 785–791, Sep 1983.
- [107] T. Svantesson, "The effects of mutual coupling using a linear array of thin dipoles of finite length," in *Proc. Ninth IEEE SP Workshop on Statistical Signal and Array Proces.*, Sep 1998, pp. 232–235.
- [108] K. Ward, C. Baker, and S. Watts, "Maritime surveillance radar. I. Radar scattering from the ocean surface," in *IEE Proc. F*, vol. 137, Apr. 1990, pp. 51–62.
- [109] F. Gini, A. Farina, and G. Foglia, "Effects of foliage on the formation of K-distributed SAR imagery," *Signal Processing*, vol. 75, pp. 161–171, Jun. 1999.
- [110] M. Greco, F. Bordonni, and F. Gini, "X-band sea-clutter nonstationarity: Influence of long waves," *IEEE J. Ocean. Eng.*, vol. 29, no. 2, pp. 269–283, Apr. 2004.
- [111] J. Wang, A. Dogandzic, and A. Nehorai, "Maximum likelihood estimation of compound-Gaussian clutter and target parameters," *IEEE Trans. Signal Process.*, vol. 54, no. 10, pp. 3884–3898, Oct. 2006.
- [112] E. Lehmann and J. P. Romano, *Testing Statistical Hypotheses*, 3rd ed. Springer, Sep. 2008.
- [113] A. Dogandzic and A. Nehorai, "Generalized multivariate analysis of variance: A unified framework for signal processing in correlated noise," *IEEE Signal Process. Mag.*, vol. 20, pp. 39–54, Sep. 2003.
- [114] J. Ward, "Space-time adaptive processing for airborne radar," Lincoln Laboratory, MIT, Lexington, MA, Tech. Rep. 1015, Apr. 1994.
- [115] F. Gini and M. Greco, "Texture modelling, estimation and validation using measured sea clutter data," *IEE Proc. Radar, Sonar and Navigation*, vol. 149, no. 3, pp. 115–124, Jun 2002.

- [116] P. Bickel and K. Doksum, *Mathematical Statistics: Basic Ideas and Selected Topics*, 2nd ed. Upper Saddle River, NJ: Prentice Hall, 2000.
- [117] K. Lange, R. Little, and J. Taylor, “Robust statistical modeling using the t distribution,” *Journal of the American Statistical Association*, vol. 84, no. 408, pp. 881–896, 1989.
- [118] T. W. Anderson, *An Introduction to Multivariate Statistical Analysis*, 2nd ed. Wiley, Sep. 2003.
- [119] E. F. Vonesh and V. Chincihilli, *Linear and Nonlinear Models for the Analysis of Repeated Measurements*, 1st ed. Dekker, 1996.
- [120] Y. Fujikoshi, “Asymptotic expansions of the non-null distributions of three statistics in GMANOVA,” *Annals of the Institute of Statistical Mathematics*, vol. 26, no. 1, pp. 289–297, Dec. 1974.
- [121] Q. He, R. Blum, H. Godrich, and A. Haimovich, “Cramer-Rao bound for target velocity estimation in MIMO radar with widely separated antennas,” *Information Sciences and Systems CISS 2008 42nd Annual Conference*, pp. 123–127, Mar. 2008.
- [122] I. Papoutsis, C. Baker, and H. Griffiths, “Fundamental performance limitations of radar networks,” in *Proc. 1st EMRS DTC Technical Conf.*, Edinburgh, 2004.
- [123] A. Fletcher and F. Robey, “Performance bounds for adaptive coherence of sparse array radar,” presented at the 11th Conf. Adaptive Sensors Array Processing, Lexington, MA, Mar 2003.
- [124] V. I. Tikhonov, “The effects of noise on phase-lock oscillator operation,” *Automat. i Telemekh.*, vol. 22, no. 9, 1959.
- [125] A. J. Viterbi, “Phase-locked loop dynamics in the presence of noise by Fokker-Planck techniques,” *Proc. of the IEEE*, vol. 51, no. 12, p. 17371753, 1963.
- [126] —, “Optimum detection and signal selection for partially coherent binary communication,” *IEEE Trans. Inf. Theory*, vol. 11, no. 2, pp. 239–246, 1965.
- [127] M. Bell, “Information theory and radar waveform design,” *IEEE Trans. Inf. Theory*, vol. 39, no. 5, pp. 1578–1597, Sep 1993.
- [128] Y. Yang and R. Blum, “MIMO radar waveform design based on mutual information and minimum mean-square error estimation,” *IEEE Trans. Aerosp. and Electron. Syst.*, vol. 43, no. 1, pp. 330–343, January 2007.
- [129] A. Dogandzic and J. Jin, “Estimating statistical properties of composite gamma-lognormal fading channels,” in *IEEE GLOBECOM Conf.*, vol. 5, San Francisco, CA, Dec. 2003, pp. 2406–2410.



- [130] S. Boyd and L. Vandenberghe, *Convex Optimization*. Cambridge University Press, Mar. 2004.
- [131] G. S. Antonio, D. Fuhrmann, and F. Robey, “MIMO radar ambiguity functions,” *IEEE Journal of Selected Topics in Signal Processing*, vol. 1, no. 1, pp. 167–177, Jun. 2007.
- [132] F. Daum and J. Huang, “MIMO radar: Snake oil or good idea?” *IEEE Aerospace and Electronic Systems Magazine*, vol. 24, no. 5, pp. 8–12, May. 2009.
- [133] E. J. Kelly and K. M. Forsythe, “Adaptive detection and parameter estimation for multidimensional signal models,” Lincoln Laboratory, MIT, Lexington, MA, Tech. Rep. 848, Apr. 1989.
- [134] F. Gini and M. Greco, “Suboptimum approach to adaptive coherent radar detection in compound-Gaussian clutter,” *IEEE Trans. Aerosp. and Electron. Syst.*, vol. 35, no. 3, pp. 1095–1104, Jul 1999.
- [135] E. Conte, M. Lops, and G. Ricci, “Asymptotically optimum radar detection in compound-Gaussian clutter,” *IEEE Trans. Aerosp. and Electron. Syst.*, vol. 31, no. 2, pp. 617–625, Apr 1995.
- [136] S. M. Kay, *Fundamentals of Statistical Signal Processing, Volume 1: Estimation Theory*. Upper Saddle River, NJ: Prentice Hall PTR, 1993.
- [137] M. Abramowitz and I. A. Stegun, *Handbook of Mathematical Functions: With Formulas, Graphs, and Mathematical Tables*. Dover Publications, Jun. 1965.
- [138] J. E. Dennis and R. B. Schnabel, *Numerical Methods for Unconstrained Optimization and Nonlinear Equations*. Society for Industrial Mathematics, 1987.
- [139] K. B. Petersen and M. S. Pedersen, *The Matrix Cookbook*. Technical University of Denmark, Oct 2008.

# Vita

Murat Akçakaya

- Date of Birth** April 8, 1982
- Place of Birth** Kutahya, Turkey
- Degrees** B.Sc., Electrical and Electronics Engg., Middle East Technical University, Ankara, Turkey June 2005
- M.Sc., Electrical Engineering, Washington University in St.Louis, May 2010
- Ph.D., Electrical & Systems Engineering, Washington University in St.Louis, December 2010
- Affiliations** Student member of IEEE Signal Processing Society
- Awards** First place award in the student paper competition at the *5th Int. Waveform Diversity & Design (WDD) Conf.*, Niagara Falls, Canada, Aug. 8–13, 2010.
- Third place award in the student paper competition at the *44th Asilomar Conf. Signals, Syst., and Comput.*, Pacific Grove, CA, Nov. 7-10, 2010.
- Third place award in the student paper competition at the *IEEE Int. Radar Conference* Washington DC, USA, May 10-14, 2010.
- Publications** M. Akcakaya, C.H. Muravchik, and A. Nehorai, “Biologically inspired coupled antenna array for direction of arrival estimation” *IEEE Trans. Signal Process.*, in revision.

M. Akcakaya and A. Nehorai, "MIMO radar sensitivity analysis for target detection," *IEEE Trans. Signal Process.*, in revision.

M. Akcakaya and A. Nehorai, "Adaptive MIMO radar design and detection in compound-Gaussian clutter," *IEEE Trans. on Aerospace and Electronic Systems*, accepted for publication.

M. Akcakaya and A. Nehorai, "Biologically inspired coupled antenna beampattern design," *Bioinspiration & Biomimetics*, vol.5, no.4, p. 046003, 2010.

M. Akcakaya and A. Nehorai, "MIMO radar detection and adaptive design under a phase synchronization mismatch," *IEEE Trans. on Signal Process.*, vol.58, no.10, pp. 4994-5005, Oct. 2010.

M. Akcakaya and A. Nehorai, "Performance analysis of the Ormia ochracea's coupled ears," *The Journal of the Acoustical Society of America*, Vol. 124, pp. 2100-2105, Oct. 2008.

M. Akcakaya and A. Nehorai, "MIMO radar sensitivity analysis for target detection," *2011 IEEE Radar Conference.*, submitted.

M. Akcakaya, C.H. Muravchik and A. Nehorai, "Biologically Inspired Direction of Arrival Estimation," *GOMACTech 2011*, Orlando, FL, USA, Mar. 21-24, 2011.

M. Akcakaya, C.H. Muravchik and A. Nehorai, "Biologically Inspired Coupled Antenna Array for Direction of Arrival Estimation," *Proc. 44th Asilomar Conf. Signals, Syst. Comput.*, Pacific Grove, CA, USA, Nov. 7-10, 2010.

M. Akcakaya and A. Nehorai, "Biologically inspired coupled beampattern design," *Proc. IEEE 5th Int. Waveform Diversity and Design Conf.*, Niagara Falls, Canada, Aug. 8-13, 2010.

M. Akcakaya and A. Nehorai, "MIMO radar detection and adaptive design in Compound-Gaussian clutter," *Proc. IEEE*

*Int. Radar Conf.*, Washington DC, USA, May 10-14, 2010, pp 236-241.

M. Akcakaya, and A. Nehorai, “MIMO radar detection under phase synchronization errors,” *Proc. IEEE Int. Conf. Acoust., Speech, Signal Processing (ICASSP)*, Dallas, TX, USA, Mar. 14-19, 2010, pp. 2578-2581.

M. Akcakaya, M. Hurtado and A. Nehorai, “MIMO radar detection of targets in compound-Gaussian clutter,” *Proc. 42nd Asilomar Conf. Signals, Syst. Comput.*, Pacific Grove, CA, USA, Oct. 2008, pp. 208-212.

December 2010

**Bioinspiration and MIMO Radar, Akçakaya, Ph.D. 2010**